Image Degradation Effects in Time-Delay Integration CCDs

Von der Fakultät für Ingenieurwissenschaften,
Abteilung Elektrotechnik und Informationstechnik
der Universität Duisburg-Essen

zur Erlangung des akademischen Grades

Doktor der Ingenieurwissenschaften

genehmigte Dissertation

von

Denis Szymon Piechaczek
aus
Tarnowitz, Polen

Gutachter: Prof. Dr.-Ing. Rainer Kokozinski
Gutachter: Prof. Dr. rer. nat. Andreas Wieck

Tag der mündlichen Prüfung: 27.04.2023

Für Chelsea und meine Eltern.

Abstract

In recent years, the interest in sophisticated optical image sensors for earth observation increased as a result of an increasing number of applications and addressable markets. However, due to the relative motion between the satellite and the earth, these sensors suffer, in general, from a short integration time per pixel, causing a limitation of the signal-to-noise ratio (SNR). To overcome these disadvantages, sensors with a special architecture have been designed which enable the accumulation of photogenerated electrons from multiple exposures without additional noise. Sensors accomplishing these requirements are time-delay integration (TDI) charge-coupled devices (CCDs), which have gained increased interest due to their capability of detecting fast-moving objects at low-light levels while maintaining a high signal-to-noise ratio.
This work is concerned with the analysis of degradation mechanisms resulting from the TDI mode operation and the impact of continuous charge accumulation on the image quality. At first, charge blooming originating from deactivated TDI stages is investigated. An anti-blooming clocking mechanism is deployed, and the impact of charge blooming on the sensor characteristics is shown experimentally. A method to identify blooming in TDI CCDs is presented. Further, two degradation effects resulting from the loss of charge carriers are thematized. For the degradation due to the falling edge of the applied clock, a one-dimensional analytical model, which describes the spatial-temporal behavior of the charge carrier density in a potential well, is derived. This solution results in an analytical expression for the temporal dependence of the total number of charge carriers containing all crucial sensor design parameters. This enables the investigation of the charge transfer efficiency (CTE) and the modulation transfer function (MTF), and the discussion of optimized design parameters.
Subsequently, the impact of defect states at the Si/SiO_2 interface is analyzed. The

continuous charge accumulation in a buried-channel TDI CCD causes the charge packets to approach the interface and interact with the defect states. Simulations of the charge transfer efficiency in dependence on the number of charge carriers are analyzed, and a model for determining the CTE for a TDI CCD is presented. Measurements are performed to prove these findings. A simple experimental method to determine the CTE is introduced.

Zusammenfassung

In den vergangenen Jahren ist das Interesse an hoch entwickelten optischen Bildsensoren für die Erdbeobachtung aufgrund einer wachsenden Anzahl von Anwendungen und potenzieller Märkte gewachsen. Diese Sensoren leiden jedoch im Allgemeinen, aufgrund der relativen Bewegung zwischen dem Satelliten und der Erde, unter einer kurzen Integrationszeit pro Pixel und beschränken so das Signal-Rausch Verhältnis. Um diese Nachteile zu überwinden, wurden Sensoren mit einer speziellen Architektur entwickelt, welche die Akkumulation von photogenerierten Elektronen aus Mehrfachbelichtungen ohne zusätzliches Rauschen ermöglichen. Sensoren, die diese Anforderungen erfüllen können, sind time-delay integration (TDI) CCDs. Diese Sensoren haben die Fähigkeit, sich schnell bewegende Objekte bei Lichtarmen Verhältnissen zu detektieren, während gleichzeitig ein hohes Signal-Rausch-Verhältnis beibehalten wird.
Diese Arbeit befasst sich mit der Analyse von Degradationsmechanismen, welche aus dem TDI Betriebsmodus und durch den Einfluss der kontinuierlichen Ladungsakkumulation resultieren und die Bildqualität beeinflussen. Zunächst wird Blooming von Ladungenträgern, welches aus deaktiven TDI Stufen herrührt, untersucht. Ein Anti-Blooming Mechanismus wird implementiert und der Einfluss von Blooming auf die Sensoreigenschaften wird experimentell gezeigt. Eine Methode um Blooming in TDI CCDs zu identifizieren wird präsentiert. Des Weiteren werden die Degradationseffekte, welche aus dem Verlust von Ladungsträgern resultieren, thematisiert. Für die Degradation durch eine fallenden Takt-Flanke der angelegten Clock wird ein ein-dimensionales analytisches Model, welches das räumliche und zeitliche Verhalten der Ladungsträgerdichte in einem Potentialtopf beschreibt, hergeleitet. Aus dieser Lösung ergibt sich ein analytischer Ausdruck für die zeitliche Abhängigkeit der Gesamtzahl der Ladungsträger, welcher alle wichtigen Design-Parameter beinhaltet. Das ermöglicht die Untersuchung der

Ladungstransfereffizienz und der Modulationtransferfunktion, und eine Diskussion über optimale Design-Parameter.
Anschließend wird der Einfluss von Defektzuständen an der Si/SiO_2-Grenzfläche analysiert. Die kontinuierliche Ladungsakkumulation einer TDI CCD führt dazu, dass sich die Ladungspakete der Grenzfläche annähern und folglich mit den Defektzuständen wechselwirken. Simulationen der Ladungstransfereffizienz in Abhängigkeit der Ladungsträgerzahl werden analysiert und ein Model zur Ermittlung der Ladungstransfereffizienz in einer TDI CCD wird präsentiert. Messungen werden durchgeführt um die Simulationsergebnisse zu bestätigen. Eine einfache experimentelle Methode, für die Bestimmung der Ladungstransfereffizienz, wird vorgestellt. Die Simulationen und experimentellen Ergebnisse werden mit den theoretischen Grundlagen verifiziert und eine Methode zur Identifizierung der Wechselwirkung von Ladungsträgern mit der Grenzfläche wird gezeigt.

Contents

List of Figures xv

List of Tables xvii

List of Abbreviations xix

List of Symbols xxi

1 Introduction 1

1.1 Motivation 1
1.2 Thesis Overview 2

2 Fundamentals of Silicon-Based Photodetection 5

2.1 MOS Capacitor 5
2.1.1 Depletion: Surface Channel 7
2.1.2 Depletion: Buried-Channel 10
2.2 Charge Generation and Collection 12
2.2.1 Photoelectric Effect 12
2.2.2 Charge Collection 16
2.3 Image Sensor 17
2.3.1 Charge-coupled Devices 17
2.3.2 CMOS Image Sensors 19
2.3.3 Modulation Transfer Function 21
2.3.4 Time-Delay Integration 23

3 Experimental Setup 29

3.1 Optoelectronic Measurement Setup 29
3.2 Design of the CMOS-TDI chip 30

3.3 Clock-Pattern 32

4 Anti-Blooming Mechanism **35**

4.1 Charge Blooming Effect 35

4.1.1 Blooming in the case of TDI-CCDs 36

4.1.2 Anti-Blooming Mechanism for TDI-CCDs 37

4.2 Experimental Results 38

4.2.1 Linear Camera Model 38

4.2.2 Responsivity 41

4.2.3 Photon Transfer Curve 43

4.2.4 Signal-to-Noise Ratio 47

4.3 Comparison and Interpretation 48

4.4 Influence of Blooming on Modulation 50

4.5 Summary 53

5 Charge Transfer Model for TDI **55**

5.1 Transfer Mechanisms 56

5.2 Transfer Dynamics 59

5.3 Transfer Analysis 62

5.3.1 Simulation of the Transfer Inefficiency 64

5.3.2 CTE and MTF 68

5.4 Discussion of Design Parameters 71

5.5 Summary 72

6 Impact of Interface States on TDI **73**

6.1 Carrier Exchange at the Interface States 74

6.2 Simulation of the Transfer Efficiency 76

6.2.1 Simulation Setup for Charge-Injection 76

6.2.2 Fill-and-Spill Method 77

6.2.3 Electrostatic Potential 79

6.2.4 Charge Transfer Efficiency 80

6.2.5 Charge Transfer Efficiency for TDI 82

6.3 Experimental Results 86

6.3.1 Experimental Setup 86

6.3.2 Method and Measurement 86

6.4 Summary 90

7 Conclusions and Outlook **91**

Publications and Conferences **98**

References **98**

List of Figures

2.1 Structures of a p-MOS and a n-p MOS capacitor. 6
2.2 Structure of the p-MOS capacitor and its energy band diagram with no applied voltage for $\Psi_{\mathrm{m}} < \Psi_{\mathrm{s}}$. 7
2.3 Energy band diagram of the MOS system at the flat-band condition. 8
2.4 Energy band diagram and charge carrier density of a MOS capacitor biased into surface depletion. 9
2.5 Structure of a buried-channel n-p MOS capacitor and the corresponding electrostatic potential. 11
2.6 Photon flux in dependence of the penetration depth for a wavelength of $\lambda = 850$ nm. 14
2.7 Measurement of the quantum efficiency. 15
2.8 Schematic cross-section of a buried-channel CCD during image integration. 16
2.9 Two-dimensional pixel array of a charge-coupled device. 18
2.10 Cross-section of a four-phase CCD and schematic diagram of the charge transfer. 19
2.11 Three-transistor pixel configuration 20
2.12 CMOS pixel array. 21
2.13 Modulation of an object an object, an image and the resulting MTF. 22
2.14 Schematic of a time-delay integration camera, the transfer of charge across the pixel column and the number of charge carriers for a corresponding TDI stage number. 24
2.15 Discrete MTF for various pixel apertures. 26

3.1 Block diagram of the measurement setup 30
3.2 Sections of the employed TDI-CCD. 31
3.3 T89022A chip photograph. 31

3.4 Design of the double source follower circuitry. 32
3.5 Four-phase, non-overlapping clock pattern with a line period of 466 clock cycles. 33

4.1 Cross-section of the TDI-CCD. 38
4.2 Timing scheme for TDI readout and anti-blooming mode. 39
4.3 Mathematical model of a simple pixel. 40
4.4 Responsivity curves measured without integration of the anti-blooming clocking for different numbers of TDI stages. 42
4.5 Offset versus photon number. 43
4.6 Responsivity curves measured with integration of the anti-blooming clocking for different numbers of TDI stages. 44
4.7 Illustration of an ideal photon-transfer curve. 45
4.8 PTCs with and without implemented anti-blooming clocking. . . . 46
4.9 SNR of the sensor with and without anti-blooming clocking, and the SNR of an ideal sensor. 48
4.10 Modulation for the measurements with and without anti-blooming mode. 51
4.11 Test pattern for various modulations. 52

5.1 Cross-section of a p-type CCD with applied gate voltages and the corresponding potential well. 58
5.2 Current flow in an infinitesimal slice of thickness dx. 60
5.3 Charge carrier distribution in the potential well for various n_0. . . 63
5.4 Spatial behavior of $n(x, t)$ at $t = 0$. 64
5.5 Time-dependent transfer inefficiency for various initial charge carrier densities n_0 in presence and absence of a fringing-field. 65
5.6 Transfer inefficiency ϵ in dependence on the fringing-field E_{ff} and the time t for a constant self-induced drift field. 67
5.7 CTE and MTF in dependence on the number of shifts N for various transfer inefficiencies ϵ. 69
5.8 Periodic bar pattern with increasing line pairs per mm for a pattern with perfect line edges and for two different levels of image degradation. 70

5.9 Relative luminance versus line pairs per mm for three different degradation models. 70

6.1 Four exchange mechanisms at the interface. 74
6.2 Cross-section a simulated CCD structure. 76
6.3 Charge injection structure and fill-and-spill method. 77
6.4 Clocking pattern for the fill-and-spill method. 78
6.5 Simulation of the injected charge and resulting capacitance for a buried-channel CCD according to the fill-and-spill method. 79
6.6 Electrostatic Potential for various signal levels. 80
6.7 Charge carrier density before and after transfer to an adjacent pixel. 81
6.8 Simulated charge transfer efficiency after one shift in dependence on the injected number of charge carriers. 82
6.9 Transfer efficiency γ after one shift process in dependence on the charge quantity for various trap concentrations. 83
6.10 Number of charge carriers for 64 shifts in dependence on the number of TDI stages. 84
6.11 CTE for 64 shifts in dependence on the number of charge carriers. 85
6.12 Mean gray values versus irradiance. 87
6.13 Transfer efficiency after 128 TDI stages and 16.7 kHz and 33.4 kHz line rate. 88
6.14 Measurement of the injected charge for a buried channel CCD and the capacitance in dependence on the number of charge carriers. . 89

List of Tables

2.1 Elemental and III-V semiconductors along with their bandgap energy and bandgap wavelength. 13
2.2 Clock pattern and their corresponding pixel apertures. 26

3.1 Signal levels for the pixel array. 34

4.1 Determined parameters for measurements with and without anti-blooming mechanism. 49

List of Abbreviations

ADC	Analog Digital Converter
CCD	Charge-Coupled Device
CDS	Correlated Double Sampling
CIS	CMOS Image Sensor
CMOS	Complementary Metal-Oxide-Semiconductior
CTE	Charge Transfer Efficiency
DN	Digital Numbers
EHP	Electron-Hole Pairs
FaS	Fill-and-Spill
FD	Floating Diffusion
FF	Fringing-Field
FPN	Fixed-Pattern Noise
FWC	Full-Well Capacity
HV	High Voltage
LED	Light Emitting Diode
LEO	Low Earth Orbit
MTF	Modulation Transfer Function
MOS	Metal-Oxide-Semiconductor
MOSFET	Metal-Oxide-Semiconductor Field-Effect Transistor
OTF	Optical Transfer Function
PD	Photodiode
PDE	Partial Differential Equation
PhTF	Phase Transfer Function
PRNU	Photo-Response Non-Uniformity
PSF	Point Spread Function
PTC	Photon-Transfer Curve

RS	Row Select
RST	Reset
S&H	Sample-and-Hold
SF	Source-Follower
SID	Self-Induced Drift
SNR	Signal-to-Noise Ratio
SRH	Shockley-Read-Hall
SW	Summing Well
TCAD	Technology Computer-Aided Design
TDI	Time-Delay Integration
TG	Transfer Gate
QE	Quantum Efficiency

List of Symbols

A_{px}	Pixel Area
C	Capacitance
C_{eff}	Effective Capacitance
C_{ox}	Oxide Capacitance
c	Speed of Light in Vacuum
D_{it}	Interface State Density
D_{n}	Diffusion Constant for Electrons
d_{max}	Location of Potential Maximum
E	Electric Field
E_0	Vacuum Level
E_{C}	Energy of the Conduction Band
E_{e}	Irradiance
E_{F}	Fermi Energy
E_{ff}	Fringing-Field
E_{g}	Energy width of the Band Gap
E_{i}	Intrinsic Fermi Energy
E_{sid}	Self-Induced Drift Field
E_{t}	Trap Energy level
E_{V}	Energy of the Valence Band
f	Frequency
f_{focal}	Focal Length
f_{line}	Line Frequency
f_{N}	Nyquist Frequency
g_{n}	Generation Rate of Electrons
G_{V}	Voltage Gain of the Source Follower
h	Planck Constant

I	Intensity
I_{max}	Maximum Intensity
I_{min}	Minimum Intensity
I_{ph}	Photo-Generated Current
j	Current Density
j_{diff}	Current Density for Diffusion
j_{ff}	Current Density for Fringing-Field Drift
j_{sid}	Current Density for Self-Induced Drift
K	Conversion Gain
k_{B}	Boltzmann Constant
L	Gate Length
L_{aperture}	Pixel Aperture
L_{px}	Pixel Pitch
L_{res}	Ground Resolution
M	Modulation
M_{img}	Image Modulation
M_{obj}	Object Modulation
N_{a}	Hole Concentration
N_{e}	Number of Electrons
N_{p}	Number of Photons
N_{d}	Electron Concentration
$N_{\mathrm{px.i}}$	Number of Electrons in Pixel i
N_{st}	Recombination Center Density
N_{TDI}	Number of TDI stages
N_{FW}	Full Well Charge Density
n	Charge Carrier Density
p_{s}	Surface Hole Concentration
Q_{dep}	Charge of the Depletion Layer
Q_{inj}	Injected Number of Charge Carriers
q	Elementary Charge
R	Responsivity
r_{n}	Recombination Rate of Electrons
S_{v}	Surface Recombination Velocity
T	Absolute Temperature

t	Time
t_{exp}	Exposure Time
U_{s}	Recombination Rate
V	Voltage
V_{fb}	Flat-Band Voltage
V_{g}	Gate Voltage
V_{D}	Diode Voltage
V_{DC}	Barrier Voltage
V_{drain}	Drain Gate Voltage
V_{IN}	Input or Injection Voltage
V_{out}	Output Voltage
V_{ox}	Oxide Voltage
V_{th}	Threshold Voltage
v_{th}	Thermal Velocity
W_{dep}	Width of the Depletion Layer
z	Penetration Depth
α	Absorption Coefficient
γ	Transfer Efficiency per Shift
ϵ	Transfer Inefficiency per Shift
ϵ_0	Vacuum Permittivity
ϵ_{r}	Relative Permittivity
ϵ_{si}	Permittivity of Silicon
η	Quantum Efficiency
λ	Wavelength
μ	Mobility
$\mu_{y.\mathrm{calc}}$	Calculated Mean Gray Values
$\mu_{y.\mathrm{meas}}$	Measured Mean Gray Values
μ_{y}	Mean Gray Value
$\mu_{\mathrm{y.dark}}$	Dark Offset
μ_{n}	Mobility of Electrons
μ_{h}	Mobility of Holes
Φ_{ph}	Photon Flux
ρ_{trap}	Recombination Center Density
σ	Standard Deviation

σ_{e}	Standard Deviation of Shot Noise
σ_{q}	Standard Deviation of Quantization Noise
σ_{d}	Standard Deviation of Distributed Noise
σ_{n}	Capture Cross Section of electrons
σ_{p}	Capture Cross Section of holes
τ	Time Constant
τ_{diff}	Time Constant for Diffusion
ϕ	Electric Potential
ϕ_{s}	Surface Potential
$\phi_{\mathrm{s,0}}$	Surface Potential at Zero Electric Charge
χ	Electron Affinity
χ_{s}	Electron Affinity for Semiconductor
Ψ	Work Function
Ψ_{s}	Work Function for Semiconductor
Ψ_{g}	Work Function for Gate Material

Chapter 1

Introduction

1.1 Motivation

The second half of the 20th century was filled with plenty of discoveries in the field of µ-electronics that initiated the digital century and formed our present age. Starting with the invention of the first Metal-Oxide-Semiconductor Field-Effect Transistor (MOSFET) by Bardeen, Shockley, and Brattain in 1959 [1] or the invention of the first integrated circuit by Kilby and Noyce in 1959 right up to the first microprocessor developed by Intel Corporation in 1971 [2]. Under all these notable inventions, the creation of digital imaging marked a breakthrough in industrial and scientific applications. This was possible thanks to the pioneering work of Willard S. Boyle and George E. Smith, who, in 1969, at Bell laboratories discovered that charge could be transferred along a shift register by placing many Metal-Oxide-Semiconductor (MOS) capacitors very close to each other [3][4]. This was the birth of the first Charge-Coupled Device (CCD). This discovery revolutionized photography so that light was now detected electronically. The impact on further applications was so immense that 40 years later, both were honored with the Nobel prize in physics [5]. Although the invention of the Complementary Metal-Oxide-Semiconductor (CMOS) sensor by Eric Fossum et al. in 1993 [6] led to a replacement of the CCD in consumer electronics and many other applications, there are up to now scientific applications where CCDs surpass CMOS sensors in terms of high-performance characteristics.
Therefore, it is no surprise that due to its unique properties, such as low readout noise and high sensitivity, CCDs are still the state of technology concerning space

applications.
Further challenges and requirements led to the development of CCDs which can be operated in Time-Delay Integration (TDI) mode. Time-delay integration denotes a special line scanning mode in which the image sensor is exposed multiple times to a moving object while the transfer of the signal charge is synchronized with the velocity of the moving object. This offers advantages at low light levels since, due to these multiple exposures, the effective exposure time and the electrical signal are increased while the Signal-to-Noise Ratio (SNR) remains low. The result is a greatly enhanced responsivity as well as the capability to detect moving objects. Consequently, TDI CCDs are deployed in particular for earth observation applications.

Time-delay integration charge-coupled devices are also the topic of this thesis. This work is primarily concerned with various operating modes of TDI CCDs and their physical properties regarding the accumulative nature of this integration mode. One way to accomplish this is to study the change of physical properties due to an increasing amount of charge carriers collected in the individual potential wells ("pixels") in terms of charge transfer efficiency. The second objective is to understand the influence of the deployed operating modes with respect to sensor characteristics.

Fortunately, while conventional CCDs are already investigated in great detail, TDI CCDs give rise to questions and offer a vast range of possibilities where improvements can be expected. Hence, the results obtained within the framework of this thesis might provide the opportunity for finding design rules applicable to sensor development due to a better understanding of the transfer behavior and an optimized choice of operating parameters.

1.2 Thesis Overview

In the **second chapter**, the concept of image sensors will be explained, starting with theoretical aspects of metal-oxide-semiconductor capacitors, followed by a depiction of the functioning of charge-coupled devices and active-pixel sensors.

The modulation transfer function and the time-delay integration scanning mode will be introduced and discussed for both of these sensor types.

The **third chapter** is reserved for an introduction of the experimental setup. A presentation of the structure and working principle of the employed TDI CCD sensor as well as the implemented timing pattern will be given.

Afterwards, in **chapter four**, blooming in TDI CCDs will be thematized. An anti-blooming mechanism will be deployed, and the functioning will be verified experimentally. A method for detecting blooming will be presented, and the impact on crucial sensor characteristics will be discussed.

The **fifth chapter** will present the derivation of an analytical model with respect to parameters enabling a detailed charge transfer analysis while considering the driving transfer mechanisms in relation to the clocking speed of the device.

Chapter six discusses the degradation of the transfer efficiency in buried-channel TDI CCDs due to interface (defect) states. Simulations and measurements are performed, investigating the impact and interaction of continuous accumulated charge carriers with the interface. Methods to determine the CTE for TDI CCDs are presented.

Finally, the results are summarized and discussed in the **last chapter**, and an outlook is given.

Chapter 2

Fundamentals of Silicon-Based Photodetection

The purpose of this chapter is to prepare the ground for the rest of this thesis, making a necessary introduction so that the contents of the following chapters will come in a natural way. Therefore, the following pages will present a description of the basic concepts related to charge-coupled devices. The first section of the chapter will thematize MOS capacitors which are the main component of many semiconductor devices. The second section discusses the functioning of charge-coupled devices and CMOS image sensors. Finally, an introduction to the modulation transfer function and a comparison of both sensors, relating the time-delay integration scanning mode, will be given.

2.1 MOS Capacitor

A charge-coupled device is an array composed of densely packed MOS capacitors, where the acronym MOS stands for Metal-Oxide-Semiconductor (MOS). These MOS capacitors are made of a doped silicon substrate, a thin dielectric layer, and a conductive gate. For this, a thin layer of Silicon-Dioxide (SiO_2) is grown on top of the doped semiconductor substrate by thermal oxidation. Since the gate-conductor needs to withstand high temperatures without reacting with the oxide, the deposited gate consists of heavily doped n^+-polycrystalline silicon making it highly conductive.

There are two designs of MOS capacitors, differing in the composition of the silicon substrate with regard to the doping structure, as the cross-sectional view in Figure 2.1 suggests. The p-MOS capacitor is only doped with acceptor atoms, resulting in an excess of holes in the substrate. Applying a positive voltage to the gate repels the holes from the Si/SiO_2 interface and induces an electric field where the electrostatic potential lies immediately at the surface. The dashed curve illustrates the electrostatic potential in Figure 2.1. As soon as minority charge carriers, in this case, electrons, are generated, they are attracted towards this interface where they are accumulated in the electrostatic potential maximum.

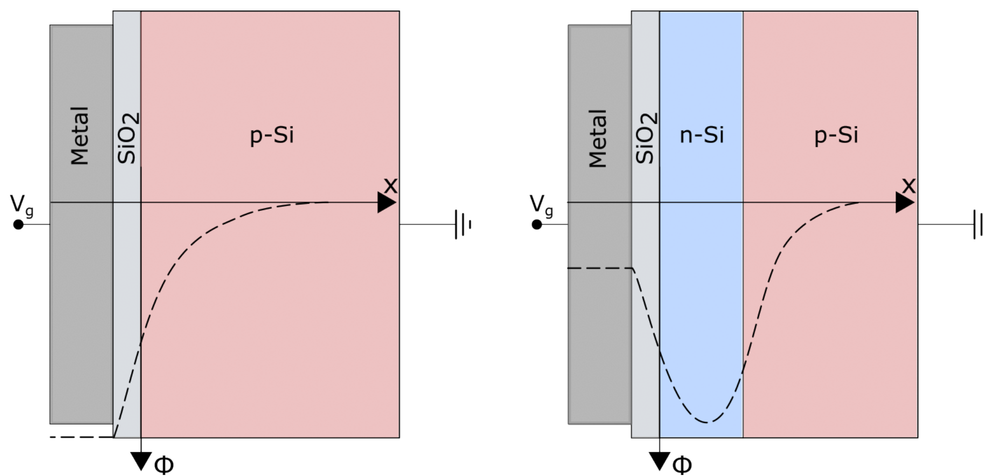

Figure 2.1: Structures of a p-MOS (left) and a n-p MOS capacitor (right). Dashed lines represent the electrostatic potentials of both types.

On the contrary, a n-p MOS capacitor contains an additional n-doped region called buried-channel. This type of MOS capacitor resembles a p-n junction, where a potential difference is formed across the p-n interface through the diffusion of the majority carriers into the opposite layer, respectively. Consequently, the resulting space charge region (or depletion layer) creates an electric field to compensate for the charge diffusion. Here, the electrostatic potential maximum, where the electrons are collected, is located within the n-type layer, i.e., with distance from the interface [7].

Depending on the applied voltage, the MOS capacitor can operate in different operational modes, called accumulation, depletion, and inversion. However, to operate a charge-coupled device, the depletion mode is essential. Therefore, the

subsequent subsections will provide a detailed discussion about the depletion mode, where crucial device design parameters can be introduced and discussed, necessary for the following chapters.

2.1.1 Depletion: Surface Channel

The contact of differing materials results in an alignment of the band diagrams throughout these materials. This is due to the dissimilarity of the electrochemical potentials, which cause a potential difference at the interface. The potential can be described by the work function Ψ, which is defined as the energy difference between the Fermi level and the vacuum level of the respective material [8].
In order to maintain an equilibrium state, charge carriers will transfer between these materials until the potential difference vanishes, and the Fermi levels align. Consequently, the direction of the electric field, i.e., the direction of charge transfer depends on the work function difference $\Delta\Psi = |\Psi_i - \Psi_j|$.
Considering a MOS-junction for the case $\Psi_\mathrm{m} < \Psi_\mathrm{s}$, where Ψ_m and Ψ_s denote the work functions for metal, respectively the semiconductor, electrons will flow from the semiconductor in direction of the metal. However, since both materials are divided by a dielectric film, the respective charge carriers will accumulate at the interfaces creating a depletion layer. As a result, a phenomenon called band bending occurs, causing the band diagram in the vicinity of the semiconductor interface to bend downwards. This can be seen in Figure 2.2. Contrary, the case $\Psi_\mathrm{m} > \Psi_\mathrm{s}$ yields an electric field in the opposite direction. Thus, the band diagram at the oxide-semiconductor interface would bend upwards.

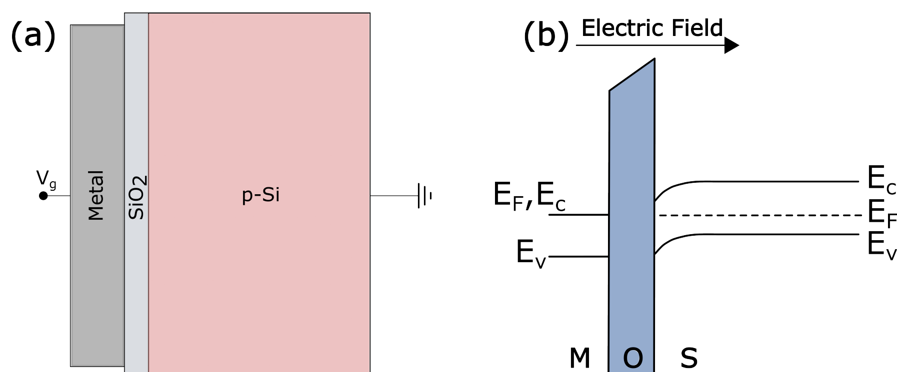

Figure 2.2: Structure of the p-MOS capacitor (a) and its energy band diagram with no applied voltage for $\Psi_\mathrm{m} < \Psi_\mathrm{s}$ (b).

The induced electric field in the depletion region can be neutralized by applying a gate voltage V_{g}, which corresponds to the opposite electric potential of the same absolute value. As a consequence, the energy band of the poly-silicon tends to be at the same level as the energy band of the silicon substrate yielding a flat energy band at the Si/SiO_2 interface since no depletion layer is present. This state is called flat-band condition and is shown in Figure 2.3. The voltage required to

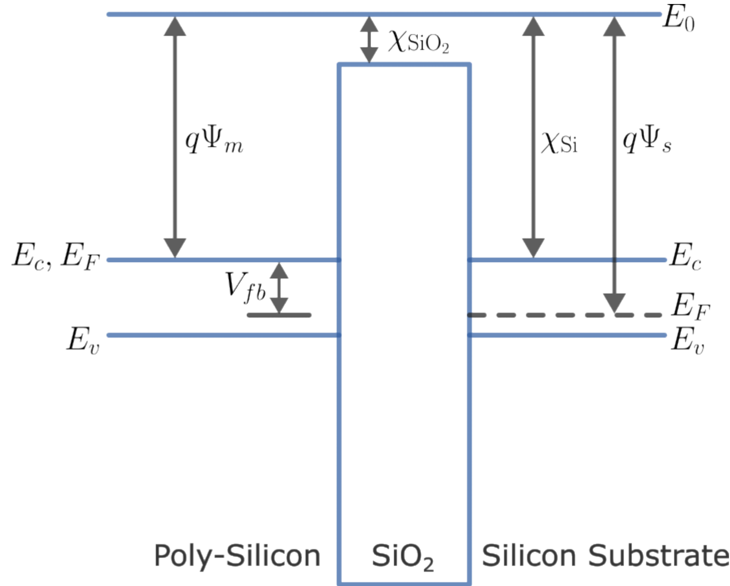

Figure 2.3: Energy band diagram of the MOS system at the flat-band condition for an applied voltage V_{fb}.

achieve this condition is called flat-band voltage V_{fb} and results from the difference

$$V_{\mathrm{fb}} = \Psi_{\mathrm{m}} - \Psi_{\mathrm{s}} = \Psi_{\mathrm{m}} - \left(\chi_{\mathrm{si}} + \frac{E_{\mathrm{g}}}{2\mathrm{q}} - \psi_{\mathrm{b}}\right), \tag{2.1}$$

where the electron affinity χ_{si} is defined as energy required to move an electron from the conduction to the vacuum level E_0, E_{g} is the width of the band gap, i.e. $E_{\mathrm{g}} = E_{\mathrm{C}} - E_{\mathrm{V}}$ and ψ_{b} is the difference of the Fermi level E_{F} and the intrinsic Fermi level $E_{\mathrm{i}} = E_{\mathrm{V}} + \frac{E_{\mathrm{g}}}{2}$ [9].
The flat-band voltage can be related to the gate voltage, the surface potential ϕ_s and the oxide voltage V_{ox} by using Kirchhoff's voltage equation for a MOS capacitor [10]:

$$V_{\mathrm{g}} - V_{\mathrm{fb}} = \phi_{\mathrm{s}} + V_{\mathrm{ox}}. \tag{2.2}$$

Here, the oxide Voltage depends on the oxide thickness d_{ox}, and the polarity and absolute value of the surface potential which again depend on the substrate type and the doping concentration.

In surface depletion mode, a positive voltage is applied to the polysilicon gate, causing the Fermi level on the gate side to fall while the Fermi level in the semiconductor rises [11]. Consequently, the semiconductor's energy bands bend downwards and yield a positive surface potential ϕ_{s} as seen in Figure 2.4. The

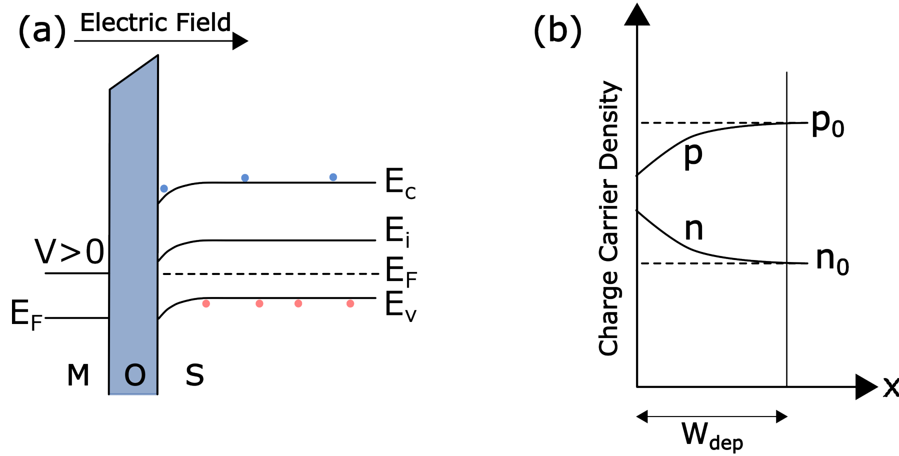

Figure 2.4: Energy band diagram (a) and charge carrier density (b) of a MOS capacitor biased into surface depletion.

positive charge at the metal-oxide junction causes the majority of carriers near the semiconductor-oxide junction to ionize due to recombination with electrons. This creates a negatively charged layer Q_{dep} of width

$$W_{\mathrm{dep}} = \sqrt{\frac{2\epsilon_{\mathrm{si}}\phi_{\mathrm{s}}}{\mathrm{q}N_{\mathrm{a}}}} \tag{2.3}$$

which is called depletion layer. Consequently, the oxide voltage is given by using Gauss' Law

$$\Phi_{\mathrm{ox}} = -\frac{Q_{\mathrm{dep}}}{\epsilon_{\mathrm{ox}}}, \tag{2.4}$$

respectively

$$V_{\mathrm{ox}} = \Phi_{\mathrm{ox}} d_{\mathrm{ox}} = -\frac{Q_{\mathrm{dep}}}{C_{\mathrm{ox}}} = \frac{\mathrm{q}N_{\mathrm{a}}W_{\mathrm{dep}}}{C_{\mathrm{ox}}} = \frac{\sqrt{\mathrm{q}N_{\mathrm{a}}2\epsilon_{\mathrm{si}}\phi_{\mathrm{s}}}}{C_{\mathrm{ox}}} \tag{2.5}$$

and thus results in

$$V_{\mathrm{g}} = V_{\mathrm{fb}} + \phi_{\mathrm{s}} + V_{\mathrm{ox}} = V_{\mathrm{fb}} + \frac{\mathrm{q}N_{\mathrm{a}}W_{\mathrm{dep}}^2}{2\epsilon_{\mathrm{si}}} + \frac{\mathrm{q}N_{\mathrm{a}}W_{\mathrm{dep}}}{C_{\mathrm{ox}}}. \tag{2.6}$$

This equation contains the dependencies of all crucial device parameters, such as gate voltage, doping density, and oxide thickness. By solving this equation for the surface potential ϕ_{s}, the expression

$$\phi_{\mathrm{s}} = V_{\mathrm{g}} - V_{\mathrm{fb}} + \frac{\mathrm{q}N_{\mathrm{a}}\epsilon_{\mathrm{si}}}{C_{\mathrm{ox}}^2} + \frac{Q_{\mathrm{sig}}}{C_{\mathrm{ox}}} - \frac{1}{C_{\mathrm{ox}}}\left[2\mathrm{q}N_{\mathrm{a}}\epsilon_{\mathrm{si}}\left(V_{\mathrm{g}} - V_{\mathrm{fb}} + \frac{Q_{\mathrm{sig}}}{C_{\mathrm{ox}}}\right) + \left(\frac{\mathrm{q}N_{\mathrm{a}}\epsilon_{\mathrm{si}}}{C_{\mathrm{ox}}}\right)^2\right]^{1/2} \tag{2.7}$$

is obtained [10]. Varying these parameters allow for examining the surface potential behavior and, consequently, the potential wells and barriers. Furthermore, a calculation of the full-well capacity (FWC) can be carried out, which is defined as the amount of charge a pixel can store before it reaches saturation. Thus, Equation 2.7 contains all quantities relevant for describing the properties of a charge-coupled device. These quantities will be used in Chapters 6 and 7 while analyzing the transfer efficiency.

2.1.2 Depletion: Buried-Channel

The electrostatic analysis of a p-MOS capacitor presented in the previous section can be carried out equivalently for an n-p MOS capacitor. Looking at Figure 2.5, one can derive the relation between the depicted potentials. Subsequently, Kirchhoff's voltage law yields [10]

$$\phi_{\mathrm{s}} + V_{\mathrm{g}} - V_{\mathrm{fb}} + V_{\mathrm{ox}} = \phi_{\mathrm{max}}, \tag{2.8}$$

where $\phi_{\mathrm{max}} = \phi_{\mathrm{c}} + \phi_{\mathrm{j}}$.

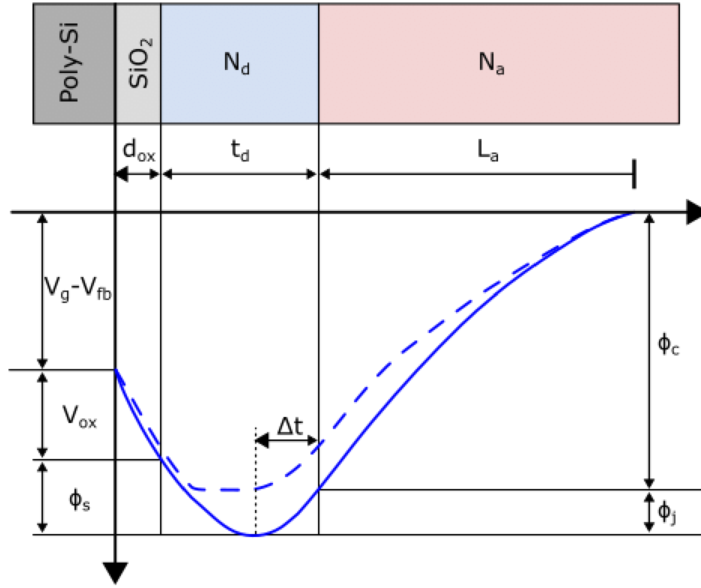

Figure 2.5: Structure of a buried-channel n-p MOS capacitor and the corresponding electrostatic potential. Solid line is the electrostatic potential for an empty potential well and dashed line corresponds to a potential well with $Q \neq 0$.

By applying the p-n junction theory and using Gauss' law, we obtain the oxide voltage V_{ox}

$$V_{\mathrm{ox}} = \Phi_{\mathrm{ox}} d_{\mathrm{ox}} = \frac{\mathrm{q} N_{\mathrm{d}} (t_{\mathrm{d}} - \Delta t - Q_{\mathrm{sig}}/N_{\mathrm{d}}) d_{\mathrm{ox}}}{\epsilon_{\mathrm{ox}}}. \tag{2.9}$$

Further, we can determine the surface potential

$$\phi_{\mathrm{s}} = \frac{\mathrm{q} N_{\mathrm{d}}}{2\epsilon_{\mathrm{si}}} \left(t_{\mathrm{d}} - \Delta t - \frac{Q_{\mathrm{sig}}}{N_{\mathrm{d}}} \right)^2 \tag{2.10}$$

and the potentials

$$\phi_{\mathrm{j}} = \frac{\mathrm{q} N_{\mathrm{d}} (\Delta t)^2}{2\epsilon_{\mathrm{si}}} \quad \text{and} \quad \phi_{\mathrm{c}} = \frac{\mathrm{q} N_{\mathrm{a}} L_{\mathrm{a}}^2}{2\epsilon_{\mathrm{si}}} \tag{2.11}$$

with $L_{\mathrm{a}} = \frac{N_{\mathrm{d}} \Delta t}{N_{\mathrm{a}}}$. Combing these relations with Equation 2.8 yields

$$\begin{aligned}
\phi_{\max} = \Bigg[&- \left(\frac{\mathrm{q}\epsilon_{\mathrm{si}}}{2} \frac{N_{\mathrm{a}}(N_{\mathrm{d}} + N_{\mathrm{a}})}{N_{\mathrm{d}}} \right)^{1/2} \left(\frac{d_{\mathrm{ox}}}{\epsilon_{\mathrm{ox}}} + \frac{t_{\mathrm{d}}}{\epsilon_{\mathrm{si}}} - \frac{Q_{\mathrm{sig}}}{N_{\mathrm{d}}\epsilon_{\mathrm{si}}} \right) \\
&+ \Bigg[\frac{\mathrm{q}\epsilon_{\mathrm{si}}}{2} \frac{N_{\mathrm{a}}(N_{\mathrm{d}} + N_{\mathrm{a}})}{N_{\mathrm{d}}} \left(\frac{d_{\mathrm{ox}}}{\epsilon_{\mathrm{ox}}} + \frac{t_{\mathrm{d}}}{\epsilon_{\mathrm{si}}} - \frac{Q_{\mathrm{sig}}}{N_{\mathrm{d}}\epsilon_{\mathrm{si}}} \right)^2 \\
&+ \frac{N_{\mathrm{d}} + N_{\mathrm{a}}}{N_{\mathrm{d}}} \left(V_{\mathrm{g}} - V_{\mathrm{fb}} + V_{\mathrm{I}} - \mathrm{q}N \left(\frac{d_{\mathrm{ox}}}{\epsilon_{\mathrm{ox}}} + \frac{t_{\mathrm{d}}}{\epsilon_{\mathrm{si}}} - \frac{Q_{\mathrm{sig}}}{N_{d}\epsilon_{\mathrm{si}}} \right) \right) \Bigg]^{1/2} \Bigg]^2
\end{aligned} \tag{2.12}$$

where

$$V_{\mathrm{I}} = \mathrm{q}N_{\mathrm{d}}t_{\mathrm{d}} \left(\frac{d_{\mathrm{ox}}}{\epsilon_{\mathrm{ox}} + \frac{t_d}{2\epsilon_{\mathrm{si}}}} \right), \tag{2.13}$$

is the voltage required to deplete the p-n junction.

As can be concluded from Equation 2.12, the maximum potential ϕ_{max} scales in dependence on the gate Voltage V_{g}, the oxide thickness d_{ox}, and the thickness of the buried-channel t_{d}. Moreover, according to Equation 2.13, a higher doping concentration N_{d} and a thicker oxide d_{ox} lead to a higher voltage, necessary for a full channel depletion. Hence, the buried-channel MOS capacitor shows the same dependencies as the surface-channel device, however, with an additional dependence on the doping concentration of the n-channel.

Comparing the surface-channel with the buried-channel device, the latter exhibits a higher transfer speed of the charge carriers [12] since it provides more favorable transfer conditions in terms of internal electric fields. Moreover, since the buried-channel device collects the charge displaced from the surface, a lower noise (dark current) is achieved due to the absence of defect states at the Si/SiO_2 interface [13]. However, the charge-carrying capability, as well as the full-well capacity, is reduced compared to a surface-channel device. Nevertheless, nowadays, all scientific CCDs are produced with a buried-channel since the advantages outweigh the disadvantages.

2.2 Charge Generation and Collection

The previous section introduced MOS capacitors and presented the theoretical fundamentals of the depletion mode. With this in mind, the primary tasks of a CCD can be discussed: charge generation, charge collection, and charge transfer. The latter will be thematized in Section 2.3.1, while discussing the functioning of a CCD.

2.2.1 Photoelectric Effect

Photons hitting a semiconductor substrate can create electron-hole pairs (EHP) via the photoelectric effect if the energy of the incident photons is larger than the

bandgap energy of the material. This is necessary in order to excite an electron from the silicon valance band to the conduction band. Thus, the condition

$$E_\mathrm{g} \leqslant E_\lambda = \frac{\mathrm{hc}}{\lambda}, \tag{2.14}$$

has to be fulfilled, where h is Planck's constant and c is the speed of light. Hence, the material is sensitive to all wavelengths shorter than λ_g, i.e.,

$$\lambda \leqslant \lambda_\mathrm{g} = \frac{\mathrm{hc}}{E_\mathrm{g}}. \tag{2.15}$$

Table 2.1 lists a selection of elemental and III-V semiconductors, as well as their bandgap energy E_g and the corresponding wavelength λ_g.

Table 2.1: Elemental and III-V semiconductors along with their bandgap energy and bandgap wavelength (after [14]).

Material	**Bandgap Energy (eV)**	**Bandgap Wavelength (μm)**
Si	1.12	1.11
Ge	0.66	1.88
AlN	6.02	0.206
GaAs	1.42	0.873
InAs	0.36	3.44
InSb	0.17	7.29

Consequently, silicon-based devices are sensitive to wavelengths shorter than 1100 nm. However, the wavelength-dependent probability of photon-absorption scales exponentially with the thickness of the substrate material.
Therefore, the photon flux $\Phi_\mathrm{ph}(z)$ as a function of the depth z can be expressed as

$$\Phi_\mathrm{ph}(z) = \Phi_\mathrm{ph.0} e^{-\alpha \cdot z}, \tag{2.16}$$

where α is the absorption coefficient of the substrate material and $\Phi_\mathrm{ph.0} = \frac{\lambda E_\mathrm{e}}{\mathrm{hc}}$ denotes the photon flux at the surface. The e-h-pair generation rate regarding an area A is determined according to

$$G(z,t) = -\frac{\mathrm{d}}{\mathrm{d}z}\Phi_\mathrm{ph}(z) \cdot A = \frac{A\lambda E_\mathrm{e}(t)}{\mathrm{hc}} \cdot \alpha \cdot \mathrm{e}^{-\alpha \cdot z}, \tag{2.17}$$

with the irradiance $E_e(t)$.

Consequently, the photon flux at a wavelength $\lambda = 850$ nm with a corresponding absorption coefficient of $\alpha = 5.35 \cdot 10^2$ cm^{-1} [15][16] can be calculated. Figure 2.6 shows the photon flux in dependence on the penetration depth.

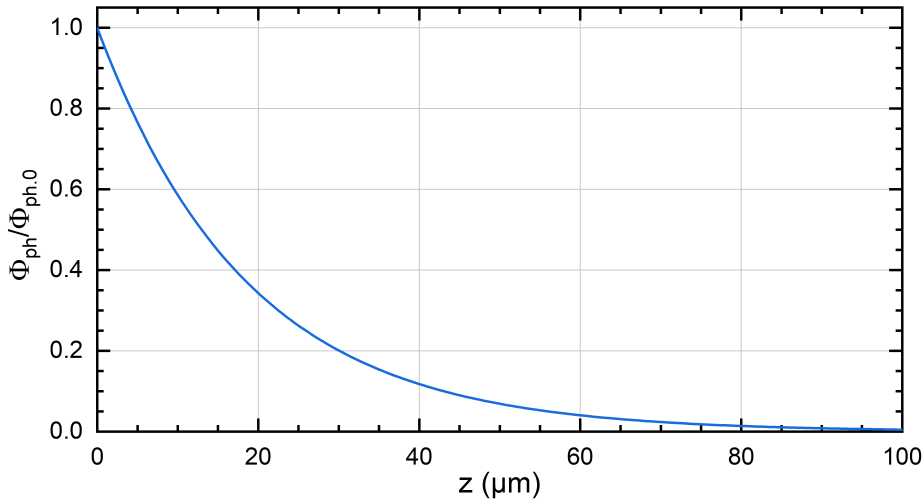

Figure 2.6: Photon flux in dependence of the penetration depth for a wavelength of $\lambda = 850$ nm and an absorption coefficient $\alpha = 5.35 \cdot 10^2$ cm^{-1}.

The probability that an incoming photon of a particular wavelength λ generates an electron is called quantum efficiency (QE) and can be defined as the ratio of photo-generated electrons to the number of incident photons

$$\eta = \frac{N_\mathrm{e}}{N_\mathrm{p}} = \frac{I_\mathrm{ph}(t_\mathrm{int})}{\mathrm{q}} \cdot \frac{\mathrm{hc}}{\lambda(t_\mathrm{int})\Phi}, \tag{2.18}$$

where I_{ph} is the photo-generated current in Ampere and t_{int} the integration time. The dataset for a quantum efficiency measurement on a silicon-based device was fitted and is shown in Figure 2.7.

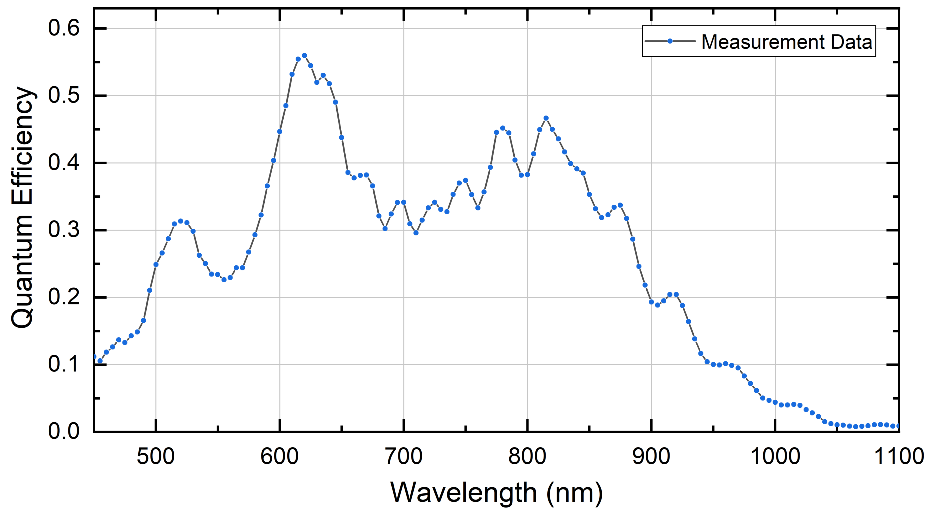

Figure 2.7: Measurement of the quantum efficiency.

The course of the QE measurement is characteristic of front-side illuminated silicon-based devices and relates to the sensor used in this thesis (see Section 3.2). In the beginning, the sensor shows a reduced blue response caused due to the polysilicon, which absorbs photons of shorter wavelengths and attenuates the number of photons reaching the silicon. As the wavelength increases, the energy of the photons decreases resulting in a higher penetration depth. Consequently, more photons reach the silicon and contribute to a higher QE. Here it should be kept in mind that due to optical effects, such as reflection and transmission, only a fraction of the incident photons create ehp. Furthermore, if the penetration depth is too long, ehp can be generated in silicon regions where no electrostatic potential is present. Thus, the generated electrons will not be attracted and collected in the potential maximum. Instead, the ehp recombine or diffuse in other regions of the device. As a result, the QE is considerably reduced, as can be seen for wavelengths $\lambda > 900$ nm.

Therefore, the penetration depth and the acting electric field along the silicon impact the QE. Thus, the doping concentration and the thickness of the buried n-layer and p-layer can be adjusted to provide a high QE at desired particular wavelengths. The quantum efficiency and the measurement shown in Figure 2.7 will be used to verify the reliability of measurements in subsequent chapters.

2.2.2 Charge Collection

During the image integration specific electrodes in each pixel with positive applied voltage on their gates form potential wells. Simultaneously the adjacent electrodes with lower applied voltages act as potential barriers. As a consequence, the photogenerated electrons are attracted towards the most positive voltage, where they are stored in the potential well. Figure 2.8 shows a schematic depiction of the collection process. As can be seen, the photoelectrons generated within a pixel are accumulated under their corresponding gate electrodes. Here, the size of the charge packet is generally proportional to the number of incoming photons. As electrons are stored in the potential well, the depletion region

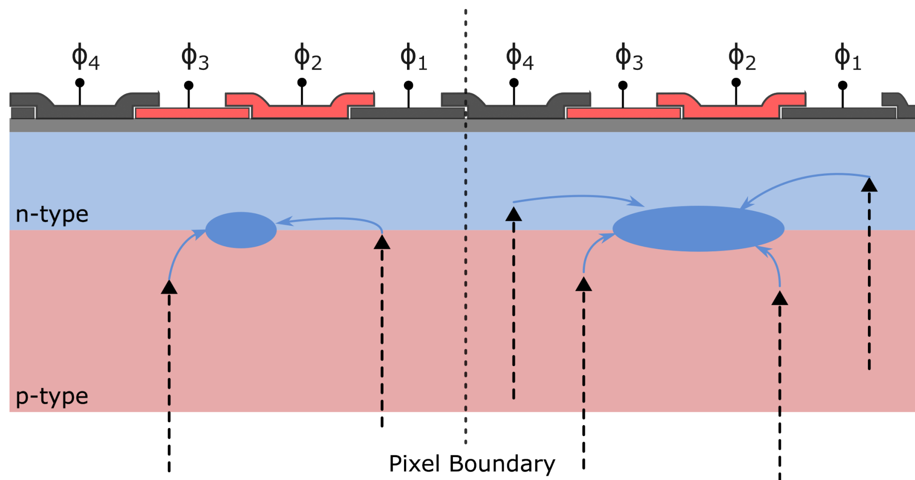

Figure 2.8: Schematic cross-section of a buried-channel CCD. Black arrows indicate incoming photons, and blue arrows the generated electrons. Blue ellipses represent the charge packets. The electrons are collected under gates with positive applied voltages ϕ_3 and ϕ_2, while ϕ_4 and ϕ_1 act as barriers: $\phi_3 = \phi_2 > \phi_4 = \phi_1$.

becomes less depleted, i.e., the depletion region becomes smaller, the potential maximum moves towards the Si/SiO$_2$ interface, and the effective capacitance increases. Here the effective capacitance for a buried-channel CCD can be expressed by [10]

$$C_{\text{eff}}^{-1} = \frac{d_{\text{ox}}}{\epsilon_{\text{ox}}} + \frac{1}{\epsilon_{\text{si}}}\left(t_{\text{d}} - \Delta t - \frac{Q_{\text{sig}}}{2N_{\text{d}}}\right) \tag{2.19}$$

where Q_{sig} is the accumulated signal charge.

The maximum amount of charge a pixel can collect is defined as full-well capacity,

which is generally dependent on the pixel size, as well as the effective capacitance and doping concentration. According to the definition, the FWC is reached when the signal charge compensates the donator atoms located between Si/SiO_2 interface and the potential maximum [17]. Thus, the full well charge density can be calculated with

$$N_{\mathrm{FW}} = N_{\mathrm{d}}(t_{\mathrm{d}} - \Delta t). \tag{2.20}$$

However, the doping concentration of the buried-channel can not be arbitrarily increased since the required gate voltage for depletion scales with doping concentration too. The effective capacitance C_{eff} and the full-well capacity N_{FW} significantly affect the charge transfer and the image quality, as will be shown in the following chapters.

2.3 Image Sensor

This section intends to describe the functioning of the two main types of image sensors: the charge-coupled device and the CMOS sensor. In this context, the modulation transfer function and the time-delay integration mode will be introduced, discussed, and compared for both types of image sensors in the following subsections.

2.3.1 Charge-coupled Devices

A charge-coupled device consists of several light-sensitive pixels, which are either arranged linearly or in a two-dimensional array (see Figure 2.9). Each of these pixels contains a particular number of densely placed MOS capacitors of which electrodes are separately connected to a clock-pulse generator. Hence, this structure enables the storage, as well as the transport of accumulated charge carriers located under the electrodes of each pixel [3].

The clock-pulse generator repeats periodically for each pixel while their number corresponds to the type of clocking used to transfer the charge along the shift register [18]. Exemplary, in a four-phase device the electrodes are connected to four clock drivers ϕ_1, ϕ_2, ϕ_3 and ϕ_4. This means that every fourth electrode is connected to the same clock phase by the same electrical connection, as seen

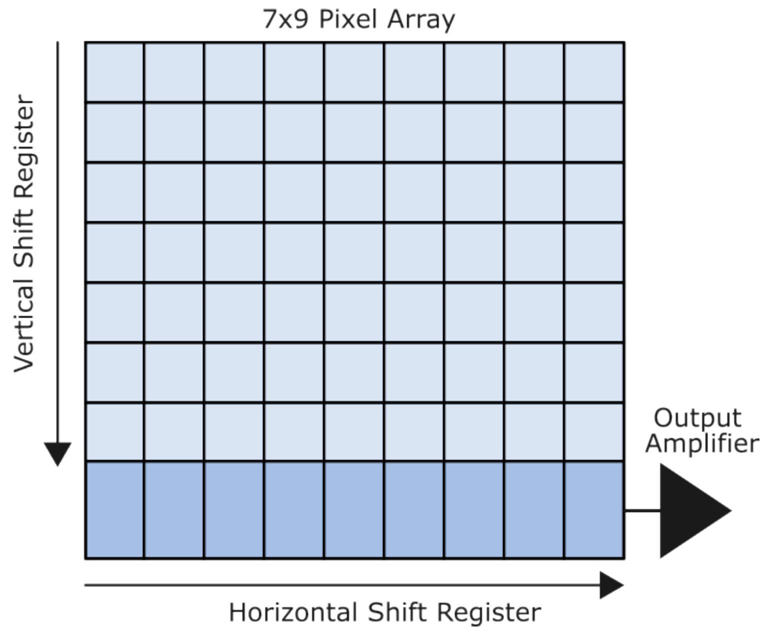

Figure 2.9: Two-dimensional pixel array. Each pixel consists of 4 phases.

in Figure 2.10. Depending on the applied voltage, the electrodes of each pixel form either a barrier or a potential well. During the integration process, where no charge shifting occurs, the photon-induced charges will be generated in the silicon substrate and attracted towards the local potential maximum (= potential well). Thus, the generated electrons are collected in their respective potential wells, where the number of electrons per pixel depends on their local exposure to light. Hereafter, the collected charge carriers are shifted gradually from one potential well to an adjacent one. This takes place by shaping and reshaping the form of the potential wells through variations of the applied voltages [19]. A schematic diagram of the transfer process for a four-phase CCD is shown in Figure 2.10.

During the integration process at the time $t_{1\text{-}1}$, the gate ϕ_4 and ϕ_3 form a potential well to collect charge carriers while the applied voltages on ϕ_2 and ϕ_1 form a potential barrier. To shift the charge across the CCD, a positive voltage on ϕ_2 is applied at $t_{1\text{-}2}$. Consequently, the potential well widens and the charge redistributes under the electrodes ϕ_4, ϕ_3 and ϕ_2. By switching the polarity of the voltage at ϕ_4 to negative, the electrode pushes the charge under this electrode away while forming a barrier. Hence, at $t_{1\text{-}3}$ the charge is located under ϕ_3 and ϕ_2 [20]. Thus, transferring the charge from one pixel to an adjacent one requires eight clocking cycles in the case of a four-phase device.

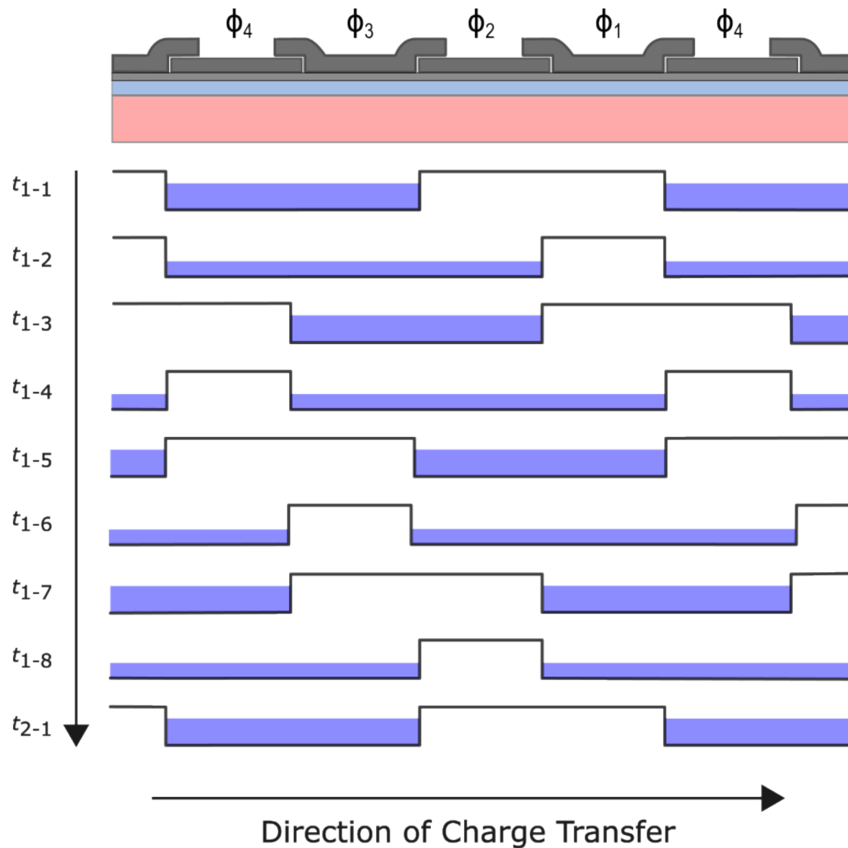

Figure 2.10: Cross-section of a four-phase CCD (top). Schematic diagram of the charge transfer (bottom).

Repeating this transfer procedure allows the charge packets to be shifted along the whole pixel column until the serial register is reached. The charge-to-voltage conversion is performed within the serial register at the sense node. This voltage is then buffered by an output amplifier and converted to a digital signal by an analog-to-digital converter (ADC) [21].

2.3.2 CMOS Image Sensors

A CMOS image sensor is an array of photosensitive elements where each element converts the photo-generated charge directly into a voltage. For this, each pixel of this array consists of a pinned photodiode, a floating diffusion, and several MOSFETs which perform different tasks [6]. A basic pixel configuration constituting of three transistors (3-Tr pixel configuration) is shown in Figure 2.11.

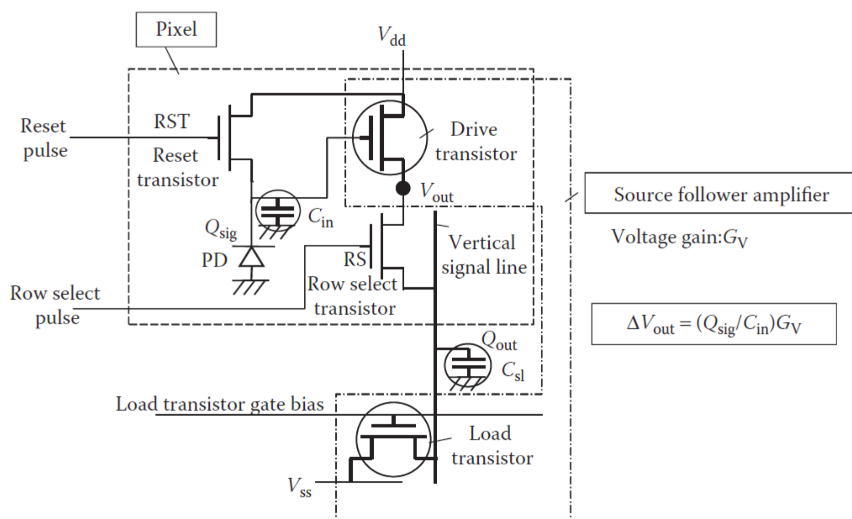

Figure 2.11: Three-transistor (3-Tr) pixel configuration consisting of a reset transistor, a drive transistor, and a row select transistor [20].

The floating diffusion of the photodiode (PD) is connected to the gate of a drive transistor and to a reset transistor (RST), which acts as a switch between the floating diffusion and the voltage source V_{dd}. By operating the reset transistor in ohmic mode, i.e., turning it on, all generated electrons are removed, and the potential of the photodiode is reset to V_{dd}.
The generation of signal charge Q_{sig} in the floating diffusion results in a change of the applied voltage on the drain gate, which can be calculated according to

$$V_{\text{drain}} = V_{\text{in}} + \frac{Q_{\text{sig}}}{C_{\text{in}}}, \tag{2.21}$$

where $V_{\text{dd}} = V_{\text{in}}$ and the voltage $V_{\text{sig}} = Q_{\text{sig}}/C_{\text{in}}$ is of negative polarity in the case of electrons [20]. Since the drive transistor operates like a resistor dependent on the applied gate voltage, the output voltage V_{out} varies for different numbers of generated electrons. The output voltage V_{out} can be calculated with the equation

$$V_{\text{out}} = -\frac{Q_{\text{sig}}}{C_{\text{in}}} G_{\text{V}} + (V_{\text{dd}} - V_{\text{th}}) G_{\text{V}} \tag{2.22}$$

where G_{V} denotes the voltage gain of the source follower and V_{th} is the threshold Voltage.
This output of the drive transistor is then connected to the vertical signal line by the row select transistor. The vertical signal line connects all vertical pixels with

the transversal signal line as depicted in Figure 2.12. Consequently, the sensor is read out row-wise by the read-out electronics [22].

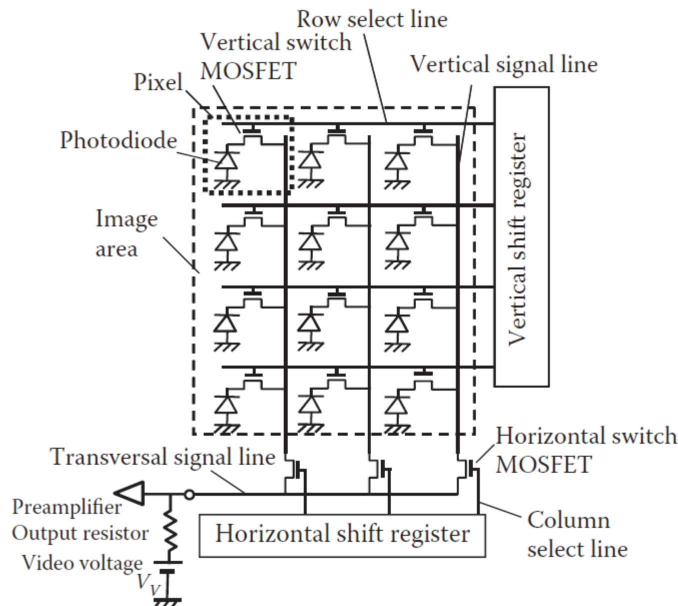

Figure 2.12: CMOS pixel array [20].

2.3.3 Modulation Transfer Function

The modulation transfer function (MTF) is one of the main parameters for measuring the image quality and will be used frequently in the subsequent chapters of this thesis. Therefore this section is intended to introduce the fundamentals regarding this quantity.

The modulation transfer function is defined as the magnitude response of an optical system to sinusoids of different spatial frequencies. A periodic pattern of spatial variations in terms of contrast can be described by modulation

$$M = \frac{I_{\mathrm{max}} - I_{\mathrm{min}}}{I_{\mathrm{max}} + I_{\mathrm{min}}} \tag{2.23}$$

where I_{max} and I_{min} denote this pattern's highest and lowest intensity. Due to the optical system's limited spatial resolution, the image's resulting modulation will be degraded compared to the object's modulation. Hence, the degradation of the modulation increases for increasing spatial frequencies since the ability to depict the contrast decreases.

The ratio of modulation in the image to that in the object as a function of spatial frequency f is defined as modulation transfer function

$$\mathrm{MTF}(f) := \frac{M_{\mathrm{img}}(f)}{M_{\mathrm{obj}}} \tag{2.24}$$

This is also exemplified in Figure 2.13. The first graphs on the left-hand side show the object's and the image's modulation in dependence on their spatial frequency. Here the modulation of the object corresponds to an idealized image without loss of contrast. Below this, the modulation of the image is depicted, whose amplitude decreases for higher spatial frequencies. Calculating the ratio of both modulations results in the MTF shown on the right.

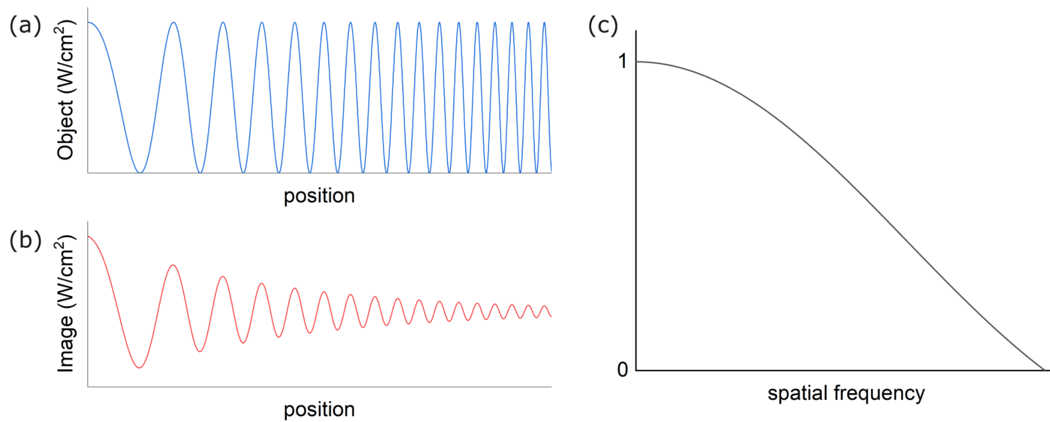

Figure 2.13: (a) Modulation of the object. (b) Modulation of the image. (c) The decrease of modulation depth with increasing spatial frequency yields the MTF and can be obtained from the ratio of both modulations.

An overall optical System consists of several subsystems such as optics, detector, and electronics. Consequently, the total MTF of this optical System is the product of all MTF contributions:

$$\mathrm{MTF}_{\mathrm{total}} = \prod_i \mathrm{MTF}_i \tag{2.25}$$

Of particular interest is the MTF of an image sensor, which is determined and influenced by the effective sampling aperture L.

In general, the MTF of an electro-optical device can be calculated by the Fourier

transform of the point spread function (PSF), defined as an optical system's impulse response.
Considering a square detector of size $L \times L$ and a constant PSF centered at x_0 [23]:

$$p(x) = p_0 \quad \text{for} \quad x_0 - L/2 \leqslant x \leqslant x_0 + L/2. \tag{2.26}$$

The Fourier transform of the PSF yields

$$\mathcal{F}(f) = \int_{-\infty}^{\infty} p(x) \mathrm{e}^{i2\pi f x} \mathrm{d}x = p_0 \frac{\sin(\pi f L)}{\pi f} \mathrm{e}^{i2\pi f x_0} := \mathrm{OTF}(f), \tag{2.27}$$

which is defined as optical transfer function (OTF).

The OTF is a complex function combining the MTF and a frequency-dependent phase denoted as phase transfer function (PhTF). Hence, the OTF can be expressed generally as

$$\mathrm{OTF}(f) = \mathrm{MTF}(f) \cdot \exp(-i\mathrm{PhTF}(f)), \tag{2.28}$$

where the PhTF describes a displacement of the image in relation to a perfect optical system [22]. In order to obtain the MTF, the absolute value of the OTF, i.e., the amplitude, has to be considered:

$$\mathrm{MTF}(f) = |\mathrm{OTF}(f)| = |\mathrm{sinc}(fL)|, \tag{2.29}$$

where

$$\mathrm{sinc}(x) = \frac{\sin(\pi x)}{\pi x} \tag{2.30}$$

is the normalized sinc function (*sinus cardinalis*). According to this equation, the MTF decreases for higher spatial frequencies and sampling apertures. Moreover, this expression allows the calculation of MTFs resulting from different origins and is therefore significant for analyzing the image quality for a particular optical system.

2.3.4 Time-Delay Integration

In modern remote sensing systems low-light-level detection capabilities are required, which can be provided by image sensors operated in Time-Delay Inegration mode. Time-delay integration is a special scanning mode in which a moving

image is integrated multiple times over a number of stages. Due to the cumulative exposure of the sensor, the effective exposure time increases, resulting in an increased number of charge carriers within the pixels [24].
This is often realized by using line-scan cameras based on charge-coupled devices, where the transfer of the photo-generated charge packet is synchronized with the relative movement of this image, as can be seen in Figure 2.14.

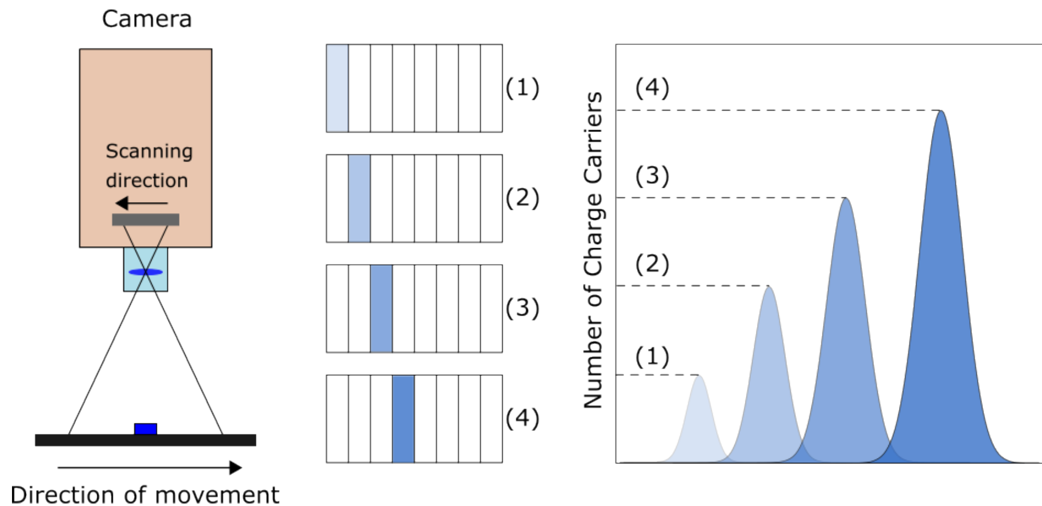

Figure 2.14: Schematic of a time-delay integration camera (left). Transfer of charge across the pixel column (middle). Number of charge carriers for a corresponding TDI stage number (right).

The continuous generation of charge carriers after N stages results in a total photon shot noise of $\sim N^{1/2}$. Nevertheless, since the accumulated charge packet is only read out once at the output, the total readout noise is independent of the number of stages N. Hence, a TDI CCD sensor allows the summation of photogenerated charge carriers from multiple exposures without additional readout noise, resulting in a high signal-to-noise ratio.
Another approach to realizing TDI mode is using CMOS image sensors (CIS), where the summing of the signal takes place externally after the charge is converted to a voltage. Hence, this method is also called digital TDI. Using a CMOS image sensor provides a fast readout and an equal photon shot noise as its CCD counterpart. However, the summation of N signals after readout causes a summation of the readout noise as well, which yields the dependence $\sim N^{1/2}$.

Besides superior noise behavior, TDI CCDs offer a higher modulation transfer function and reduced optical crosstalk compared to digital TDI. Crosstalk denotes an undesired interaction in which the signal of a particular pixel induces a response in adjacent pixels. In general, optical crosstalk arises due to optical diffraction, refraction, and reflection within the device [25]. Especially for TDI mode, this can cause a major difference in the image quality between both technologies. To compare both sensors, we consider the total dynamic MTF of each system which is the product of all MTF contributions, such as the static MTF and a motion related MTF contribution [26]

$$\mathrm{MTF_{dyn}} = \mathrm{MTF_{static}} \cdot \mathrm{MTF_{motion}}. \tag{2.31}$$

Here, the static MTF is, in general, dependent on the aperture MTF

$$\mathrm{MTF_{static}} \sim \mathrm{MTF_{aperture}}, \tag{2.32}$$

which is a static contribution and includes the MTF resulting from the detector and the optical system according to

$$\mathrm{MTF_{aperture}}(f) = \mathrm{sinc}\left(\frac{\pi}{2}\frac{f}{f_\mathrm{N}}\frac{L}{L_\mathrm{px}}\right), \tag{2.33}$$

with the Nyquist frequency $f_\mathrm{N} = 1/2L_\mathrm{px}$. Considering a sampling aperture which corresponds to the pixel pitch $L = L_\mathrm{px}$ we obtain

$$\mathrm{MTF_{aperture}}(f_\mathrm{N}) = \mathrm{sinc}\left(\frac{\pi}{2}\right) = 0.64 \quad \text{for} \quad f = f_\mathrm{N}, \tag{2.34}$$

resulting in a rectangular pixel aperture, respectively for both sensor types.

The discrete MTF is given by the effective sampling aperture, defined by the number of subpixels and the deployed clock pattern, i.e., the discrete charge motion in TDI direction. This type of MTF describes the dissonance in sampling relating to the linear movement of an object and the discrete transfer of the charge carriers between adjacent potential wells. As a consequence, the charge transfer is asynchronous with the movement of the optical image [27].
In Table 2.2, different clock pattern and their corresponding effective pixel apertures are listed.

Table 2.2: Clock pattern and their corresponding pixel apertures (after [23]).

Clock pattern	Effective aperture L
Single-phase	L_{px}
Two-phase	$L_{\mathrm{px}}/2$
Three-phase, nonoverlapping	$L_{\mathrm{px}}/3$
Three-phase, overlapping	$L_{\mathrm{px}}/6$
Four-phase, nonoverlapping	$L_{\mathrm{px}}/4$
Four-phase, overlapping	$L_{\mathrm{px}}/8$

This table enables the calculation and comparison of the discrete MTF according to

$$\mathrm{MTF}_{\mathrm{discrete}}(f) = \mathrm{sinc}\left(\frac{\pi}{2}\frac{f}{f_{\mathrm{N}}}\frac{L}{L_{\mathrm{px}}}\right) \tag{2.35}$$

for the different clock pattern. In Figure 2.15 the corresponding curves are shown.

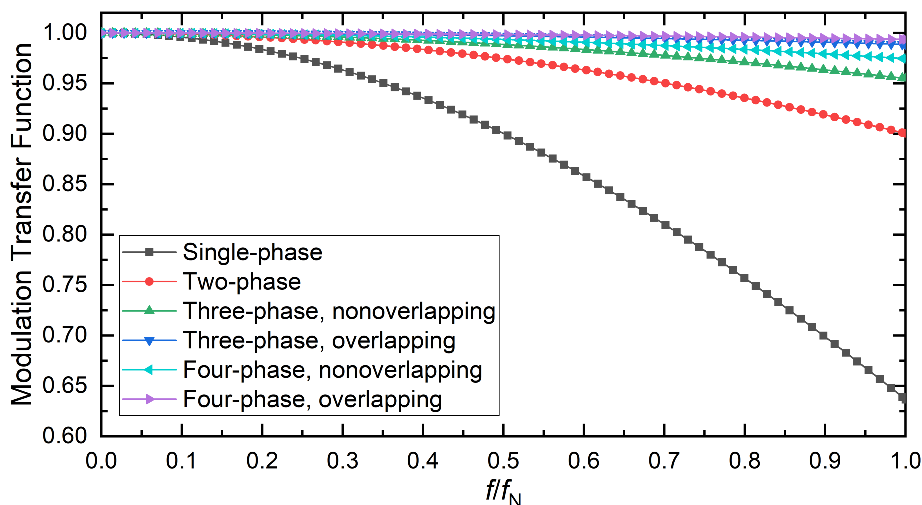

Figure 2.15: Discrete MTF for various pixel apertures.

As the graphs suggest, a smaller effective aperture L causes a higher discrete MTF, which is due to a smoother transfer of charge carriers in relation to the moving object. Therefore, a 4-phase CCD with an overlapping clock yields

$$\mathrm{MTF}_{\mathrm{discrete}} = \mathrm{sinc}\left(\frac{\pi}{2 \cdot 4}\right) = 0.994 \quad \text{for} \quad f = f_{\mathrm{N}}, \tag{2.36}$$

which is the highest value of all listed clock patterns. Moreover, since charge transfer is not possible in CMOS image sensors, this results in a single-phase addition step of adjacent TDI stages equal to a single-phase clock pattern. We obtain

$$\mathrm{MTF}_{\mathrm{discrete}} = \operatorname{sinc}\left(\frac{\pi}{2}\right) = 0.64, \tag{2.37}$$

which is a significant degradation compared to the MTF above.

Another contribution to the overall MTF is the motion related velocity MTF. Here, a mismatch in the relative velocity of the object and charge after N_{TDI} stages causes an increment in the sampling aperture. This can be expressed as

$$\mathrm{MTF}_{\mathrm{velocity}}(f) = \operatorname{sinc}\left(\frac{\pi}{2}\frac{f}{f_{\mathrm{N}}}N_{\mathrm{TDI}}\frac{\Delta v}{v}\right), \tag{2.38}$$

where v is the velocity of the moving object and Δv is the difference in velocity between charge and object motion. Consequently, this yields the dynamic MTF [28]

$$\mathrm{MTF}_{\mathrm{dyn}} = \mathrm{MTF}_{\mathrm{static}} \cdot \operatorname{sinc}\left(\frac{\pi}{2}\frac{f}{f_{\mathrm{N}}}N_{\mathrm{TDI}}\frac{\Delta v}{v}\right) \cdot \operatorname{sinc}\left(\frac{\pi}{2}\frac{f}{f_{\mathrm{N}}}\frac{L}{L_{\mathrm{px}}}\right). \tag{2.39}$$

Finally the total dynamic MTF, can be calculated which yields $\mathrm{MTF}_{\mathrm{dyn,CCD}} \approx 0.62$ for CCDs and $\mathrm{MTF}_{\mathrm{dyn,CMOS}} \approx 0.40$ for CMOS image sensors.
In this calculation the velocity MTF has been assumed to be $\mathrm{MTF}_{\mathrm{velocity}} = 1$ to illustrate the difference between both sensor types in terms of the deployed clock pattern and aperture. In conclusion, a reduced effective pixel aperture results in a higher dynamic MTF, which generally corresponds to lower optical crosstalk, i.e., reduced motion blur [26]. Especially TDI-CCDs provide improved noise and optical crosstalk characteristics compared to digital TDI sensors making CCDs more convenient for low-light applications and the detector of choice for TDI mode.

Chapter 3

Experimental Setup

The following pages describe the measurement setup and the experimental realization. Starting with an introducing overview, the subsequent sections will discuss the structure and functioning of the particular components, especially the TDI CCD and the evaluation board, in detail. Here, the circuits realized on the CCD will be shown and explained. Finally, this chapter ends with a presentation of the implemented timings.

3.1 Optoelectronic Measurement Setup

The measurements in this thesis were performed on an optoelectronic setup, which is sketched in Figure 3.1. As can be seen, the setup consists of a lightproof dark box in which a light emitting diode (LED) illumination module and the evaluation board, including a TDI CCD sensor, are placed. The illumination module is exchangeable, which enables it to cover a wavelength spectrum ranging from ultraviolet to infrared. The illumination source can be operated in constant or pulsed mode and illuminates an area of a circle with a diameter of 80 mm homogeneously. Here the maximum adjustable irradiance can reach up to $E = 500\ \mu\mathrm{W/cm}^2$. To ensure a constant distance between module and target, the illumination source is mounted atop a 3-dimensional axis of displacement. As voltage source for the illumination module and the evaluation board are 16x power supplies of type TTI QL355TP available, which can provide 15V/5A, 35V/3A, or 35V/0.5A. The control of the LED module occurs externally by a LabView program which allows conducting all mentioned adjustments. For the description of the design of the

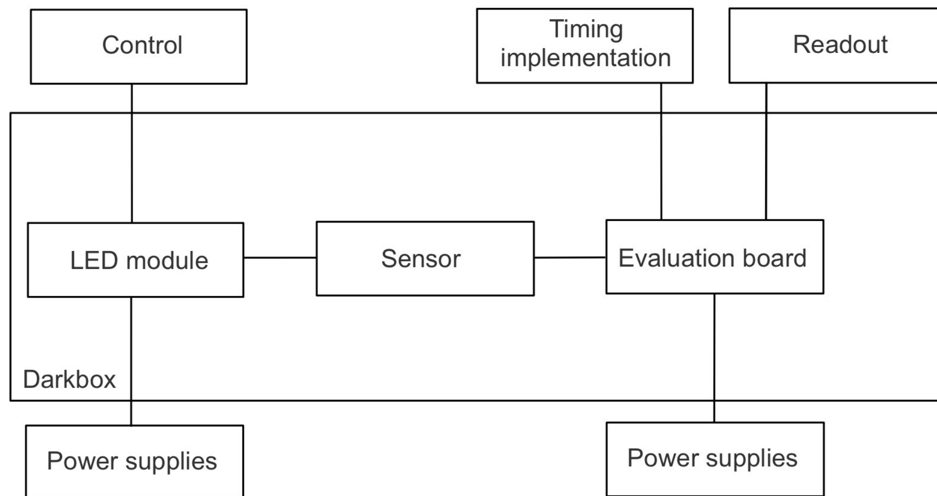

Figure 3.1: Block diagram of the measurement setup.

TDI-CCD and the clocking pattern, see the subsequent sections.

3.2 Design of the CMOS-TDI chip

The employed TDI sensor consists of a pixel matrix that contains 320 columns, each with a TDI depth of 128 stages [29]. The processing of the signal takes place by a correlated double sampling (CDS) stage as well as a sample-and-hold (S&H) circuitry, a comparator, and a digital circuit including a multiplexer. An illustration of the chip structure is shown in Figure 3.2.

The number of TDI stages can vary in steps 1, 32, 64, and 128. For this, the connection of the gate electrodes with an externally provided voltage supply can be divided into 4-pixel blocks. These four blocks have a pixel quantity of 1, 31, 32, and 64 pixels. For example, if a TDI depth of 64 is required, the first three blocks need to be activated, while the fourth block remains switched off, i.e. the unused TDI pixels are inactive. In total, the first three blocks yield than a TDI number of $1 + 31 + 32 = 64$ stages. Furthermore, the blocks can be addressed separately and simultaneously so that shifting of charges in both directions is possible.

To enable a bidirectional operation of the CCD, the pixel columns are mirror-

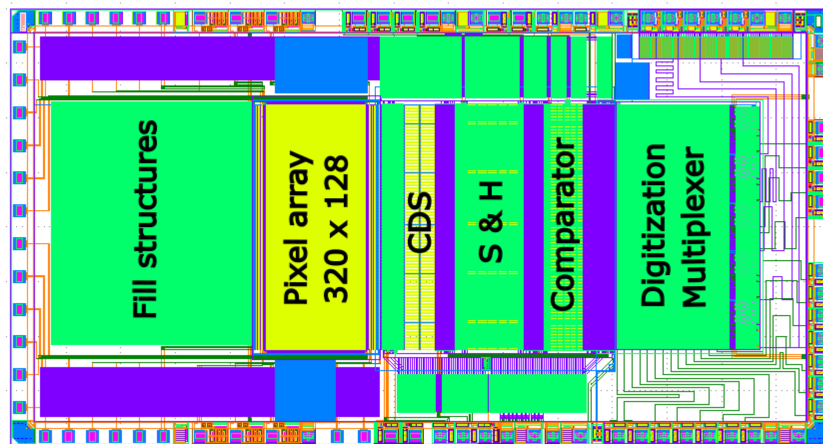

Figure 3.2: Top view of the sections of the employed TDI-CCD.

symmetric, and a readout structure is available on both sides. The readout is composed of a summing well (SW), a transfer gate (TG), a floating diffusion (FD), and a source follower (SF) circuitry. A chip photograph can be seen in Figure 3.3.

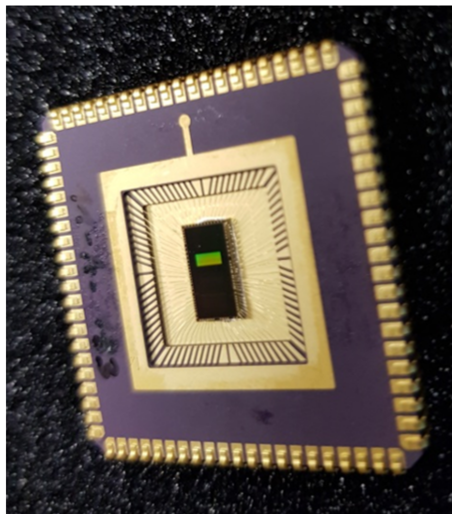

Figure 3.3: T89022A chip photograph [29].

The charge transfer in the TDI readout direction occurs by shifting the signal charge pixel-wise until the summing well is reached. The signal charge corresponding to a pixel is then collected in the summing well until it is transferred via the transfer gate, which acts as a barrier, when operated in blocking mode,

into the floating diffusion. Therefore, the floating diffusion of each TDI column is connected with a source follower circuitry at both ends. This double source follower circuitry consists of different MOSFETs which serve other purposes. The circuit diagram is shown in Figure 3.4.

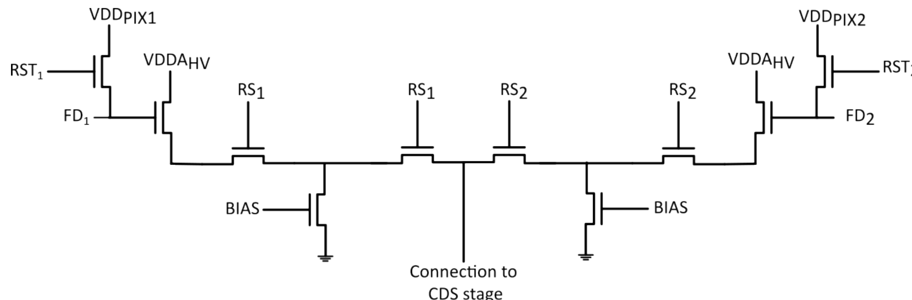

Figure 3.4: Design of the double source follower circuitry. Source followers at both sides of a TDI column are connected before the CDS stage.

The reset transistor removes the charge in the floating diffusion by applying a high voltage on the gate terminal RST while the voltage on the drain VDD_{PIX} is continuously constant. The depicted row select (RS) transistors act as a gate and passes the signal between FD and the CDS stage when activated. To convert the charge in the FD to a voltage, the signal voltage across the FD is measured. Here, a higher number of charge carriers results in a lower voltage at the FD and, consequently, the source follower output.

The signal is then processed by the CDS stage and afterwards stored in a S&H circuitry. Here, the sample-and-hold ensures effective use of the whole line period for conversion. For this, the S&H circuitry provides a stable input voltage to the comparator, while simultaneously, the other part of the S&H circuitry receives the next output voltage by the CDS. Finally, the digitization takes place by a comparator and an externally provided gray code. The multiplexer then latches the signal and shifts it towards the outputs.

3.3 Clock-Pattern

The pixel structure consists of four gates which are connected to four clock-pulse generators ϕ_1, ϕ_2, ϕ_3 and ϕ_4, respectively [19]. Here, the applied voltage

ranges from −4.5 V to 6.5 V. Since the device is of p-type, this means that at the low voltage, the gate is operated in blocking mode, whereas, at the high voltage, the CCD accumulates photo-generated charge carriers. The four-phase non-overlapping clock pattern employed in the measurements is depicted in Figure 3.5, where the period length is 466 clock cycles with a maximum line rate of 36 kHz, i.e., a minimal line period of 27.78 µs. As can be seen, the four different

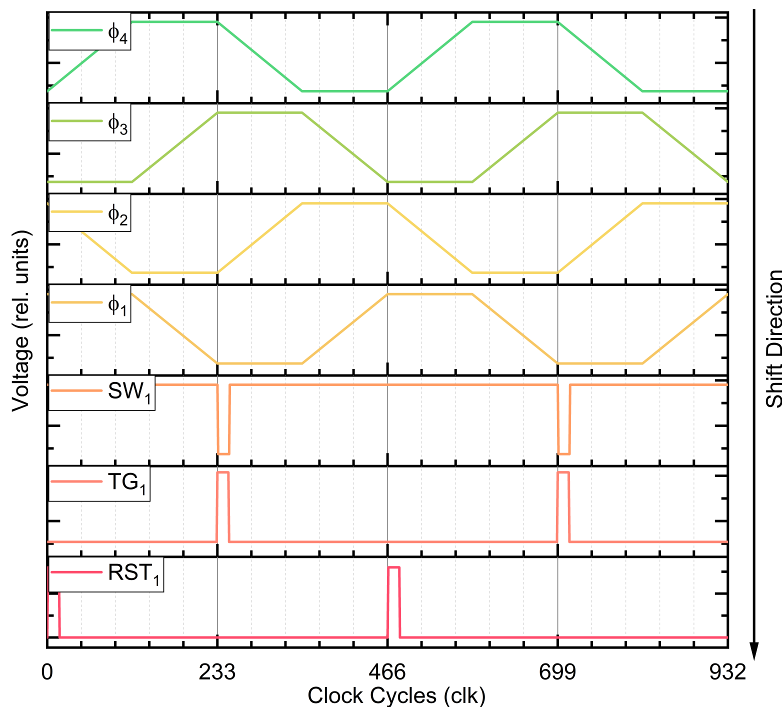

Figure 3.5: Four-phase, non-overlapping clock pattern with a line period of 466 clock cycles.

conditions of the ϕ signals, meaning high, low, increasing, and decreasing, are shaped with an equal clock length. Moreover, comparing the ϕ-signals with regard to each other, it is also obvious that the signals are shifted by $\pi/2$.

The readout is initiated by the signals SW_1 and TG_1 and starts at the beginning of the low phase of ϕ_1. At first, the summing-well gate is operated at high voltage while the signal charge carriers are shifted by ϕ_1 into the summing well. As ϕ_1 reaches the low voltage state, the summing well becomes low while the transfer gate TG_1 becomes high. Consequently, the charge stored in the summing well will

be shifted into the floating diffusion. Afterwards, when the transfer gate is at low again, a reset pulse RST_1, placed at the beginning of each line period, removes all charge carriers in the floating diffusion, and the whole procedure repeats. The used signal levels are listed in Table 3.1.

Table 3.1: Signal levels for the pixel array.

Signal	Low Voltage (V)	High Voltage (V)
ϕ	-4.5	6.5
SW_1	-4.5	6.5
TG_1	-4.5	-2.5
RST_1	0	16

Chapter 4

Anti-Blooming Mechanism

Various effects can degrade the image quality of a charge-coupled device. One is the blooming effect, which causes an overflow of charge carriers from one pixel to multiple surrounding pixels. This can be a problem, especially for TDI-CCDs where the charge is continuously accumulated, i.e., the effective exposure time is increased due to the multiple TDI stages.
The starting point for the discussion will be the cause and prevention of blooming in TDI-CCDs. The following pages will then introduce experimental techniques for characterizing time-delay integration CCDs. Further, the influence on specific device parameters used for sensor characterization will be investigated and discussed.

4.1 Charge Blooming Effect

In photo-electronic devices, the pixels have a particular saturation level, which defines the number of charge carriers a pixel can store and transfer without reporting a drop in performance. If this specific level is exceeded, the charge carriers start to overflow into adjacent pixels, i.e., contribute to other signal packets. This process is called charge blooming. The occurrence of blooming causes the image to be locally overexposed, which appears as a bright white spot spanning over a large area affecting multiple pixels.

The reason for blooming in an image sensor is, in general, overexposure of the pixels. However, in the case of TDI-CCDs, this overexposure can be of different origin. Therefore, to understand the cause of this effect and apply measures, this

effect needs to be discussed in detail in the particular case of TDI-CCDs.

4.1.1 Blooming in the case of TDI-CCDs

There are two different reasons for Blooming in TDI-CCDs: The overexposure of the active TDI stages (a) and the saturation of the inactive TDI region (b). Here, the cause of the first case does not differ significantly from blooming in common CCDs. However, the second case has a special origin which occurs only in TDI-CCDs. Both cases are explained in the following:

(a) The overexposure of active TDI stages is mainly due to an unmatched effective exposure time, which depends on the number of chosen TDI stages. The adjustment of the active TDI stages concerning the scene's brightness affects the total quantity of generated signal charges. For this, a bright scene usually uses a lower number of TDI stages, whereas a higher number of TDI stages is required for a darker scene. Otherwise, if too many stages are deployed for a bright scene, blooming will result, causing significant degradation of the image quality. This effect was shown for TDI CCDs by Materne et al. [30], where specular reflections over horizontal surfaces were the cause of blooming along the shifting register.

(b) TDI-CCDs offer the capability to select between a particular number of active TDI stages. Consequently, the other stages are not used or required for read-out. Nevertheless, the exposure of the sensor causes a generation of charge carriers anyhow in the silicon under the deactivated stages. If these charge carriers are not removed, the accumulation in the silicon will exceed the saturation level and cause blooming into the active TDI region. In conclusion, these photo-generated charge carriers must be removed to prevent blooming [31].

There are various options for preventing blooming in a TDI column. One method for blooming prevention takes place by dumping the excess charge into a vertical [32], or lateral [30][33] anti-blooming drain. Another method concerns shifting the charge in the opposite direction into a sink [34] and removing it by a periodical applied reset. This has the advantage, opposite to the other methods, that the charge storage capacity of the pixel is not reduced by integrating a physical anti-blooming structure. The following section will discuss an improved

version of the latter method.

4.1.2 Anti-Blooming Mechanism for TDI-CCDs

The anti-blooming mechanism used in this thesis is based on the concept of shifting charge packets located in unused TDI stages in opposite directions and removing them afterwards.
A similar mechanism was proposed by Farrier et al. [34] where a so-called exposure control was introduced, which deploys a particular number of TDI stages for readout. This exposure control is a switch selecting an ordinary ϕ-voltage clock or a ground state. The grounding of one gate causes a separation of the pixel column so that only a reduced number of pixels is read out since the grounded gate acts as a blockade preventing the charge from being transferred in the readout direction. Hence, by implementing these exposure control switches in particular positions, the number of TDI stages can be varied depending on which gate is grounded. However, the charge in the undesired TDI stages is still clocked in the readout direction since all four gates of each pixel are connected to the same respective four-phase clocks. Therefore, to prevent an overflowing of accumulated charges in the undesired region, the charge carriers are transferred by diffusion in the opposite direction into an exposure control sink, where they are removed.

Nevertheless, the anti-blooming mechanism presented by Farrier et al. has significant disadvantages that influence the TDI CCD's operation. The main disadvantage is the lacking capability of controlled removal of the excess charge carriers. Since these charges are transferred in the readout direction, the spilling charge carriers are assumed to be transferred in the opposite direction due to diffusion. However, at high illumination levels, the amount of generated charge carriers in the undesired stages will reach a level that can not be removed in an appropriate amount of time. At this point, there is the possibility that the excess charges overcome the barrier, causing blooming into the desired TDI stages.

Therefore, an alternative anti-blooming mechanism is presented, which allows the clocking of unused stages in the opposite direction. For this, the gates are connected in such a way that each pixel column has the capability to shift charge packets in both directions. This bidirectional shift mechanism requires a specific

separation of the pixel matrix and control of the transfer gates as already thematized in Section 3.2. Figure 4.1 shows a cross-section of a TDI-CCD operation in both directions simultaneously. The shifting occurs by periodic variations of the

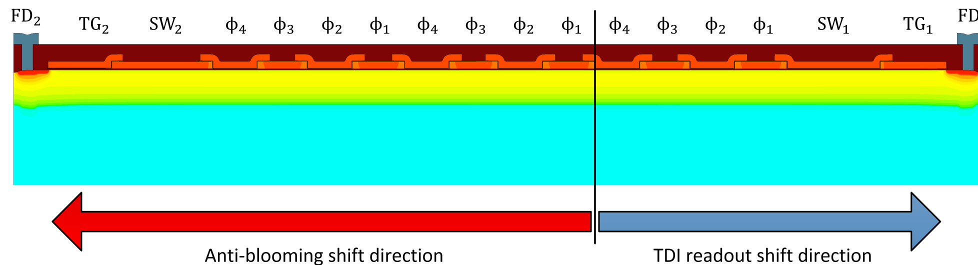

Figure 4.1: Cross-section of the TDI-CCD divided into an anti-blooming shift region and a TDI shift region [35].

applied voltage on the gate caused by an external clock. The bidirectional timing schemes used for a 4-phase CCD are depicted in Figure 4.2. Here, the shift direction for readout mode is $\phi_4 \rightarrow \phi_3 \rightarrow \phi_2 \rightarrow \phi_1 \rightarrow \mathrm{SW}_1 \rightarrow \mathrm{TG}_1 \rightarrow \mathrm{FD}_1$. In contrast the anti-blooming timing is $\phi_1 \rightarrow \phi_2 \rightarrow \phi_3 \rightarrow \phi_4 \rightarrow \mathrm{SW}_2 \rightarrow \mathrm{TG}_2 \rightarrow \mathrm{FD}_2$. Comparing both timing schemes, it is apparent that they shift in opposite directions. In this case, the signal is only read out at the FD_1 while at FD_2 the charge will be removed by RST_2 and VDDPIX_2. Consequently, the row select RS_2 is operated in continuous blocking mode while RS_1 passes the signal to the floating diffusion FD_1 and the CDS stage [35].

4.2 Experimental Results

4.2.1 Linear Camera Model

The exposure of an image sensor causes a generation of free charge carriers due to the photoelectric effect when the energy of the incident photons is greater than the band gap of the substrate material:

$$E_\lambda = \frac{\mathrm{hc}}{\lambda} > E_\mathrm{g} \tag{4.1}$$

where h denotes Planck's constant, λ is the wavelength, and c is the speed of light. If this requirement is fulfilled, electrons are excited from the valence band to the conduction band. The ratio of the total number of photons N_p that hit a pixel

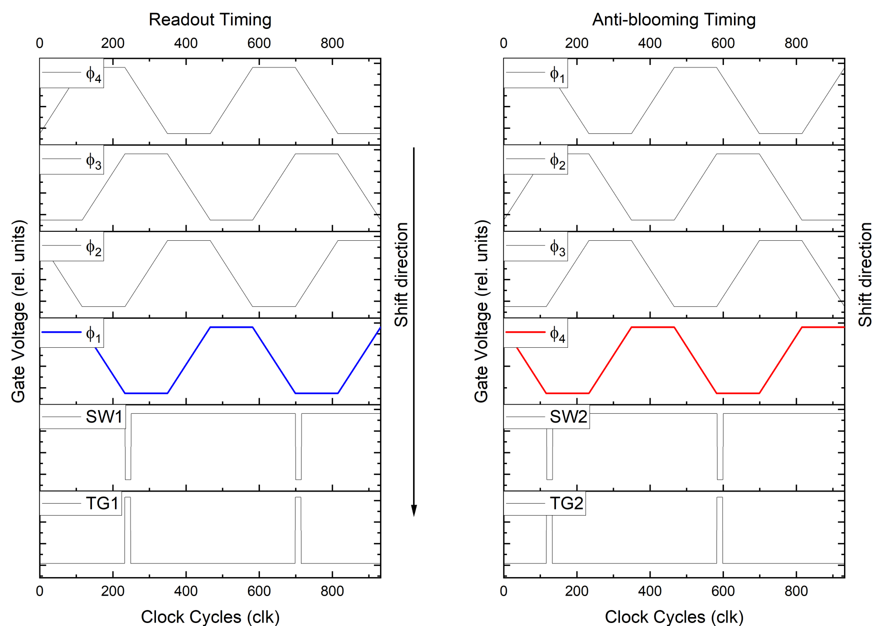

Figure 4.2: Timing scheme for TDI readout (left) and for anti-blooming mode (right) [35].

area A_{px} during the exposure time t_{exp} and the number of generated electrons N_{e} due to the photoelectric effect is defined as quantum efficiency [36]

$$\eta(\lambda) = \frac{N_{\mathrm{e}}}{N_{\mathrm{p}}}. \tag{4.2}$$

Here, the total number of photons after N_{TDI} TDI stages can be calculated according to

$$N_{\mathrm{p}} = \frac{A_{\mathrm{px}} E_{\mathrm{e}} t_{\mathrm{exp}} \lambda N_{\mathrm{TDI}}}{\mathrm{hc}}. \tag{4.3}$$

The characterization of a TDI sensor is based on the EMVA Standard 1288, which assumes a linear camera model. A sensor is called linear if the digital values at the output are proportional to the incident photons [37]. The mathematical model describing the steps from photons to digital numbers (DN) is sketched in Figure 4.3.

At first, a number of photons generate, with probability η, a particular number of electrons N_{e}. To this, a constant dark noise contribution μ_{d} is added. This signal is then converted to a voltage, amplificated, and digitized to digital gray

values μ_y. Here, the conversion of electrons can be modeled by the linear scaling factor K, which denotes the conversion or system gain. Equivalently, these steps concern the variance σ_y^2 and their corresponding contributions [38]. The remarkable of this mathematical model is that the camera is assumed to be a black box, i.e., the sensor parameters η, σ_d^2, and K are undetermined. Hence, only the input (=number of photons) and the output (=digital gray values) are known. However, these two pieces of information are sufficient to characterize the sensor and determine all needed quantities. This will be carried out in the following sections while examining blooming in TDI CCDs and its influence on the sensor characteristics.

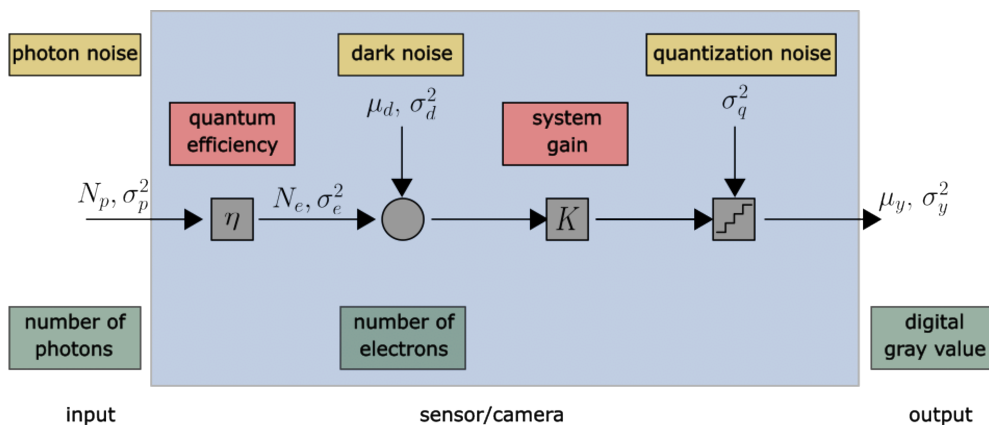

Figure 4.3: Mathematical model of a simple pixel. μ and σ^2 represent the mean and variance of a quantity, respectively (after [39]).

Nevertheless, to employ the characterization according to the EMVA Standard 1288, the following conditions need to be fulfilled [39]:

(1) The photon number depends linearly on the irradiance E_e and the exposure time t_exp. In the case of TDI sensors, the photon number also scales linearly on the number of TDI stages N_TDI.

(2) The mean gray values μ_y scale linearly with the number of incident photons N_p.

(3) The noise sources are stationary and white as well as invariant with respect to time and space.

(4) The quantum efficiency is the only quantity that is depending on the wavelength.

(5) The dark offset depends on the temperature.

These assumptions are valid for TDI sensors since the number of TDI stages N_{TDI} only increases the effective exposure time, i.e., the number of photons linearly. Hence, a TDI sensor can be considered a linear camera.

4.2.2 Responsivity

The gain which measures this input-output relation is called responsivity. However, this linearity is only valid if the amount of generated signal charges does not exceed the saturation level of the pixels.
Since the signal charge units are converted to digital gray values μ_y given in digital numbers DN, the linearity can be verified by plotting μ_y versus N_{p}. By definition, the slope yields the responsivity

$$R = \frac{\mu_y - \mu_{y.\mathrm{dark}}}{N_{\mathrm{p}}} \tag{4.4}$$

where the dark offset $\mu_{y.\mathrm{dark}}$ results from measurements in the absence of any light source. Furthermore, the mean gray values scale linearly with the photon number due to the listed points (1) and (2). Thus, the responsivity should yield a constant value independently of the TDI stage number. However, as suggested by Ercan et al. [31], photo-generated carriers in the unused stage can cause blooming.
Accordingly, the first measurements took place without an anti-blooming scheme to demonstrate the occurrence of blooming caused by the unused stages. For this, the timing scheme presented in Section 4.1.2 was applied, while at first, the anti-blooming clocking was inactive, i.e., the applied gate voltage on the unused stages was set to low. In the following, the mean gray values and the photon numbers are normalized by dividing by N_{TDI} to better compare the corresponding responsivity curves among themselves.
Figure 4.4 shows the resulting responsivity curves for 128, 64, and 32 TDI stages, while the former corresponds to the TDI depth of the whole pixel column, i.e., the 128 TDI curve states the actual responsivity. As can be observed, the responsivities (= the slope of these curves) differ in value. Furthermore, the measurements

for smaller numbers of TDI stages yield higher mean gray values than the measurement with more TDI stages which is contradictory to the linear dependence demanded in point (1).

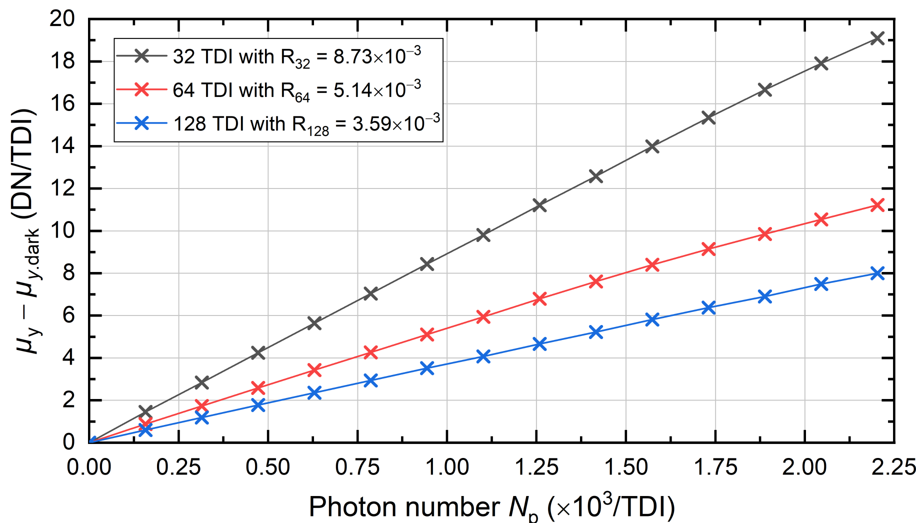

Figure 4.4: Responsivity curves measured without integration of the anti-blooming clocking for different numbers of TDI stages.

According to these results, it can be supposed that these measurements contain a light-dependent offset which is stronger the more stages are unused. The prove this conjecture, the offset was measured while all TDI stages were adjusted inactive and the summing well, the transfer gate, and the readout circuitry operated as described in the previous section. The plot can be viewed in Figure 4.5, which shows an increment of gray values in dependence on the photon number. This effect can be explained as follows:

Since the whole pixel area is inactive, the exposure causes the generation of charge carriers in the silicon. Yet, the charges are not removed, causing them to accumulate until they reach the saturation level. However, this saturation level cannot be exceeded, forcing newly generated electrons to spill across the pixel column and reach the floating diffusion where they are read out. Here, the spilled charge depends on the irradiance, specifically on the photon number. In addition, the amount of spilled charge also depends on the number of deactivated stages.

To cancel this blooming effect out and verify the proper functionality of the

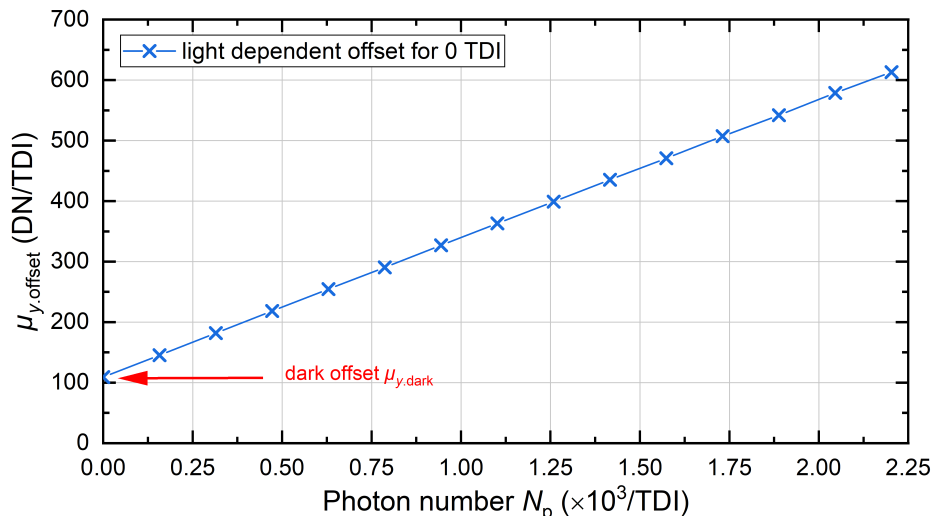

Figure 4.5: Signal offset $\mu_{y.\text{offset}}$ versus photon number. For $N_\text{p} = 0$ the signal offset is equal to the dark offset $\mu_{y.\text{dark}}$.

presented anti-blooming mechanism, the responsivity measurements will be repeated, considering that the charge in the not used TDI stages is shifted in the opposite direction and removed. As the plots in Figure 4.6 confirm, the anti-blooming mechanism impacts the measurements and results in equal responsivity curves. Consequently, there is no blooming present. Moreover, it can also be concluded that measurements of the responsivity for varying numbers of TDI stages are necessary to check the correct functioning of the implemented timing, anti-blooming scheme, and operation of the TDI CCD in general.

4.2.3 Photon Transfer Curve

In the previous section, the responsivity was introduced, where gray values in digital numbers were determined in dependence on the photon number. Nonetheless, from a physical aspect, these digital numbers are meaningless. Therefore, it is all the more important to define a quantity that describes the conversion of electrons to digital numbers. The best known and most common approach is the photon transfer method [40], which exploits the Poissonian statistics of photon arrival. For this, the measured photo-induced variance σ_y^2 is depicted versus the mean gray values μ_y. The slope of this curve yields the conversion factor, which is denoted as conversion gain K in DN/e$^-$.

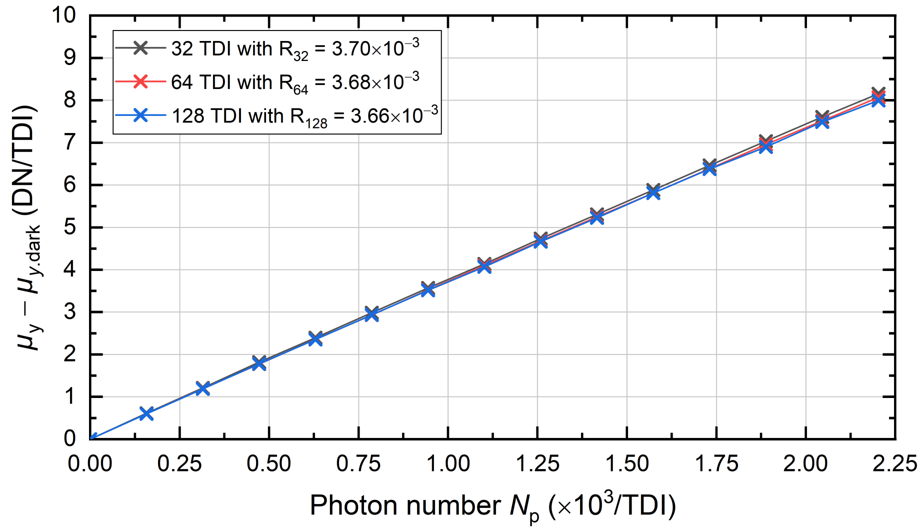

Figure 4.6: Responsivity curves measured with integration of the anti-blooming clocking for different numbers of TDI stages.

The exposure of the sensor induces a signal variance consisting of different noise sources. These can be variations in the value of a pixel that is observed over time (temporal noise), or due to spatial variations of the pixels (spatial noise) [38]. Moreover, the noise sources can be dependent or independent of the signal. Here the independent noise, relevant for the photon transfer evaluation, can be summarized as dark noise $\sigma^2_{y.\mathrm{dark}}$. This consists of the quantization noise $\sigma^2_{\mathrm{q}} = 1/12\ \mathrm{DN}^2$ as well as the sensor readout and the amplifier circuit-related distributed noise σ^2_{d}. Hence, the dark offset is given by as $\sigma^2_{y.\mathrm{dark}} = K^2\sigma^2_{\mathrm{d}} + \sigma^2_{\mathrm{q}}$. On the contrary, the shot noise σ^2_{e} is signal-dependent and scales linearly to the number of electrons according to $\sigma^2_{\mathrm{e}} = N_{\mathrm{e}}$. Since the noise contributions sum up the total variance can be written as

$$\sigma^2_y = K^2(\sigma^2_{\mathrm{d}} + \sigma^2_{\mathrm{e}}) + \sigma^2_{\mathrm{q}}. \tag{4.5}$$

Finally, if the relation $\mu_y - \mu_{y\mathrm{dark}} = KN_{\mathrm{e}}$ is used we obtain the equation [17]

$$\sigma^2_y - \sigma^2_{y.\mathrm{dark}} = K(\mu_y - \mu_{y.\mathrm{dark}}). \tag{4.6}$$

Figure 4.7 shows an ideal illustration where the four characteristic noise regimes of a Photon-Transfer Curve (PTC) are depicted. At first, the read noise is the

dominating noise source under dark conditions. As the signal, respectively, the number of photons increases, the shot noise exceeds the read noise. However, because the Fixed-Pattern Noise (FPN) scales linearly with the signal, the Photo-Response Non-Uniformity (PRNU) becomes dominating afterwards. Finally, the noise decreases drastically as the full-well capacity is reached in the corresponding pixels. Thus, the conversion gain K can be determined by depicting the variance versus the mean gray values and calculating the slope of the shot-noise-related part of this curve.

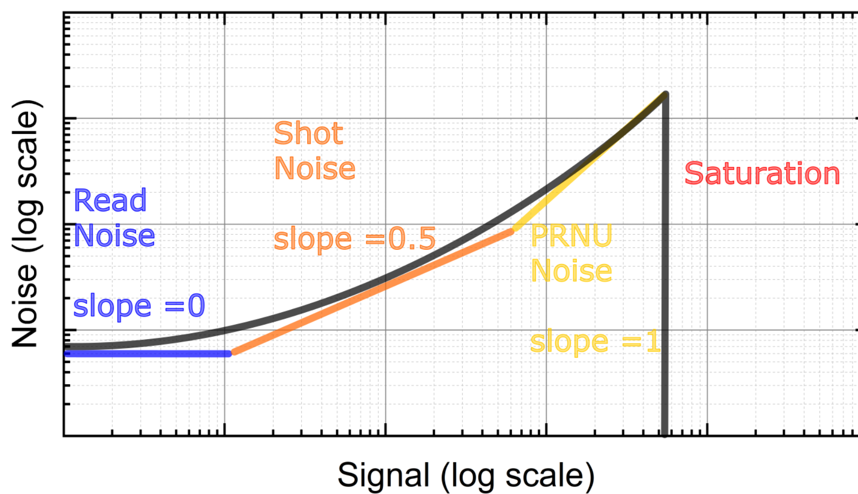

Figure 4.7: Ideal PTC illustration showing the four classical noise regimes.

The calculation of the conversion gain takes place in the following, where measurements for a TDI depth of 64 stages and a line frequency of 16.7 kHz are carried out with and without an anti-blooming mechanism. The corresponding photon transfer curves evaluated for 40-pixel columns, respectively, are depicted in Figure 4.8. The first thing which can be observed is the kink at around 600 DN, which both diagrams show. This can be caused most probably by surface contact of the charge packets. Since this kink distorts the actual value of the camera gain, the evaluation takes place for the interval 100 DN – 500 DN which yields

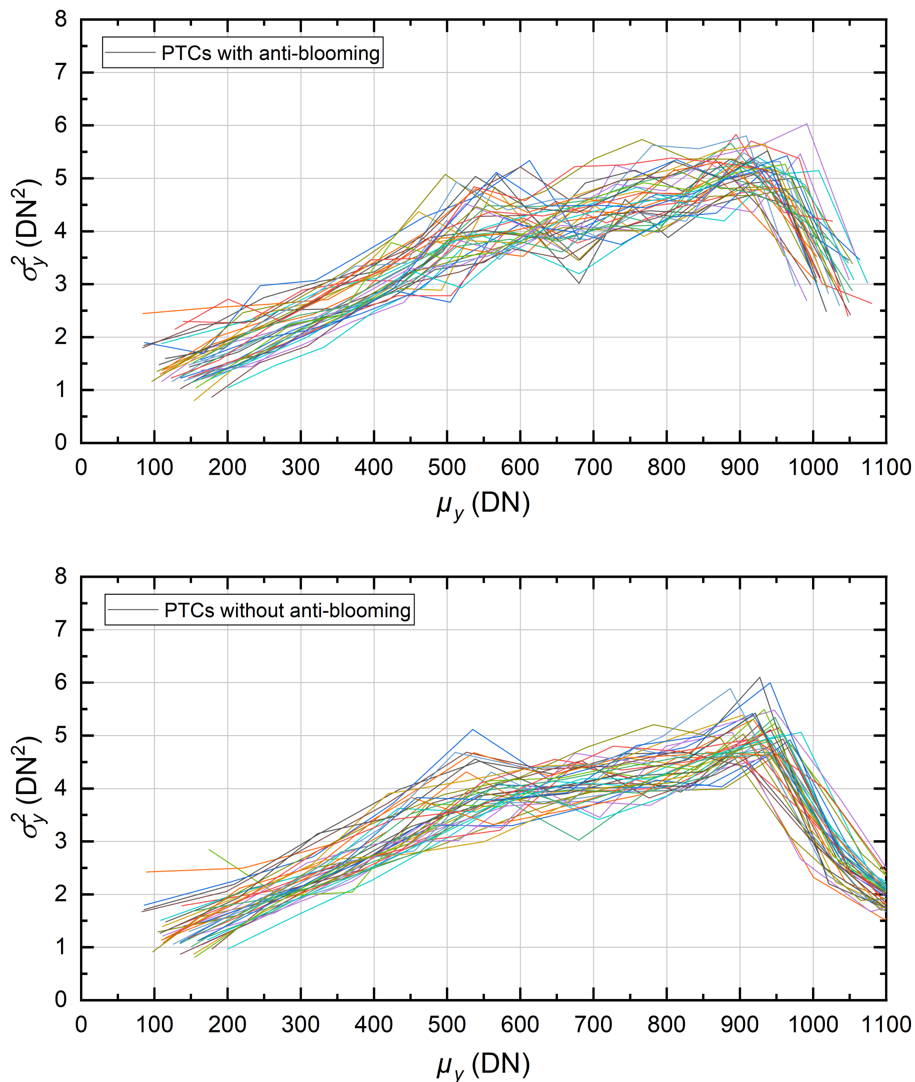

Figure 4.8: Photon transfer curves with (top) and without (bottom) implemented anti-blooming clocking for 64 TDI stages.

the camera gains arithmetically averaged by 40-pixel columns:

$$K_{\text{noAB}} = (6.30 \pm 1.14) \cdot 10^{-3}\ \text{DN/e}^- \tag{4.7}$$

$$K_{\text{AB}} = (6.14 \pm 1.26) \cdot 10^{-3}\ \text{DN/e}^- \tag{4.8}$$

where the indices denote the used mechanism. Not surprisingly, the determined camera gains show no difference in value since the variance only depends on the shot noise, respectively, the number of accumulated electrons N_{e}. Therefore, the increasing number of charge carriers in the used pixels due to blooming results in

a rising variance as well.
But most importantly is the fact that the camera gain (or PTC measurement) in itself is not a reliable quantity to verify the proper function of a TDI sensor since it does not reflect blooming effects.
For this reason, it can be concluded that in the case of TDI CCDs, first and foremost, the responsivity measurement for varying numbers of TDI stages should be carried out and compared to verify the proper functioning of the device and timing.

4.2.4 Signal-to-Noise Ratio

In general, applications with low-light-level detection capabilities require low noise and a high signal. Hence, especially for TDI CCDs, particular attention has to be paid to the signal-to-noise ratio (SNR), which can be expressed in dependence on the conversion gain and the responsivity according to [36]

$$\mathrm{SNR}(N_\mathrm{p}) = \frac{K\eta N_\mathrm{p}}{\sqrt{\sigma^2_{y.\mathrm{dark}} + K^2\eta N_\mathrm{p}}}, \tag{4.9}$$

with $\eta = R/K$. Both R and K have been determined in the previous sections, which allows us to compare the SNR for the measurements with and without anti-blooming clocking. Further, both results can be compared to an ideal SNR curve

$$\mathrm{SNR}_\mathrm{ideal}(N_\mathrm{p}) = \sqrt{N_\mathrm{p}}, \tag{4.10}$$

where the assumptions of a quantum efficiency $\eta = 1$ and no dark noise $\sigma_{y.\mathrm{dark}} = 0$ are made. The corresponding curves are depicted in Figure 4.9. It is apparent that the SNR curve without an anti-blooming mechanism is closer to the ideal SNR curve and yields a better SNR in comparison to the measurement with implemented anti-blooming. If we take a closer look at Eq.(4.9), these results are not surprising. As we can see, the SNR scales with the responsivity $\sim R^{1/2}$ if we deploy the equation for the quantum efficiency. Consequently, since the responsivity increases due to blooming, the SRN increases as well and distorts the actual value, which would be obtained if no blooming were present.

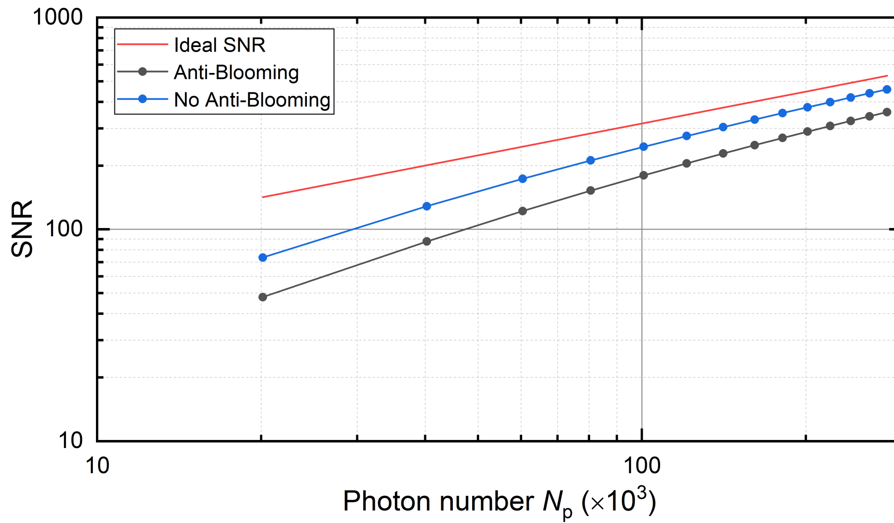

Figure 4.9: SNR of the sensor with and without anti-blooming clocking, and the SNR of an ideal sensor.

Further, the ratio between the largest and smallest value of the photon number can be determined. This ratio is defined as dynamic range

$$\mathrm{DR} = \frac{N_{\mathrm{p.sat}}}{N_{\mathrm{p.min}}}, \tag{4.11}$$

where $N_{\mathrm{p.sat}}$ is the photon number at the highest SNR, and $N_{\mathrm{p.min}}$ is obtained for SNR = 1. The calculation of the photon numbers can be carried out according to [39] with the approximation

$$N_{\mathrm{p}}(\mathrm{SNR}) \approx \begin{cases} \frac{\mathrm{SNR}^2}{\eta}\left(1 + \frac{\sigma_{\mathrm{d}}^2+\sigma_{\mathrm{q}}^2/K^2}{\mathrm{SNR}^2}\right) & \text{for SNR} \gg \sqrt{\sigma_{\mathrm{d}}^2 + \sigma_{\mathrm{q}}^2/K^2} \\ \frac{\mathrm{SNR}}{\eta}\left(\sqrt{\sigma_{\mathrm{d}}^2 + \sigma_{\mathrm{q}}^2/K^2} + \frac{\mathrm{SNR}}{2}\right) & \text{for SNR} \ll \sqrt{\sigma_{\mathrm{d}}^2 + \sigma_{\mathrm{q}}^2/K^2}. \end{cases} \tag{4.12}$$

Consequently, with Eq.(4.12) and Eg.(4.11) we obtain

$$\mathrm{DR}_{\mathrm{AB}} = 800 \qquad \text{and} \qquad \mathrm{DR}_{\mathrm{noAB}} = 1270. \tag{4.13}$$

The comparison and discussion of the results are provided in the following section.

4.3 Comparison and Interpretation

To provide a better comparison, the determined parameters are listed in Table 4.1 for both implementations measured for 64 TDI stages.

Table 4.1: Determined parameters for measurements with and without anti-blooming mechanism.

Parameter	Anti-blooming	No Anti-blooming
Responsivity	$3.68 \cdot 10^{-3}$ (DN)	$5.14 \cdot 10^{-3}$ (DN)
Conversion Gain	$6.14 \cdot 10^{-3}$ (DN/e$^-$)	$6.30 \cdot 10^{-3}$ (DN/e$^-$)
Quantum Efficiency	0.60	0.82
SNR	1 - 357	1 - 457
Dynamic Range	800	1270

Comparing the determined parameters, a significant difference in value for both mechanisms can be identified since the measurement without anti-blooming is affected by overflowing charge carriers generated in inactive TDI pixels. Considering the responsivity R, which is the input-output gain of a detector, the relation

$$\mu_y - \mu_{y.\mathrm{dark}} = R \cdot N_{\mathrm{p}} \tag{4.14}$$

can be used to calculate the ratio of both mechanisms and compare the input, i.e., the number of incident photons. Here, for 64 TDI stages, the ratio

$$\frac{(\mu_y - \mu_{y.\mathrm{dark}})_{\mathrm{noAB}}}{(\mu_y - \mu_{y.\mathrm{dark}})_{\mathrm{AB}}} = \frac{R_{\mathrm{noAB}}}{R_{\mathrm{AB}}} \cdot \frac{N_{\mathrm{p.noAB}}}{N_{\mathrm{p.AB}}} = 1.4. \tag{4.15}$$

is obtained. Since the responsivity R is a constant and characteristic quantity for a detector [39], independently of the number of used TDI stages and used mechanism, this result suggests that the number of incident photons differs between both mechanisms according to

$$N_{\mathrm{p.noAB}} = 1.4 \cdot N_{\mathrm{p.AB}}. \tag{4.16}$$

However, this is a contradiction because the quantities in Eq.(4.3) were equal for both measurements, i.e., the photon number has to be equal as well.
This can be explained by comparing the quantum efficiencies of both mechanisms for different numbers of TDI stages. Here, the quantum efficiency describes the probability that a photon of a particular wavelength generates an electron. Hence, the QE should yield the same result for all measurements. Calculating the quan-

tum efficiencies we obtain

$$\eta_{128.\mathrm{AB}} = \eta_{64.\mathrm{AB}} = \eta_{32.\mathrm{AB}} = 0.60 \tag{4.17}$$

for 128, 64, and 32 TDI stages with implemented anti-blooming clocking and contrary

$$\eta_{128.\mathrm{noAB}} = 0.60, \qquad \eta_{64.\mathrm{noAB}} = 0.8, \qquad \text{and} \qquad \eta_{32.\mathrm{noAB}} = 1.39. \tag{4.18}$$

for the measurements without anti-blooming clocking. According to the definition of the QE, the results without AB mechanisms are implausible since they indicate that a reduction of the TDI stage number increases the probability of generating more electrons, i.e., increasing the signal with the same number of incident photons per TDI stage. This contradiction results from an accumulation of charge carriers in inactive regions of the pixel array. Since these charge carriers are not removed, they saturate the inactive area and start, as a consequence, to overflow into the active region, where they contribute to the signal. Consequently, the signal constitutes charge carriers generated in the active pixel and additional charge carriers generated in the inactive area. This causes significant distortion of further responsivity-dependent quantities, such as the signal-to-noise ratio and the dynamic range.
Thus, an anti-blooming mechanism has to be implemented if measurements with a reduced number of TDI stages are performed to ensure that no undesired signals affect the measurement results.
Moreover, before characterizing TDI sensors, the linearity has to be confirmed by comparing responsivity measurements with differing numbers of TDI stages. Here, an equal responsivity would indicate that a proper operation of the TDI CCD without blooming can be assumed. Otherwise, the characterization would yield wrong results for the parameters, and the image quality would be degraded considerably.

4.4 Influence of Blooming on Modulation

The previous section has shown how the sensor characteristics can be distorted by blooming. To illustrate how blooming affects the image quality, we consider a periodic pattern with variations in intensity, resulting in periodic variations of

the mean gray values. The modulation (or contrast) of this pattern can then be expressed by [41][42]

$$M = \frac{f_{\text{max}} - f_{\text{min}}}{f_{\text{max}} + f_{\text{min}}}, \tag{4.19}$$

where f_{max} denotes the maximum and f_{min} is the minimum value of a specific quantity. Here, the modulation can assume values ranging from $0 \leqslant M \leqslant 1$, where $M = 1$ yields the highest and $M = 0$ no contrast, i.e., the pattern is indistinguishable. Considering the highest mean gray value μ_{max} at the highest intensity of this pattern, whereas the lowest intensity μ_{min} is equal to the dark offset $\mu_{\text{y.dark}}$, the modulation with the anti-blooming mechanism is given by

$$M_{\text{AB}} = \frac{\mu_{\text{max}} - \mu_{y.\text{dark}}}{\mu_{\text{max}} + \mu_{y.\text{dark}}}. \tag{4.20}$$

Equivalent, the modulation for the case without anti-blooming can be calculated. However, it must be considered that μ_{min} contains an offset dependent on μ_{max}, i.e. $\mu_{\text{min}} = \mu_{y.\text{dark}} + \mu_{y.\text{offset}}$. Hence, we obtain the equation

$$M_{\text{noAB}} = \frac{\mu_{\text{max}} - (\mu_{y.\text{dark}} + \mu_{y.\text{offset}})}{\mu_{\text{max}} + (\mu_{y.\text{dark}} + \mu_{y.\text{offset}})}. \tag{4.21}$$

In Figure 4.10, the modulation curves for both cases are depicted in dependence on the irradiance, i.e., the intensity maximum.

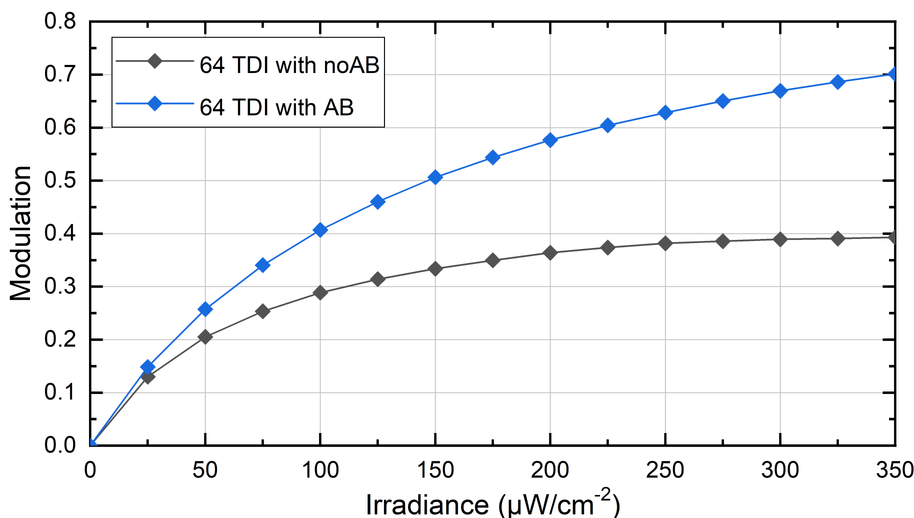

Figure 4.10: Modulation for the measurements with (blue) and without anti-blooming mode (red) for 64 TDI stages.

The comparison shows that $M_{\mathrm{AB}} > M_{\mathrm{noAB}}$. Consequently, a better contrast is obtained with an anti-blooming mechanism than without, i.e., due to blooming, the difference in luminance is more difficult to distinguish. Especially at higher irradiances, where blooming increases, the measurement becomes, at some point, useless. To illustrate the change, in contrast, we consider both modulations at 350 $\mu\mathrm{W/cm^2}$. Figure 4.11 shows three test pattern with modulations $M = 1.0$, $M = 0.7$, and $M = 0.4$. It can be seen how the black-white stripes become indistinct with decreasing contrast. Moreover, as already discussed in Section 2.3.3, the modulation transfer function is defined as the ratio of the image's modulation to the object's modulation. Hence, blooming will also result in a degradation of the MTF. The subsequent chapter will discuss how the degradation of the MTF affects the image quality.

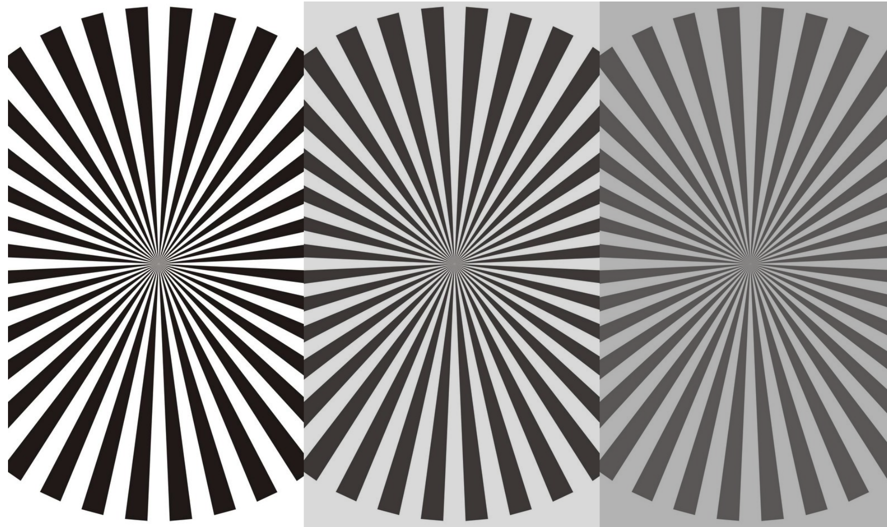

Figure 4.11: Test pattern for various modulations. Modulations from left to right: 100%, 70%, and 40%.

4.5 Summary

In the present chapter, an extensive examination of blooming in time-delay integration CCDs was given, while the focus laid on blooming caused due to an accumulation of charge carriers in unused TDI stages. A method to identify blooming of this origin was presented, and an anti-blooming mechanism has been implemented. Measurements with and without this anti-blooming mechanism have been conducted and compared, showing considerable differences in the determined sensor parameters. The differences caused due to blooming caused a contribution to the signal and resulted in responsivity curves that differed depending on the employed TDI stage number.

Since the quantum efficiency, the signal-to-noise ratio, and the dynamic range depend on the responsivity, they have been distorted as well, yielding wrong sensor characteristics.

Beyond that, blooming not only yields wrong sensor characteristics but also considerably degrades the image quality in terms of contrast since excess carriers are added to pixel signals yielding erroneous values. This has been shown by comparing the modulation curves of both implementations.

In conclusion, it has been shown that using the anti-blooming clocking implementation led to accurate and correct measurements of the sensor characteristics. Consequently, TDI CCDs need to contain an anti-blooming mechanism. Moreover, the linearity between different TDI stage modes can be used as a method to check the sensor's functionality and to support the correctness of the measurements and sensor characterization.

Chapter 5

Charge Transfer Model for TDI

To understand and exploit the properties of a continuously accumulating charge-coupled device operating in time-delay integration mode, the transfer of the charge packets across the pixel line was intensively studied.

Especially the degradation of the charge transfer efficiency per shift, which states the percentage of successfully transferred charge carriers between two adjacent potential wells, is crucial. Since the transfer is affected by the size of the accumulated signal charge within a potential well, a change in transfer conditions has an impact on the transfer time. Here, a difference in gate clocking time with respect to the transfer time of the charge packet would result in a possible loss of charge carriers. This is associated with the fall time of the applied clock since a falling edge faster than the charge transfer will result in a redistribution of left-over charges to adjacent potential wells [43].

Throughout this chapter, the corresponding transfer mechanisms will be explained, and an analytical model, considering these mechanisms, will be derived. Finally, an analytical investigation of the charge transfer efficiency (CTE) and MTF will be presented and discussed. The goal is to obtain a model that allows an estimation of the transfer characteristics for a TDI CCD dependent on the design parameters.

5.1 Transfer Mechanisms

The transfer of charge carriers in the silicon from one gate to another in a charge-coupled device takes place by shaping and reshaping the form of the potential wells through variations of the applied voltages. By operating two adjacent gates at surface depletion, the superposition of the potential wells will result in a redistribution of charge carriers underneath both gates. As soon as one of these gates starts to form a potential barrier, the difference in potential well depth will originate in a potential gradient causing the charge carriers to flow in the direction of the lowest potential. Since the spatial expansion of the potential wells is finite, the flow of charge carriers through an area A in a particular time t results in an electric current density j. In a semiconductor, this current density can be expressed as the sum of the drift current and the diffusion current

$$j_\mathrm{n}(x,t) = -\underbrace{\mathrm{q}\cdot\mu_\mathrm{n}\cdot n(x,t)\cdot E}_{\text{drift}} - \underbrace{\mathrm{q}\cdot D_\mathrm{n}\partial_x n(x,t)}_{\text{diffusion}}, \tag{5.1}$$

where μ_n denotes the electric charge mobility, $n(x,t)$ the charge carrier density and D_n the diffusion constant. Here, the charge movement due to electric fields corresponds to the drift current, while the diffusion current results from a variation in the charge carrier concentration.
In a charge-coupled device, the transfer of charge carriers is mainly driven by three transfer mechanisms that affect the electric current density simultaneously: These are the self-induced drift, the fringing-field drift, and the thermal diffusion.

The self-induced drift and the fringing-field drift contribute to the drift current since the charge propagation, affected by both transfer mechanisms, is the result of electric fields at the Si/SiO_2 interface. For both transfer mechanisms, the source and the impact on the charge transfer are different and depend, in general, on the size of the charge packet. Here, the **Self-induced drift** (SID) results from a repulsive force caused by charger carriers with the same polarity. This induced electric field equals a concentration gradient along the Si/SiO_2 interface, causing a redistribution of charge carriers until the repulsive force is neutralized, i.e., an equilibrium state is reached.
The self-induced current density can therefore be expressed as

$$j_\mathrm{sid} = -\mathrm{q}\cdot\mu_\mathrm{n}\cdot n(x,t)\cdot E_\mathrm{sid}, \tag{5.2}$$

where E_{sid} is the charge-dependent electric self-induced drift field. To formulate E_{sid} in dependence of the charge carrier density, the approach of a linear relation between $n(x,t)$ underneath the transfer gate and the surface potential ϕ_{s} is assumed [44]. The equation gives this linear relation

$$\phi_{\text{s}}(x,t) = \phi_{\text{s},0} - \frac{\text{q}}{C_{\text{eff}}} n(x,t), \tag{5.3}$$

where $\phi_{\text{s},0}$ denotes the surface potential in absence of any electric charge [45]. Determining the derivative of $\phi_{\text{s}}(x,t)$ with respect to the spatial variable x yields the electric field

$$E_{\text{sid}} = -\frac{\partial \phi_{\text{s}}}{\partial x} = \frac{\text{q}}{C_{\text{eff}}} \frac{\partial n(x,t)}{\partial x} \tag{5.4}$$

whose spatial gradient is $\partial n/\partial x < 0$, since the electric field is also $E_{\text{sid}} < 0$ regarding p-type charge-coupled device where the electrons are the minority charge carriers. Consequently, with Eq.(5.2) and Eq.(5.4) the electric current density can be written as

$$j_{\text{sid}}(x,t) = -\frac{\text{q}^2 \cdot \mu_{\text{n}} \cdot n(x,t)}{C_{\text{eff}}} \frac{\partial n(x,t)}{\partial x}. \tag{5.5}$$

resulting in a positive self-induced net current $j_{\text{sid}} > 0$.

In contrast, the **fringing-field (FF) drift** occurs due to varying externally applied potentials of two adjacent gate electrodes. The reason is a coupling of electrostatic potentials of the concerned gates, whose superposition results in a distortion of the potential curve, equivalent to a potential gradient. This is shown in Figure 5.1. Thus, the corresponding drift current contribution can be expressed as

$$j_{\text{ff}}(x,t) = -\text{q} \cdot \mu \cdot n(x,t) \cdot E_{\text{ff}} \tag{5.6}$$

where the fringing-field E_{ff} is mainly dependent on the difference in gate voltages, the gate geometry, and the substrate doping [46].
However, due to the uniformity of the fringing-field and its complex boundary conditions, an analytical expression is quite difficult. Hence, the minimal value of the fringing field located at the center of the transferring electrode [46] can be calculated by the empirical approximation [47]

$$E_{\text{ff,min}} = 6.5 \frac{d_{\text{ox}}}{L} \frac{V}{L} \left[\frac{5 d_{\text{si}}/L}{1 + 5 d_{\text{si}}/L} \right]^4, \tag{5.7}$$

where ΔV is the voltage difference applied on adjacent gates during charge transfer, L is the gate length, and d_{ox} and d_{si} denote the thickness of the oxide and silicon.

In comparison, the self-induced drift is a fast transfer mechanism that dominates the initial charge transfer for higher signal levels, while the fringing-field drift is a relatively slow process. However, as the charge carrier density decreases, the self-induced drift becomes less effective, and the remaining charge is mainly transferred by the fringing-field [19]. Hence, the fringing-field leads to a significant contribution to the transfer efficiency.

On the other hand, the fringing field depends, in general, strongly on the accumulated charge quantity and becomes weaker for higher charge densities. Moreover, under full well conditions, the fringing-field disappears since, in this case, the potential difference between two adjacent gates equals zero.

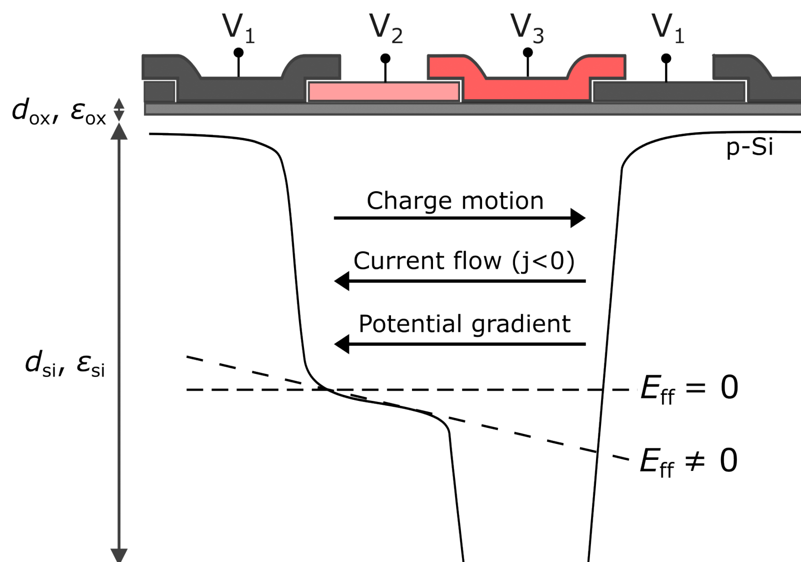

Figure 5.1: Cross-section of a p-type CCD with applied gate voltages $V_1 < V_2 < V_3$. The coupling of the electric fields results in a potential gradient E_{ff}. Dashed lines indicate the shape of the potential well in the absence and presence of the fringing-field. The direction of charge motion, current flow, and potential gradient are indicated by the arrows [48].

In the absence of any electric field, i.e., self-induced drift and the fringing field drift, the transfer is described by **thermal diffusion**. In this case, the charge movement occurs by the gradient of the charge concentration, causing an entropy-

driven current. Consequently, the charge redistributes from a region with higher concentration to a region with lower concentration until an equilibrium state is reached. This concentration gradient evokes a diffusion current which can be described by Fick's Law [49][50]

$$j_{\text{diff}}(x,t) = -\mathrm{q} \cdot D_{\text{n}} \cdot \frac{\partial n(x,t)}{\partial x}, \tag{5.8}$$

where the diffusion constant D_{n} is given by the Einstein relation [51] which is defined as

$$D_{\text{n}} = \frac{k_{\text{B}} T}{\mathrm{q}} \mu_{\text{n}} \tag{5.9}$$

with the Boltzmann constant k_{B} and the absolute temperature T. As can be seen, a higher temperature results in higher current density. Therefore, the time constant needs to be inversely proportional upon the absolute temperature $\tau_{\text{diff}} \sim T^{-1}$ [36]. Further, thermal diffusion acts in general for small charge packets. However, in comparison with the fringing-field the effect of the thermal diffusion is, especially for gate lengths $L < 10\ \mu\text{m}$, negligible in most cases [46][50].

5.2 Transfer Dynamics

The drift and diffusion current affect the charge motion between potential wells simultaneously. Hence, the total current density $j(x,t)$ is given by the sum

$$j(x,t) = -\,\mathrm{q} \cdot \mu_{\text{n}} \cdot n(x,t) \cdot [E_{\text{sid}}(x,t) + E_{\text{ff}}(x,t)] - \mathrm{q} \cdot D_{\text{n}} \cdot \partial_x n(x,t) \tag{5.10}$$

which is composed of the current density contributions of the transfer mechanisms. Since the difference of charge carriers flowing in and out of a volume $A\mathrm{d}x$ with infinitesimal thickness $\mathrm{d}x$ is equivalent to a temporal change of the electric charge carrier density n in this volume, the overall change in the number of charge carriers is given by

$$\frac{\partial n}{\partial t} A\mathrm{d}x = \frac{j_{\text{n}}(x)A}{-\mathrm{q}} - \frac{j_{\text{n}}(x+\mathrm{d}x)A}{-\mathrm{q}} \tag{5.11}$$

which is depicted in Figure 5.2.

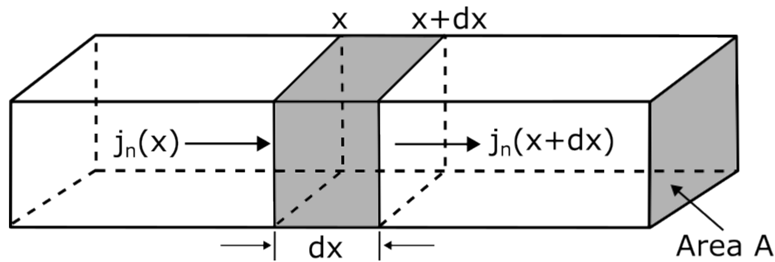

Figure 5.2: Current flow in an infinitesimal slice of thickness dx.

The derivation for an infinitesimal spatial expansion d$x \to 0$ yields the continuity equation

$$\frac{\partial n(x,t)}{\partial t} = -\frac{1}{\mathrm{q}}\frac{\partial j(x,t)}{\partial x} \tag{5.12}$$

which describes the law of charge conservation.

Combining current density and continuity equation, we obtain the following nonlinear parabolic partial differential equation (PDE)

$$\frac{\partial n}{\partial t} = D_{\mathrm{n}}\frac{\partial^2 n}{\partial x^2} + \mu_{\mathrm{n}} E_{\mathrm{ff}}\frac{\partial n}{\partial x} + \mu_{\mathrm{n}} n\frac{\partial E_{\mathrm{ff}}}{\partial x} + \frac{\mathrm{q}\mu_{\mathrm{n}}}{C_{\mathrm{eff}}}\frac{\partial}{\partial x}\left(n\frac{\partial n}{\partial x}\right), \tag{5.13}$$

which describes the process of charge transfer where x denotes the spatial coordinate within one gate $x \in [0, L]$.

However, since for gate lengths $L < 10$ μm the transfer of small charge packets is dominated by the fringing-field drift, the thermal diffusion can be neglected, i.e. $D_{\mathrm{n}} = 0$ [36]. Moreover, stipulate that subsequently, the denotation E_{ff} will correspond to the minimal fringing-field $E_{\mathrm{ff,min}}$, and assuming a local constant fringing-field $\partial_x E_{\mathrm{ff}} = 0$ yields the differential equation

$$\frac{\partial n}{\partial t} = \mu_{\mathrm{n}} E_{\mathrm{ff}}\frac{\partial n}{\partial x} + \frac{\mathrm{q}\mu_{\mathrm{n}}}{C_{\mathrm{eff}}}\frac{\partial}{\partial x}\left(n\frac{\partial n}{\partial x}\right). \tag{5.14}$$

To obtain a general solution a conversion to a simplified form is required. For this, we first use the substitution

$$a = \frac{\mathrm{q}\mu_{\mathrm{n}}}{C_{\mathrm{eff}}} \qquad \text{and} \qquad f = \mu_{\mathrm{n}} E_{\mathrm{ff}} \tag{5.15}$$

and apply afterwards the transformation

$$u(z,t) = n(x,t) \qquad \text{and} \qquad z = x + \int f dt. \tag{5.16}$$

The conversion of the PDE is obtained by determining the total differentials of $n(x,t)$ according to

$$\frac{\partial n}{\partial t} = \frac{\partial u}{\partial z}\frac{\partial z}{\partial t} + \frac{\partial u}{\partial t}\frac{\partial t}{\partial t} = \frac{\partial u}{\partial z}\frac{\partial z}{\partial t} + \frac{\partial u}{\partial t} \tag{5.17}$$

$$\frac{\partial n}{\partial x} = \frac{\partial u}{\partial z}\frac{\partial z}{\partial x} + \frac{\partial u}{\partial t}\frac{\partial t}{\partial x} = \frac{\partial u}{\partial z} \tag{5.18}$$

and

$$\frac{\partial^2 n}{\partial x^2} = \frac{\partial^2 u}{\partial z^2}\left(\frac{\partial z}{\partial x}\right)^2 + 2\frac{\partial^2 u}{\partial x \partial t}\frac{\partial z}{\partial x}\frac{\partial t}{\partial x} + \frac{\partial^2 u}{\partial t^2}\left(\frac{\partial t}{\partial x}\right)^2 + \frac{\partial u}{\partial z}\frac{\partial^2 z}{\partial x^2} + \frac{\partial u}{\partial t}\frac{\partial^2 t}{\partial x^2} = \frac{\partial^2 u}{\partial z^2} \tag{5.19}$$

Finally, the PDE defined by Eq.(5.13) can be converted to the form

$$\frac{\partial u}{\partial t} = au\frac{\partial^2 u}{\partial z^2} + a\left(\frac{\partial u}{\partial z}\right)^2 = a\frac{\partial}{\partial z}\left(u\frac{\partial u}{\partial z}\right) \tag{5.20}$$

where the general solution is obtained by solving this PDE leading to [52]

$$u(z,t) = -\frac{(z+\mathrm{c}_1)^2}{6a(t+\mathrm{c}_2)} + \frac{\mathrm{c}_3}{|t+\mathrm{c}_2|^{1/3}}. \tag{5.21}$$

Consequently, the re-transformation results in the transfer equation

$$n(x,t) = -\frac{(x+ft+\mathrm{c}_1)^2}{6a(t+\mathrm{c}_2)} + \frac{\mathrm{c}_3}{|t+\mathrm{c}_2|^{1/3}} \tag{5.22}$$

where c_1, c_2 and c_3 are constants and the spatial and temporal derivations are obtained by

$$\frac{\partial n(x,t)}{\partial x} = -\frac{k(x,t)}{3a(t+\mathrm{c}_2)} \tag{5.23}$$

and

$$\frac{\partial n(x,t)}{\partial t} = \frac{k(x,t)^2}{6a(t+\mathrm{c}_2)^2} - \frac{\mathrm{c}_3}{3(t+\mathrm{c}_2)^{\frac{4}{3}}} - \frac{fk(x,t)}{3a(t+\mathrm{c}_2)} \tag{5.24}$$

where the substitution $k(x,t) = ft + x + \mathrm{c}_1$ is used.

5.3 Transfer Analysis

An analytical equation that describes the transfer process in good approximation is obtained by defining proper boundary conditions and determining the transfer constants c_1, c_2, and c_3.
For this, we first stipulate that the transfer electrode potential is midway between the blocking and receiving electrode potential.
This leads to the assumption that the highest initial charge carrier density n_0 is located at the position $x = 0$, defining the first boundary condition

$$n(x = 0, t = 0) = n_0. \tag{5.25}$$

Furthermore, considering a perfect sink at position $x = L$ indicates that the charge carrier density has to be zero. Consequently, we obtain the condition

$$n(x = L, t = 0) = 0. \tag{5.26}$$

At last, since the transfer of charge corresponds to a unidirectional flow of the charger carriers, we assume the existence of an infinite potential barrier at position $x = 0$, which results in

$$\partial_t n(x = 0, t = 0) = 0. \tag{5.27}$$

Thus, by applying this boundary condition, we obtain a system of equations that can be used to determine the constants c_1, c_2, and c_3. The solution yields

$$c_1 = \frac{L}{4\left(n_0 - \frac{fL}{a}\right)}\left[\left(2n_0 + \frac{fL}{a}\right) \pm \sqrt{12n_0^2 - \frac{4n_0 fL}{a} + \left(\frac{fL}{a}\right)^2}\right], \tag{5.28}$$

$$c_2 = L \cdot \left(\frac{L + 2c_1}{6 \cdot a \cdot n_0}\right) \quad \text{and} \quad c_3 = \left(n_0 + \frac{c_1^2}{6 \cdot a \cdot c_2}\right) c_2^{1/3} \tag{5.29}$$

Here, c_1 has the dimension of a length in cm, c_2 is the time constant $\tau = c_2$ in seconds s and the dimension of c_3 is $s^{1/3}cm^{-2}$.
These results allow us to calculate the distribution of the charge carrier density $n(x, t)$ within a potential well. For this we set the parameters $L = 0.5 \cdot 10^{-3}$ cm, $\mu_n = 1350$ cm^2/V^{-1}s^{-1} and $C_{eff} = 2 \cdot 10^{-8}$ Fcm^{-2}.
Because of the boundary conditions and the fact that the potential well is situated between a blocking and a receiving electrode, we obtain at equilibrium a charge

density that is in good approach Poisson distributed. Here, at $x = 0$, the charge carrier density n_0 increases until the highest charge carrier density $1.5n_0$ is reached and then starts to decrease while approaching the edge of the sink where it yields $n(x = L, t = 0) = 0$. This is shown in Figure 5.3, for various initial charge carrier densities $n_0 = n(x = 0, t = 0)$.

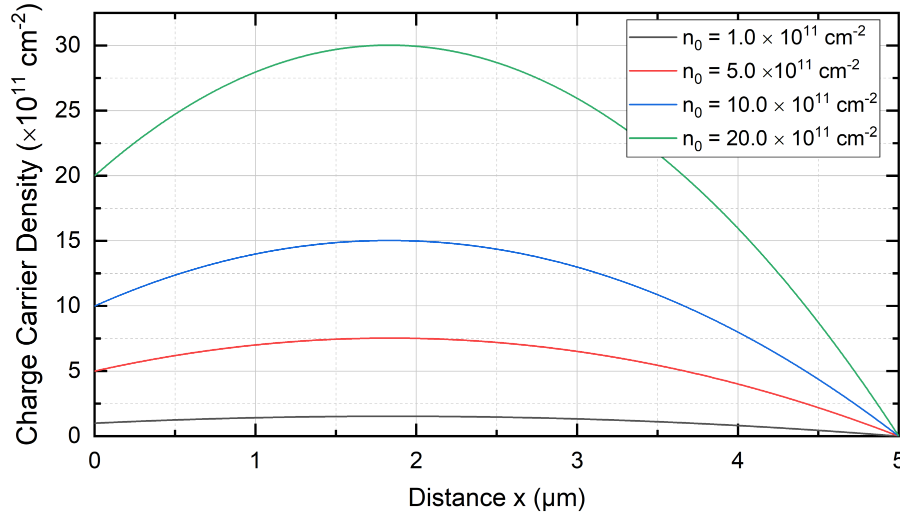

Figure 5.3: Charge distribution in the potential well for various n_0 at $t = 0$. The potential well verges on a potential barrier at $x = 0$ and a deeper potential well at $x = L$.

The spatial gradient of $n(x, t)$ indicates the strength of the self-induced drift field according to Eq.(5.4). This can be observed in Figure 5.4 where the spatial derivation of $n(x, t)$ is plotted versus the distance for $t = 0$. At the position of the highest charge density, the self-induced drift is $E_{\text{sid}} = 0$ since $\partial n/\partial x = 0$, i.e., the repulsive forces at this location neutralize. However, on the left, respectively, on the right-hand side, the gradient shows two different polarities stating the direction of the self-induced drift field. As a consequence, the electrons are pushed in the direction of the blocking electrode at $x = 0$ for negative polarity, whereas the positive polarity causes a shift in the direction of the sink at $x = L$. Here, the absolute values of the spatial-gradient prove that the condition of an increasing self-induced drift field for an increasing number of charge carriers is fulfilled.

Comparing these with results obtained in existing literature, a close resemblance is found. Hence, this model is qualified to describe the charge distribution within

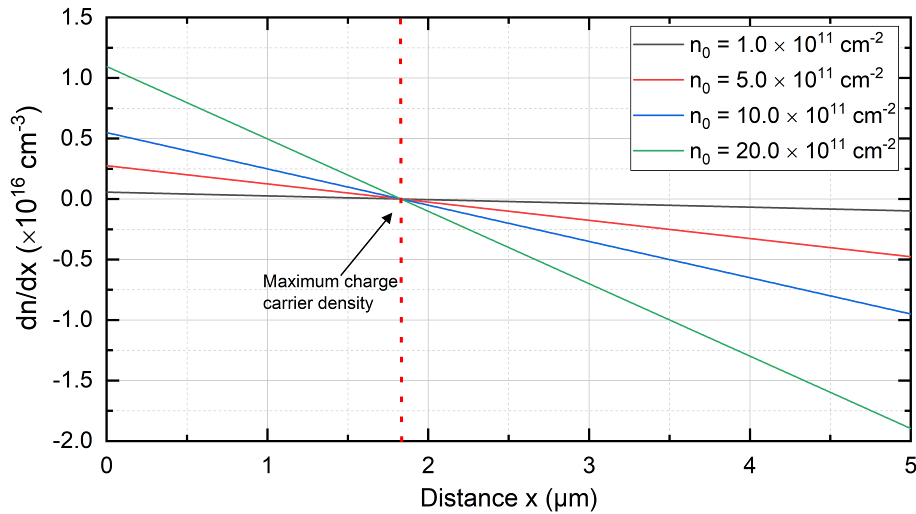

Figure 5.4: Spatial behavior of $n(x,t)$ at $t = 0$.

a potential well. The subsequent section investigates the transfer inefficiency in dependence on the time to verify the temporal behavior.

5.3.1 Simulation of the Transfer Inefficiency

The charge carrier density $n(x,t)$ gives the spatial-temporal behavior of the charge within a potential well. To calculate the efficiency of the transfer concerning the difference in gate clocking and transfer time, an equation that yields the charge remaining in the potential well after time t needs to be determined. This is achieved by integrating $n(x,t)$ over the gate length L, which results in

$$Q(t) = \int_0^L n(x,t)\mathrm{dx} = -\frac{L}{3}\frac{(L^2 + 3(c_1 + ft)(c_1 + ft + L))}{6 \cdot a \cdot (t + c_2)} + \frac{Lc_3}{(t + c_2)^{\frac{1}{3}}}. \tag{5.30}$$

This equation describes the temporal change of total charge carriers under the transfer gate. Consequently, the **transfer inefficiency** per shift ϵ can be defined as the ratio of the remaining charge under the transfer gate $Q(t)$ and the initial number of charge carriers $Q(0)$:

$$\epsilon(t) := \frac{Q(t)}{Q(0)} \tag{5.31}$$

Equivalent, the charge **transfer efficiency** per shift γ is defined as:

$$\gamma(t) = 1 - \epsilon(t) = 1 - \frac{Q(t)}{Q(0)} \tag{5.32}$$

Several simulations with different parameters have been made to investigate the transfer mechanisms' contributions to the transfer efficiency and verify the derived transfer model. The results are presented in Figure 5.5 and Figure 5.6 where the transfer efficiency versus time is depicted for various initial charge carrier densities n_0, respectively fringing fields E_{ff}.

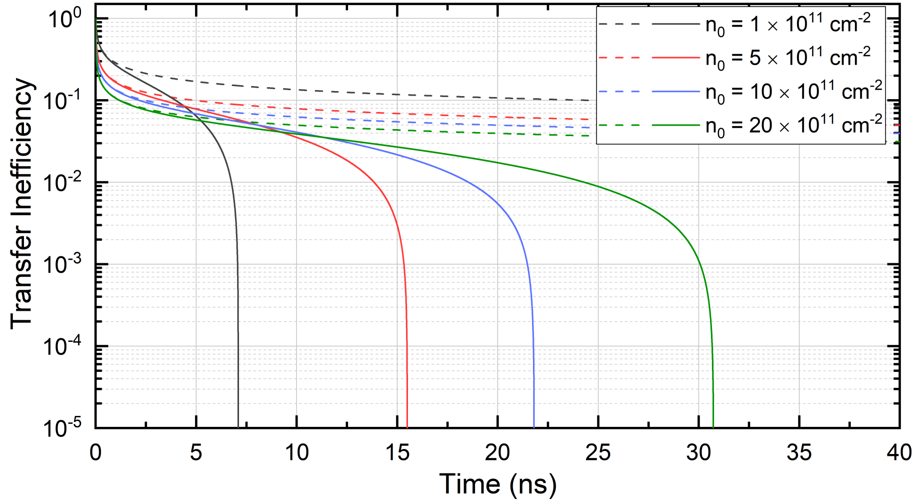

Figure 5.5: Time-dependent transfer inefficiency for various initial charge carrier densities n_0, i.e., self-induced drift fields. Solid lines indicate the impact of a constant fringing-field $E_{\text{ff}} = -300$ Vcm^{-1} on the transfer inefficiency. Dashed lines show the charge transfer in the absence of the fringing-field $E_{\text{ff}} = 0$.

The initial charge transfer is mainly driven by the self-induced drift which is affected proportionally by the initial charge carrier density n_0. As the charge density in the potential well decreases, the impact of the self-induced drift becomes negligible, causing the transfer of the remaining charge to proceed mainly by the fringing-field drift. This is proven by the plots in Figure 5.5. Comparing the transfer inefficiencies in the presence (solid line) and absence (dashed line) of the fringing field, it can be seen that the curves overlap at the beginning. However, as time progresses, the interaction of self-induced drift and fringing-field drift yields a significantly lower transfer inefficiency in an appropriate amount of time.
Moreover, if only the self-induced drift is considered, a lower transfer inefficiency is obtained by a higher charge carrier density n_0. This can also be observed for the initial transfer in the presence of a fringing-field. Nevertheless, as the fring-

ing field becomes the dominating transfer mechanism, it will take more time to achieve a particular transfer inefficiency for higher n_0 since a higher amount of remaining charge carriers needs to be transferred by the fringing-field.

As shown in Figure 5.5, the timescale for reaching a transfer inefficiency of $\epsilon = 10^{-5}$ lies within a few 10ns, which is valid for this particular parameter set used in the simulation. Consequently, in this case, the maximum line frequency is in the order of MHz. Exemplary, with the previous listed parameters and an initial charge carrier density $n_0 = 20 \cdot 10^{11}$ cm^{-2} the maximum line frequency for reaching at least $\epsilon = 10^{-5}$ with a four-phase overlapping clock pattern is $f_{\text{line}} = 31.25$ MHz. However, the charge transfer efficiency, respectively the line frequency can vary depending on the choice of device design parameters. Therefore, these dependencies will be thematized and summarized in Section 5.4.
Nevertheless, the variation in charge packet size relating to TDI mode affects the charge transfer considerably, especially since it has been shown that a higher time is required to transfer larger charge packets. As a result, continuously increasing charge due to the time-delay integration mode causes an increment of transfer inefficiency [48].
Further, the fringing-field is negligible as the accumulated charge reaches a specific size since, in this case, the adjacent potential well can not be assumed as a perfect sink anymore. Henceforth, the charge is only driven by the self-induced drift, causing a considerable degradation of the charge transfer as shown in Figure 5.5. It can be concluded that the line frequency has to be chosen such that the transfer inefficiency is low for larger charge packets approaching full well capacity. Therefore, these aspects must be considered when choosing the line rate of the CCD.

The impact of various fringing-fields E_{ff} on the transfer inefficiency with constant n_0 is shown in Figure 5.6. Here, a higher absolute E_{ff} results in a faster transfer of charge carriers. Although we assumed a constant self-induced drift in these plots, it can be observed that the contribution of the self-induced drift decreases as the absolute fringing-field increases. This supports the statement that the self-induced drift dominates initially for large charge packets but is being replaced by the fringing-field drift as the charge carrier density, i.e., the total

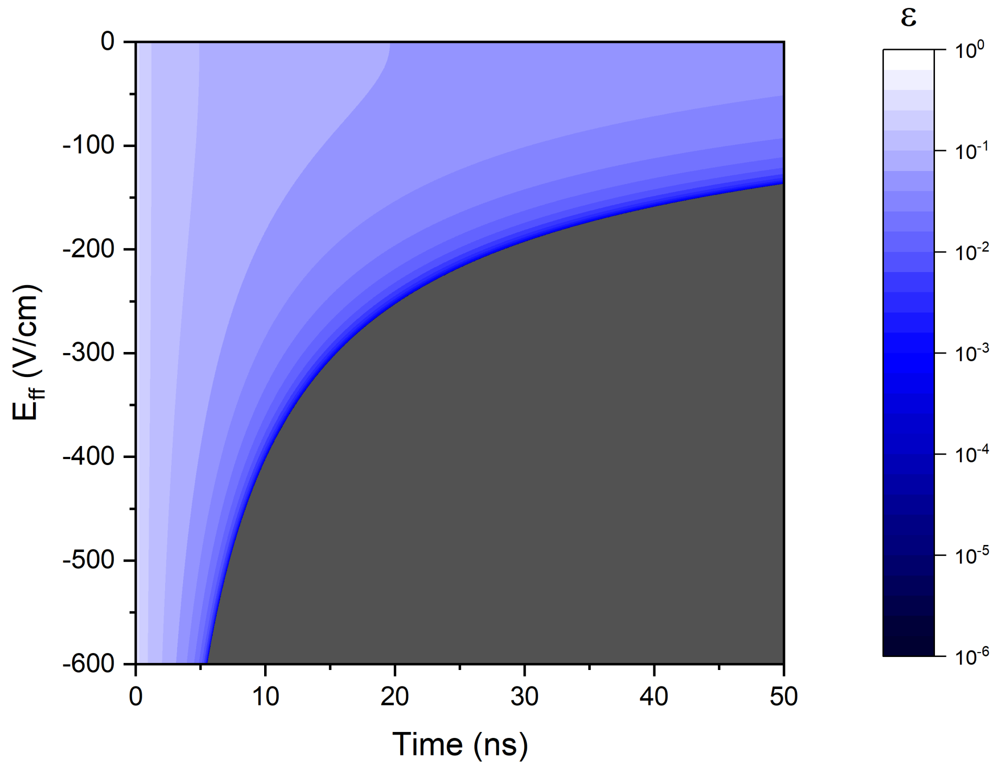

Figure 5.6: Transfer inefficiency ϵ in dependence on the fringing-field E_{ff} and the time t for a constant self-induced drift field ($n_0 = 5 \cdot 10^{11}$ cm^{-2}).

amount of charge carriers decreases.

The transfer inefficiencies shown in Figure 5.5 and 5.6 reflect the charge loss for one shifting process, depending enormously on the device parameters, the size of the charge packet, and the line frequency. However, since multiple shifts are required to transfer the charge across a pixel column, the particular transfer efficiencies multiply, causing a stronger degradation in total. Therefore, to investigate how the charge transfer efficiency and the modulation transfer function are affected by varying transfer inefficiencies for a particular number of transfer processes, the following section provides an analysis of both these quantities.

5.3.2 CTE and MTF

The derived transfer model enables the calculation of the transfer inefficiency ϵ between two adjacent potential wells caused due slow charge transfer with respect to the gate clocking. Consequently, assuming a constant ϵ, the total charge transfer efficiency CTE after a certain number of shifts N can be calculated according to

$$\text{CTE} = (1 - \epsilon)^N. \tag{5.33}$$

Furthermore, the total MTF of an optical system is composed of the product of all MTF contributions, where one of these contributions concerns the transfer process [53]. Hence, the transfer MTF is associated with the transfer efficiency and is given by [54]

$$\text{MTF}_{\text{transfer,y}} = \frac{1}{N(a^2 + b^2)}(c^2 + d^2)^{0.5} \tag{5.34}$$

where the substitutions

$$c^2 = \left(a - e^{-Na} \cdot [a \cdot \cos(Nb) - b \cdot \sin(Nb)]\right)^2 \tag{5.35}$$

$$d^2 = \left(b - e^{-Na} \cdot [a \cdot \sin(Nb) + b \cdot \cos(Nb)]\right)^2 \tag{5.36}$$

as well as

$$a = \epsilon \cdot \left[1 - \cos\left(\frac{\pi f}{f_\text{N}}\right)\right] \qquad \text{and} \qquad b = \epsilon \cdot \sin\left(\frac{\pi f}{f_\text{N}}\right) \tag{5.37}$$

where made. If the spatial Nyquist-Frequency $f = f_\text{N}$ is assumed, which is defined as one-half of the sampling rate, the transfer MTF can be simplified to the form [55]

$$\text{MTF}(f_\text{N}) = \frac{1 - \exp(-2\epsilon N)}{2\epsilon N}. \tag{5.38}$$

Here, the Nyquist frequency f_N states the upper limit, i.e., every signal frequency has to be below the Nyquist frequency $f_\text{s} < f_\text{N}$ to be reconstructed. Otherwise, aliasing can occur, which is an effect that causes different signals to become indistinguishable when sampled. Primarily, in digital imaging, this effect is referred to as spatial aliasing and results in a moire' pattern, an interference of identical but displaced patterns.

A simulation of the CTE and the MTF at Nyquist frequency is plotted in Figure 5.7 for varying transfer inefficiencies ϵ. As can be observed, this degradation affects the transfer stronger for a higher transfer inefficiency ϵ and increases with the number of TDI stages. Moreover, since the modulation transfer function is considered at the Nyquist frequency, the MTF plots state the highest possible degradation due to transfer. Hence, charge loss concerning the transfer process should be prevented since a worsening of the CTE and MTF means degradation of contrast and resolution.

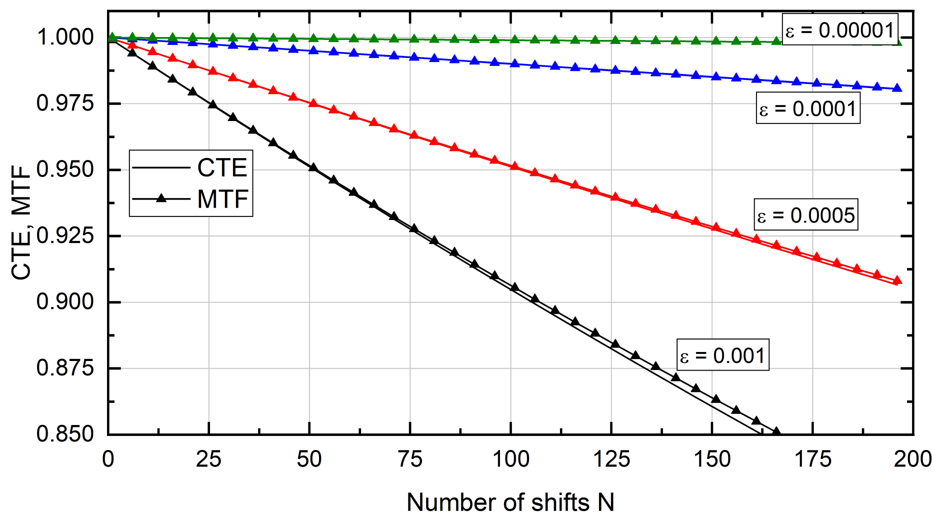

Figure 5.7: CTE and MTF in dependence on the number of shifts N for various transfer inefficiencies ϵ.

The influence of a degrading charge transfer efficiency on the modulation transfer function can be observed in Figure 5.8. Depicted are three sine patterns with logarithmically increasing line pairs per mm (lp/mm), i.e., decreasing spatial frequencies, which differ in contrast levels. The first pattern (a) has ideal line edges and achieves, even at very low spatial frequencies, a contrast of 100 percent. However, in a real system, charge loss can not be prevented. Depending on the transfer inefficiency per shift ϵ, the MTF contribution for the transfer is degraded, resulting in a degradation of the total MTF. Therefore, in (b) and (c), this chart pattern is shown for different degradation levels to depict how the contrast is affected at differing spatial frequencies. Here a worsened image quality applies to a worsened CTE, respectively MTF and vice versa.

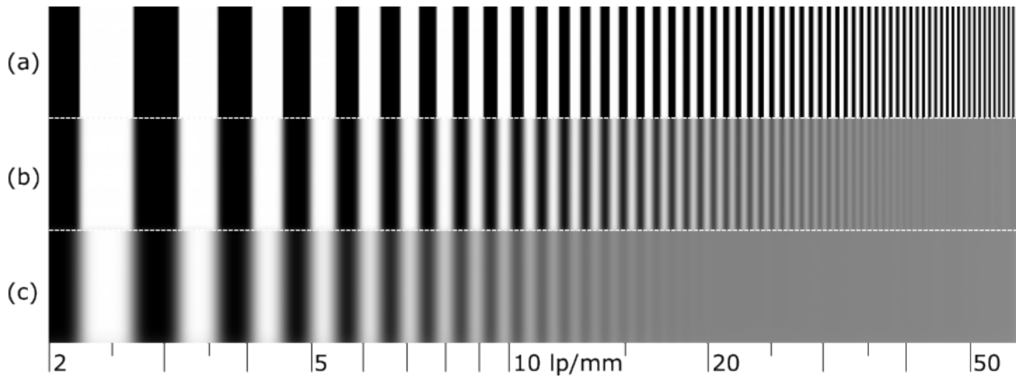

Figure 5.8: Periodic bar pattern with increasing line pairs per mm. (a) Pattern with perfect line edges. (b,c) Bar pattern for two different levels of image degradation.

The change of these contrast levels can be visualized by plotting the relative luminance versus the line pairs, as shown in Figure 5.9. Since a lower charge transfer efficiency causes a degradation of the MTF, the contrast and, consequently, the total image quality will be degraded. Hence, a stronger decay of the sine amplitude will appear, as Figure 5.9 suggests. Thus, an optimized charge transfer process with minimized charge losses is inevitable.

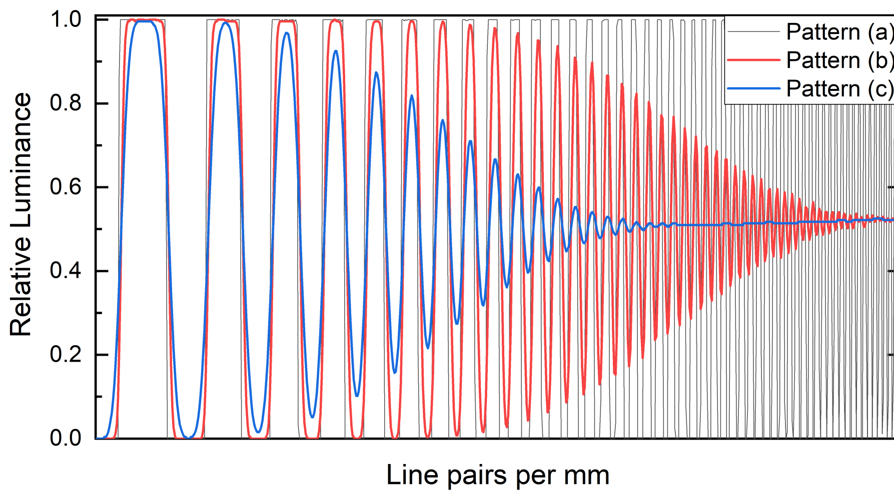

Figure 5.9: Relative luminance versus line pairs per mm for three different degradation models.

According to the derived transfer model, the design parameters considerably

affect the charge transfer and modulation transfer function. Therefore, to clarify these coherences in terms of device optimization, a discussion of the crucial design parameters will be provided in the subsequent section.

5.4 Discussion of Design Parameters

The charge transfer is strongly influenced by the design parameters of the device, as seen in the derived transfer model. To conclude how each of these parameters affects the charge transfer and thus the image quality, we regard at first the time constant

$$\tau = L \cdot \left(\frac{L + 2\mathrm{c}_1}{6an_0} \right) = C_{\mathrm{eff}} \cdot L \cdot \left(\frac{L + 2\mathrm{c}_1}{6\mathrm{q}\mu_{\mathrm{n}} n_0} \right), \tag{5.39}$$

which represents the time required for the charge to decrease to 1/e of its initial value, i.e., a higher time constant yields a slower charge transfer.
As can be seen, the time constant scales quadratic with the gate length L. Since a higher time constant requires a higher time to reach a particular CTE, the CTE increases with decreasing gate length. Moreover, the time constant scales inverse linearly with the mobility μ_{n} which is doping dependent, i.e. after Chen et al. [56], a higher doping concentration N_{d} causes a decrement in mobility.
The effective capacitance C_{eff} can be expressed in dependence on the oxide thickness d_{ox} and in the case of a buried-channel CCD in dependence on the depletion width t_{d}, yielding the distance from oxide to the potential maximum. Thus, the effective capacitance is given by

$$C_{\mathrm{eff}}^{-1} = \frac{d_{\mathrm{ox}}}{\epsilon_{\mathrm{ox}}} + \frac{1}{\epsilon_{\mathrm{si}}} \left(t_{\mathrm{d}} - \Delta t - \frac{Q_{\mathrm{sig}}}{2N_{\mathrm{d}}} \right), \tag{5.40}$$

where the doping concentration contributes to C_{eff} for $Q_{\mathrm{sig}} > 0$. Consequently, a smaller effective capacitance is in favor of acquiring a faster charge transfer. However, as the charge in the potential well increases, the depletion region, i.e., t_{d}, becomes smaller, causing an increment of the effective capacitance. This must be considered especially concerning TDI CCDs, where the charge increases continuously. At last, it can be seen that the temporal behavior in Equation 5.30 is also dependent on the minimal fringing-field $E_{\mathrm{ff,min}}$. In accordance with the expression 5.7 the fringing-field scales linearly with the applied gate voltage. Furthermore, the oxide thickness and the depletion width contribute proportionally

to the strength of this field.
Hence, through an appropriate choice of design parameters, the transfer of charge carriers across the CCD can be influenced considerably. In conclusion, the CTE...

(1) ... increases with decreasing gate length L.

(2) ... increases with increasing mobility μ_n. Since the mobility is doping dependent and decreases with higher concentration N_d, the CTE decreases for higher doping concentrations as well.

(3) ... increases with decreasing effective capacitance C_eff. Here, the capacitance depends on the oxide thickness d_ox, the depletion width t_d, and the doping concentration N_d.

(4) ... increases with increasing absolute fringing-field $E_\mathrm{ff,min}$ which depends on L, d_ox, and d_si.

This discussion shows that an increment in CTE, respectively, MTF, requires an appropriate adjustment of the design parameters to obtain the desired sensor performance, which can be achieved with the presented transfer model.

5.5 Summary

The derived analytical model describes the temporal-spatial behavior of the charge carrier density inside a potential well. However, the derived model can take all three transfer mechanisms simultaneously into account. Hence, this model enables a more detailed investigation of the charge transfer with regard to crucial device parameters like gate length, doping concentration, and oxide and silicon thickness. Moreover, the integration over the potential well length allows calculating the charge transfer (in)efficiency and, consequently, analyzing the dynamic MTF. Nevertheless, this model is exceptionally qualified for investigating the behavior of TDI CCDs since the change in transfer speed depending on the accumulated charge can be calculated. Out of this, further design improvements can be carried out until the sensor fulfills the requirements.

Chapter 6

Impact of Interface States on TDI

Defects and imperfections located at the Si/SiO_2 interface can affect the performance and characteristics of semiconductor devices. Due to continuous charge accumulation, as a consequence of the time-delay integration mode, charge packets in a buried-channel CCD approach this interface region. The interaction with this defect states results in trapping of charge carriers and thus in a degradation of the CTE. Therefore, the goal of this chapter is to investigate the behavior and impact of recombination at the interface with respect to an increasing number of charge carriers.

In the subsequent sections an explanation of the formation of interface defects and the interaction with signal charges is given first. The injection of different-sized charge packets according to the fill-and-spill method into a buried-channel CCD will be simulated and the corresponding transfer efficiency after one shift is determined. An approach to describe the CTE after N_{TDI} stages will be presented. Finally, measurements with optical and electrical injection of charge carriers are performed. A method to determine the CTE for a particular number of TDI stages using responsivity measurements will be presented.

6.1 Carrier Exchange at the Interface States

The occurrence of defect states in MOS or Si/SiO_2 structures is unavoidable and can originate from different reasons. In general, these defect states are caused due to technological processes and can significantly affect the electrical properties of a device. Especially at the Si/SiO_2 interface, the electronic properties are dominated by so-called silicon dangling bonds [57] whose generation can be explained as follows. The deposition of SiO_2 on a Si substrate forms an interface region where the deviation of the lattice parameters creates interface traps, also referred to as interface states (or surface states). These interface states are generally unpaired electrons with energy levels located in the forbidden band gap, i.e., dangling bonds are formed by atoms that possess too few bonding partners to fill their valence shell with electrons.

According to this, the discontinuity in the lattice structure induces interface states, resulting in generation-recombination centers providing an increased exchange interaction. Subsequently, four different exchange mechanisms can occur, as depicted in Figure 6.1, whereby electrons or holes can be trapped by an interface state, depending on the ionization energy of the defect level. The first

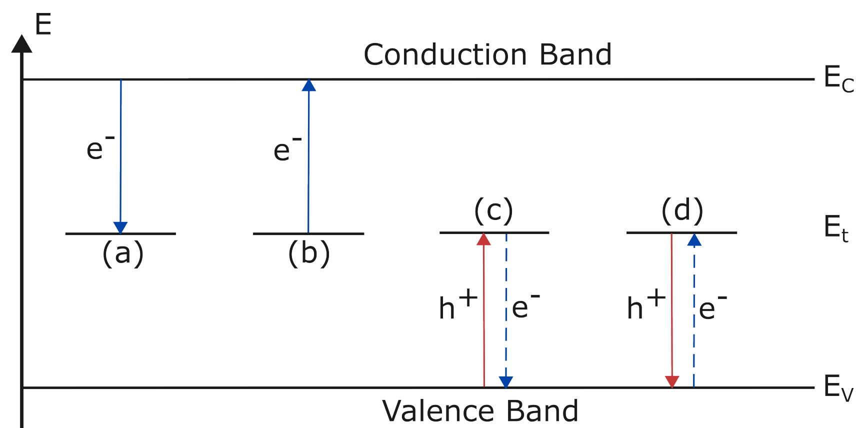

Figure 6.1: A representation of the four exchange mechanisms at the interface: (1) electron capture, (2) electron emission, (3) hole capture, and (4) hole emission.

process is the recombination of an electron in the conduction band by an interface state located in the band gap at trap level E_t. Consequently, the second process denotes the emission of an electron into the conduction band by a previously-

filled interface state. Analogously, the recombination and emission of holes are described. Here, the recombination of holes occurs by emitting an electron from the trap level into the valence band. Similarly, hole emission takes place if an electron from the valence band recombines with an interface state.
Here, the emission processes shown in (b) and (d) occur because of thermal excitation after a particular mean lifetime, which is shorter for higher absolute temperatures T.

The recombination of electrons and holes due to defect states in a semiconductor can be described by Shockley-Read-Hall (SRH) theory [58]. Since the surface state levels are continuously distributed, the recombination rate is obtained by integration over the band gap [59][60]

$$U_\mathrm{s} = \int_{E_\mathrm{V}}^{E_\mathrm{C}} \frac{v_\mathrm{th}\sigma_\mathrm{p}\sigma_\mathrm{n}D_\mathrm{it}(E_\mathrm{t})\,(p_\mathrm{s}n_\mathrm{s} - n_\mathrm{i}^2)\,\mathrm{d}E_\mathrm{t}}{\sigma_\mathrm{n}(n_\mathrm{s} + n_\mathrm{i}\mathrm{e}^{(E_\mathrm{t}-E_\mathrm{i})/k_\mathrm{B}T}) + \sigma_\mathrm{p}(p_\mathrm{s} + n_\mathrm{i}\mathrm{e}^{(E_\mathrm{i}-E_\mathrm{t})/k_\mathrm{B}T})} \tag{6.1}$$

where σ_n and σ_p denote the energy-dependent capture cross sections of electrons and holes, p_s and n_s are the concentration of holes and electrons at the surface, D_it is the energy-dependent interface state density, v_th the thermal velocity, and E_t the trap energy level.
Moreover, the surface recombination velocity S_v can be defined as [61]

$$S_\mathrm{v} = \frac{U_\mathrm{s}}{(p_\mathrm{s}n_\mathrm{s} - n_\mathrm{i}^2)} = \int_{E_\mathrm{V}}^{E_\mathrm{C}} \frac{v_\mathrm{th}\sigma_\mathrm{p}\sigma_\mathrm{n}D_\mathrm{it}(E_\mathrm{t})\mathrm{d}E_\mathrm{t}}{\sigma_\mathrm{n}(n_\mathrm{s} + n_\mathrm{i}\mathrm{e}^{(E_\mathrm{t}-E_\mathrm{i})/k_\mathrm{B}T}) + \sigma_\mathrm{p}(p_\mathrm{s} + n_\mathrm{i}\mathrm{e}^{(E_\mathrm{i}-E_\mathrm{t})/k_\mathrm{B}T})}. \tag{6.2}$$

Here, the time constant for recombination τ_r is inversely proportional to the surface velocity [62], i.e., $\tau_\mathrm{r} \sim 1/S_\mathrm{v}$. Further, the time constant shows, in general, the dependence $\tau_\mathrm{r} \sim (\sigma_\mathrm{n}\sigma_\mathrm{p}v_\mathrm{th}\rho_\mathrm{trap})^{-1}$ [63], where ρ_trap is the recombination center density per unit area (=trap density). Hence, the time constant decreases for increasing σ and ρ_trap, i.e., the probability of charge trapping increases as well. However, describing the SRH surface recombination for a buried-channel CCD is quite complicated [64], especially when TDI CCDs are considered since a continuous accumulation causes a continuous change of the physical conditions. Therefore, the following sections will analyze the charge transfer efficiency in a buried-channel CCD and present a method to examine the CTE in the case of time-delay integration.

6.2 Simulation of the Transfer Efficiency

The previous section provided a brief introduction to the interface recombination process, showing the dependencies on the trap density, the trapping cross-section, and the charge carrier concentration at the surface, yielding an expression for the recombination process. This serves as the basis for deploying the following simulations and is used for comparing and verifying the obtained results. The subsequent sections present, at first, the deployed simulation setup and the fill-and-spill method used for electrical charge injection. Furthermore, a method to simulate the accumulation of charge carriers in a TDI CCD will be derived and discussed. At last, an analysis of the transfer efficiency for various parameter sets depending on the number of accumulated charge carriers is presented.

6.2.1 Simulation Setup for Charge-Injection

A 2-dimensional CCD structure was simulated with technology computer-aided design (TCAD) using the Synopsys Sentaurus software. The CCD structure has a p-type substrate with an n-type buried-channel and can be divided into three areas: an input structure, a pixel area, and an output structure, as shown in Figure 6.2. The input structure serves for electrical charge injection (fill-and-spill method) and consists of an n^+-diode and two input gates: ϕ_{DC} and ϕ_{IN}. The pixel area contains two pixels with a pixel pitch of 7 µm and four transfer gates ϕ, respectively. Finally, an output structure for readout with two gates ϕ_{SW} and ϕ_{TG} and a floating diffusion FD is present.

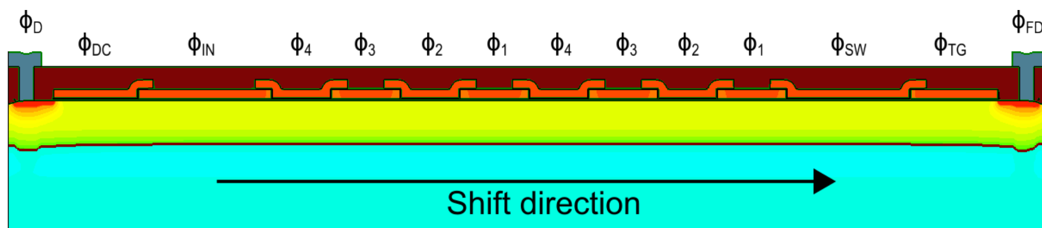

Figure 6.2: Cross-section of the simulated CCD structure. Charge is shifted from left to right.

6.2.2 Fill-and-Spill Method

The fill-and-spill (FaS) method is an electrical charge injection mechanism where the amount of injected charge carriers can be adjusted due to proper choice of the applied voltages V_{DC} and V_{IN}. The input structure and the corresponding fill-and-spill charge injection diagram are depicted in Figure 6.3 for a p-type charge-coupled device.

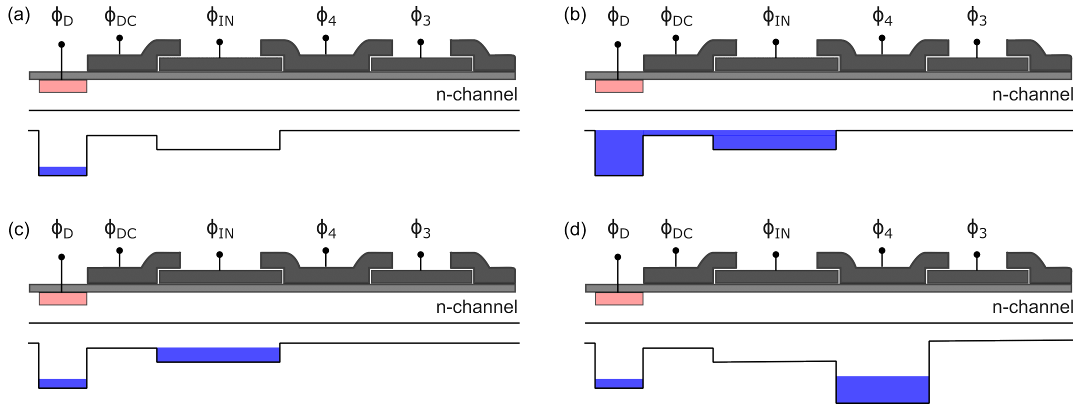

Figure 6.3: Charge injection structure and fill-and-spill method.

At the beginning of the fill-and-spill process, a voltage V_{IN} is applied to form a potential well. This potential well is isolated from the CCD channel by the blocking ϕ_4-gate as well as from the diode by a potential barrier under V_{DC}.
To initiate the charge injection process, the voltage V_{D} is decreased such that the diode potential is set above the barrier, causing the regions under the gates V_{DC} and V_{IN} to fill with electrons. By increasing V_{D} again, the electrons start to spill back into the diode. However, since V_{IN} forms a deeper potential well than the potential barrier V_{DC}, it prevents electrons which are under the V_{DC} potential level to spill back [19]. The remaining charge in the potential well can be transferred afterwards by clocking ϕ_4. The clocking pattern is depicted in Figure 6.4.

This residual charge Q_{inj} which remains in the potential well can be calculated by the potential difference between V_{IN} and V_{DC} according to

$$Q_{\mathrm{inj}} = C_{\mathrm{ox}} \cdot (V_{\mathrm{IN}} - V_{\mathrm{DC}}) \tag{6.3}$$

where C_{ox} denotes a constant oxide capacitance [65]. Nevertheless, the linearity of this equation is only valid for surface channel CCDs [66] and small charge

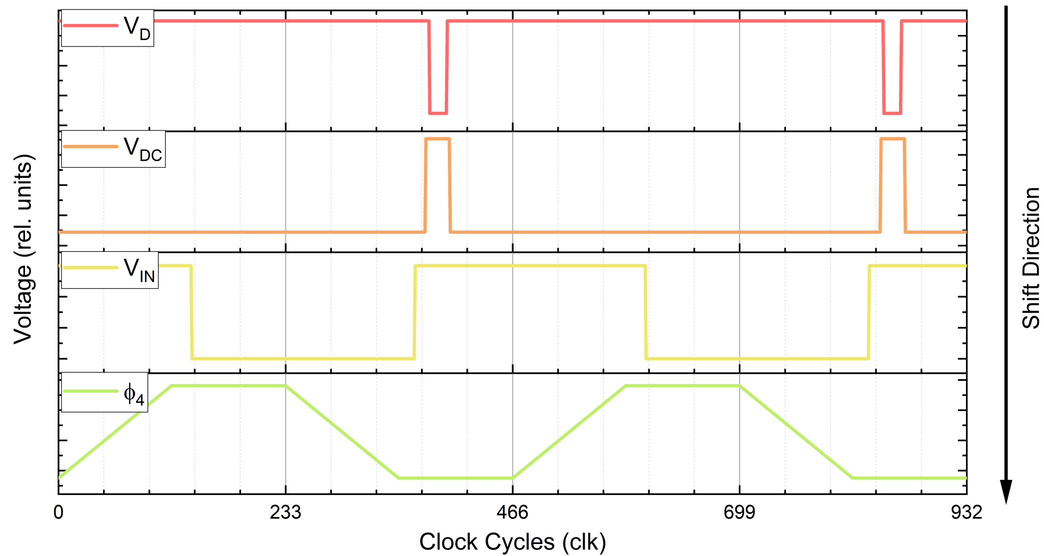

Figure 6.4: Clocking pattern for the fill-and-spill method.

packets [67]. In the case of buried channel CCDs, the capacitance depends on the signal charge level yielding a non-linear equation. The reason is a decreasing distance between gate and charge packet as the charge packet increases resulting in an increased capacitance as well [67][68]. Hence, the number of charge carriers scales non-linearly in relation to the injection voltage. This is shown in Figure 6.5 (top), where the charge carrier density in dependence on V_{IN} is depicted. Here, the non-linear behavior of the capacitance, which corresponds to the slope, can be also identified.

To further analyze the behavior of the capacitance, their dependence on the charge carrier density was determined, which is given at the bottom of Figure 6.5. Here the simulation indicates a non-linear behavior of the capacitance, proving an increment with an increasing number of charge carriers. Nevertheless, at some point, the capacitance scales linearly since the accumulated amount of charge expands towards the Si/SiO_2 interface. Henceforth, the buried channel CCD operates similarly to a surface channel CCD. These results indicate a decrement of the depletion width and, consequently, an approach towards the Si/SiO_2 on the one hand but also a decrement of the charge transfer time on the other hand, as discussed in the previous chapter.

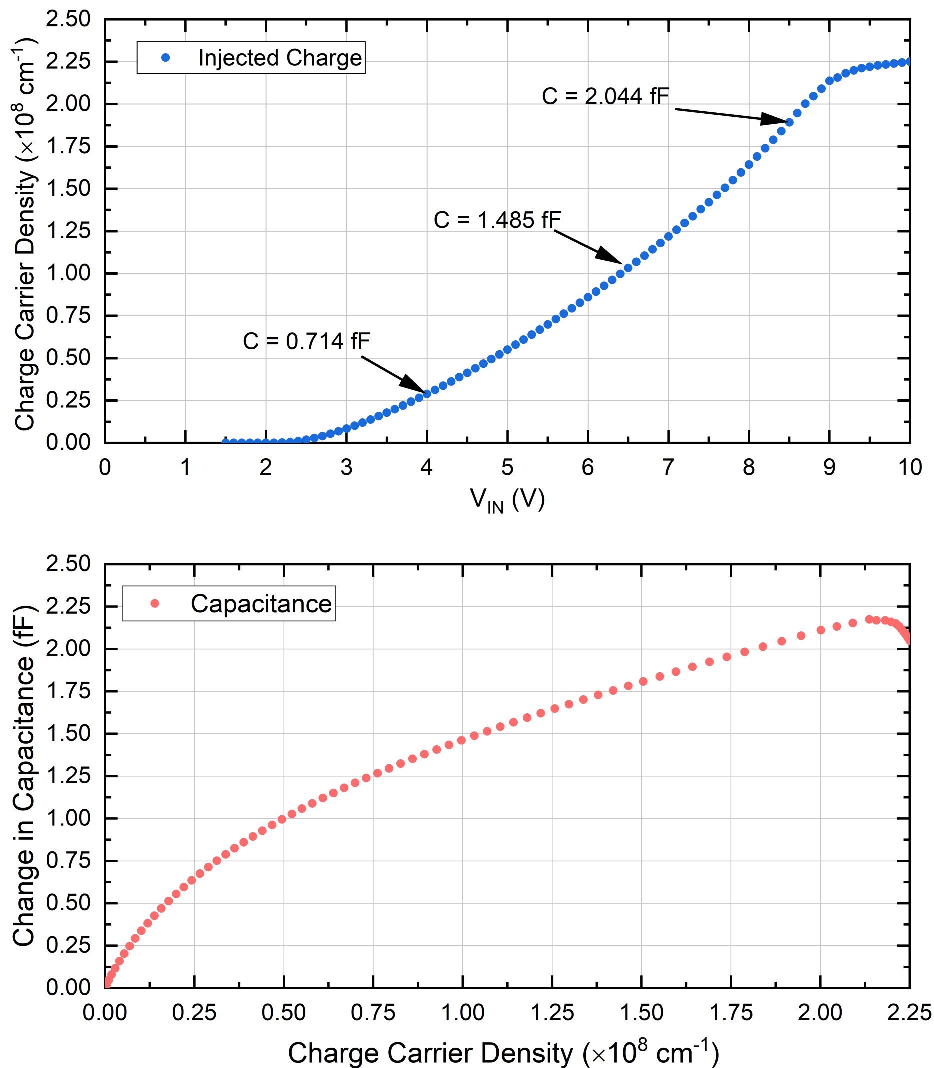

Figure 6.5: Simulation of the injected charge for a buried-channel CCD with two pixels and four subpixels, respectively. Charge carrier density versus injection voltage (top). Change in capacitance versus the charge carrier density (bottom).

6.2.3 Electrostatic Potential

The generated signal charge carriers are stored in the electrostatic potential maximum. However, this potential maximum will decrease and approach the interface as the number of signal charge carriers increases since the depletion region becomes smaller [69].

The corresponding surface potential ϕ_s, the location of the potential maximum

d_{max} and the signal charge Q_{sig} are related to each other according to

$$\phi_{\mathrm{s}} = \frac{\mathrm{q}N_{\mathrm{d}}}{2\epsilon_{\mathrm{si}}} \left(d_{\mathrm{max}} - \frac{Q_{\mathrm{sig}}}{N_{\mathrm{d}}} \right)^2 , \tag{6.4}$$

where N_{d} denotes the donor concentration of the buried channel. Hence, as the size of the signal charge packet increases, it is more likely that charge carriers interact with the Si/SiO_2 interface. Moreover, as a certain signal level is reached, the buried channel CCD behaves like a surface channel CCD causing the signal charges to collect at the Si/SiO_2 interface. This is shown in Figure 6.6, where the electrostatic potential as a function of the distance x from the Si/SiO_2 interface for various signal charge levels were simulated. Relating these results to the time-

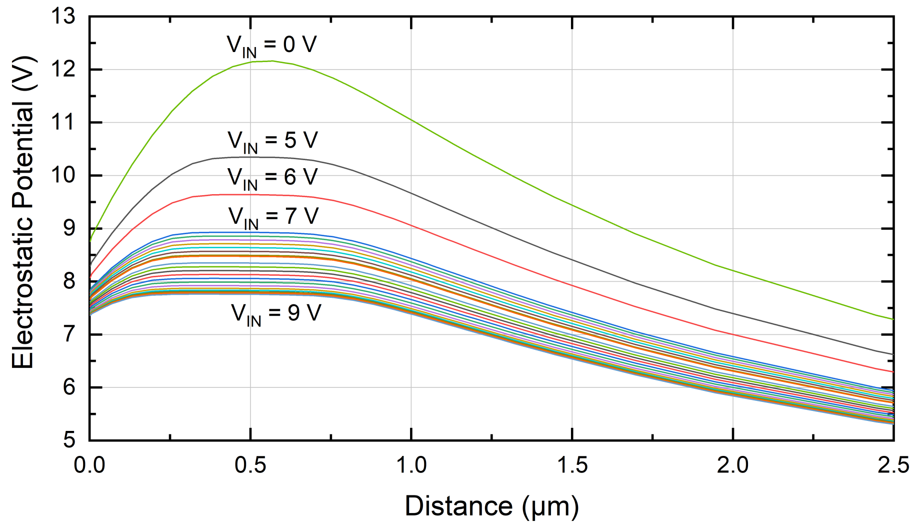

Figure 6.6: Electrostatic Potential for various signal levels. The increment from V_{IN} = 7 V to V_{IN} = 9 V occurs in steps of 0.1 V.

delay integration mode in CCDs, it is evident that since the charge is accumulated continuously after each TDI stage, the signal charge packets approach the Si/SiO_2 interface and cause a possible interaction resulting in a degradation of the transfer efficiency due to the presence of interface states.

6.2.4 Charge Transfer Efficiency

To examine the influence of these interface states on a CCD operated in time-delay integration mode, defect states with a defined trap density and cross-section were implemented at the interface. Subsequently, to simulate the increasing number of

charge carriers as a consequence of the TDI mode, different-sized charge packets were injected according to the fill-and-spill method explained in section 6.2.2. These charge packets were transferred across the pixel column, while the number of electrons was determined in the first, and after one shift, in the adjacent second pixel. Figure 6.7 shows the number of charge carriers located under both of these pixels for various initial numbers of injected charge carriers.
Comparing these curves, it can be seen that the charge carrier density is reduced for a particular number of injected charge carriers after one shift due to interaction with interface states.

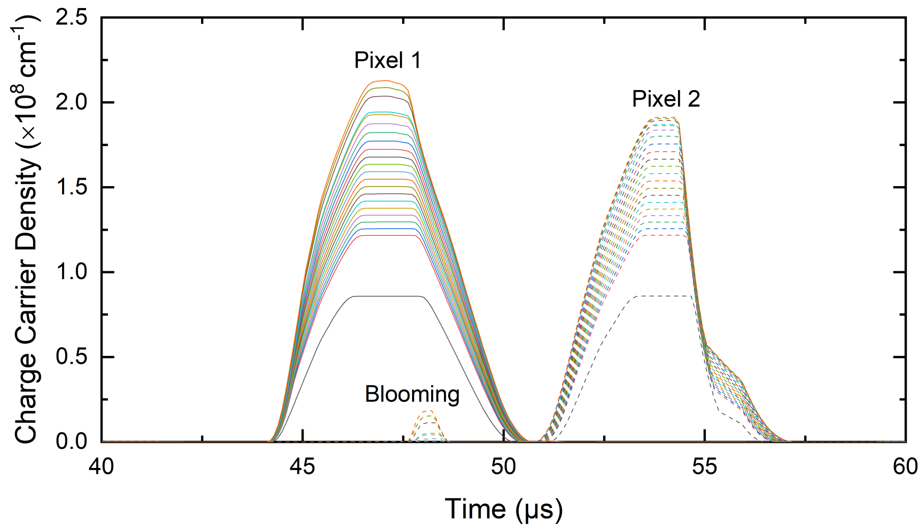

Figure 6.7: Initial charge carrier density in the first pixel (solid line) and the decreased charge carrier density after transfer to the adjacent pixel (dashed line).

Since the CTE is defined as the percentage of successfully transferred electrons, we obtain the relation [70]

$$\mathrm{CTE} = \frac{N_{\mathrm{px.2}}}{N_{\mathrm{px.1}}}, \tag{6.5}$$

where $N_{\mathrm{px.1}}$ and $N_{\mathrm{px.2}}$ are the number of electrons under the first, respectively the second pixel. Calculating the CTE and depicting it in dependence on the initial number of injected charge carriers, we identify a behavior that is separable in four sections (see Figure 6.8). At first, disregarding other charge loss mechanisms, the CTE corresponds to CTE = 1 since for the present amount of charge located in the potential well, there is no contact with the Si/SiO_2 interface yet. As the

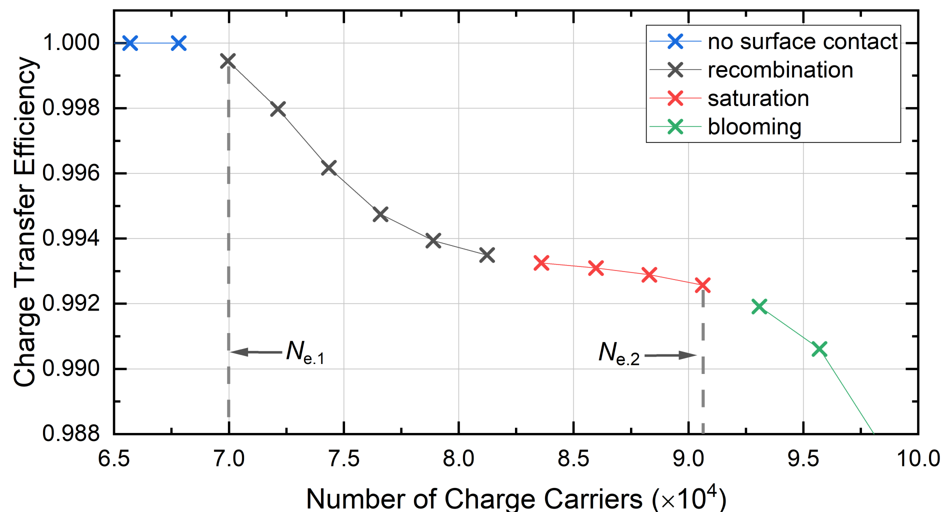

Figure 6.8: Simulated charge transfer efficiency after one shift in dependence on the injected number of charge carriers. The four sections are emphasized in different colors. Within the interval $N_e \in [N_{e.1}, N_{e.2}]$ the CTE can be approximated by an exponential function.

number of charge carriers increases, the CTE starts to decrease since more and more electrons begin to interact with the Si/SiO_2 interface. As soon as the traps become saturated, the CTE takes on a constant value until the accumulated charge exceeds the saturation level of the pixel and thus results in blooming, which decreases the CTE considerably.

6.2.5 Charge Transfer Efficiency for TDI

The charge transfer efficiency in dependence of a varying charge carrier concentration N_e can be, relating to the simulations depicted in Figure 6.9, approximated by an exponential function

$$\gamma(N_e) = 1 - \epsilon(N_e) = \mathrm{CTE}_0 + m \cdot \exp(R_0 \cdot N_e), \tag{6.6}$$

where the interval $N_e \in [N_{e.1}, N_{e.2}]$ indicates the range of the exponential course and $\epsilon(N_e)$ denotes the charge dependent transfer inefficiency, respectively $\gamma(N_e)$ the transfer efficiency after one shift. If the charge carrier concentration is $N_e < N_{e.1}$, the CTE will not be affected since there is no interaction with the interface. On the other hand, if $N_e > N_{e.2}$, blooming will occur, causing significant degradation of the CTE. This approximation enables the calculation of the

CTE after N_{TDI} shifts for a given trap concentration and a constant generation of charge carriers g_{n} according to

$$\mathrm{CTE} = \prod_{i=1}^{N_{\mathrm{TDI}}} 1 - \epsilon(N_{\mathrm{e}} + g_{\mathrm{n}} - r_{\mathrm{n}}) = \prod_{i=1}^{N_{\mathrm{TDI}}} \gamma(N_{\mathrm{e}} + g_{\mathrm{n}} - r_{\mathrm{n}}), \tag{6.7}$$

while considering the charge loss due to recombination r_{n}, which took place one charge shift earlier.

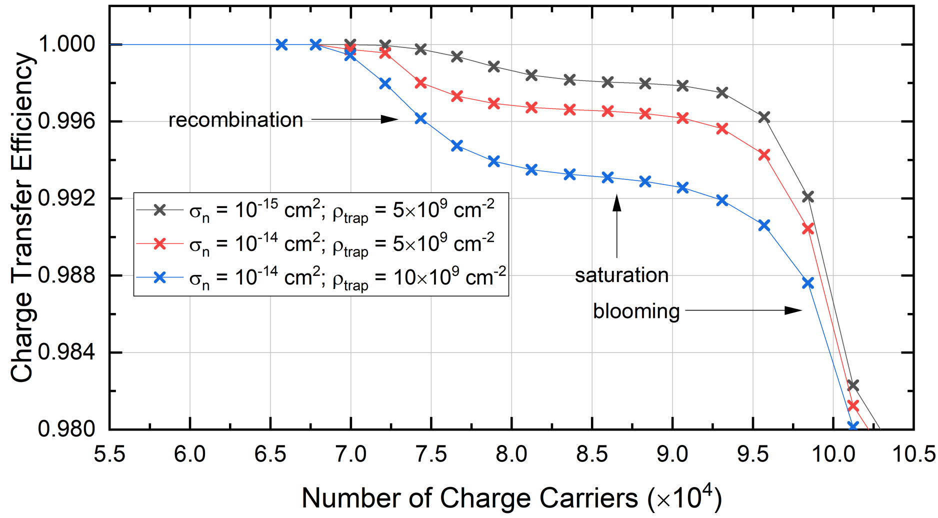

Figure 6.9: Transfer efficiency γ after one shift process in dependence on the charge quantity for various trap concentrations. The pixel area is 7 µm × 5.4 µm.

The total number of accumulated charge carriers after N_{TDI} shifts depends on the charge generation rate per TDI stage and the trap concentration. Figure 6.10 shows the simulations for two different generation rates. As can be observed, the course of the plots can be divided into two different manners. The first shows a decrement in the number of charge carriers dependent on the TDI stage. This decrement occurs since the trap concentration, i.e., the recombination rate, is higher than the concentration of charge carriers at the interface. However, as the accumulation proceeds, the number of charge carriers reaches a constant value due to an equilibrium state between generation and recombination of charge carriers, i.e., the same amount of generated charge carriers recombines with the defect states.

The increment of the charge carrier number is the second manner and occurs because the generation rate is higher than the recombination rate at the interface. This process takes place as long as $N_{\mathrm{e}} < N_{\mathrm{e.2}}$. If this upper limit is exceeded, the blooming of excess charge carriers needs to be considered. At this point, the total quantity of charge carriers will remain constant at full well capacity since the potential well reaches the maximum amount of charge carriers it can store.

The generation rate can be expressed in dependence of the photon number and quantum efficiency according to $g_n = \frac{\eta N_{\mathrm{p}}}{t_{\mathrm{exp}}}$.
To quantify the described cases, the relation between generation and recombination rate

$$\frac{g_{\mathrm{n}}}{r_{\mathrm{n}}} = \frac{\eta N_{\mathrm{p}}}{r_{\mathrm{n}} t_{\mathrm{exp}}} > 0, \tag{6.8}$$

can be considered. Here, the ratio $\frac{g_{\mathrm{n}}}{r_{\mathrm{n}}} > 1$ causes a continuous increase of the total number of charge carriers until blooming occurs, while $0 < \frac{g_{\mathrm{n}}}{r_{\mathrm{n}}} < 1$ results at some point in an equilibrium state between generation and the charge dependent recombination rate.

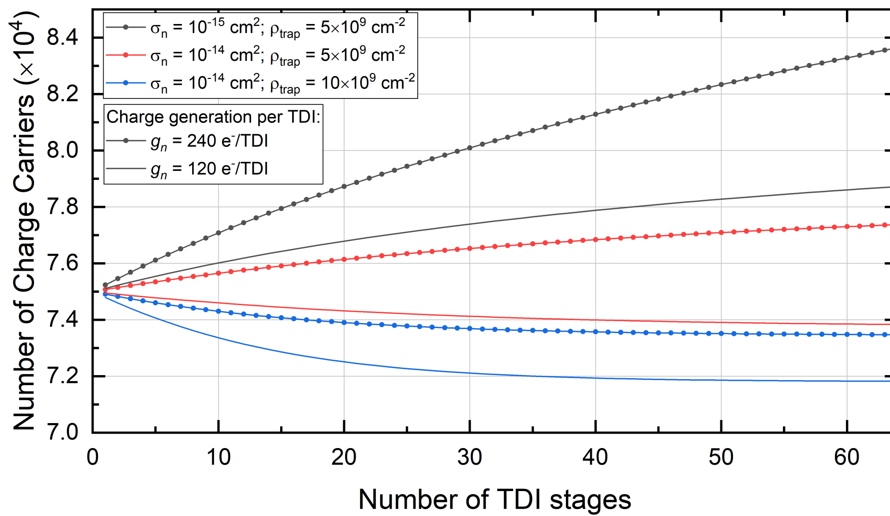

Figure 6.10: Number of charge carriers for 64 shifts in dependence on the number of TDI stages. g_{n} is the generation rate of charge carriers per TDI stage, and $N_{\mathrm{e}} = 75$ ke^{-} is the initial number of charge carriers.

The calculation of the CTE, plotted in Figure 6.11, shows that a high trap

density results in a stronger degradation. However, this is also the case for a high generation rate of charge carriers. As soon as the potential maximum approaches the interface, a high generation rate would increase the total number of charge carriers, respectively a higher number of charge carriers is located in the vicinity of the interface resulting in a significant loss of charge carriers. Nevertheless, new charges are generated in the next TDI stage, and the whole procedure repeats. This causes the total number of generated charge carriers to increase with each TDI step, but the net amount of actual existing carriers in the pixel is significantly lower. Hence, the ratio, i.e., the CTE, decreases considerably. This can be especially problematic for TDI CCDs if the number of chosen TDI stages is too high.

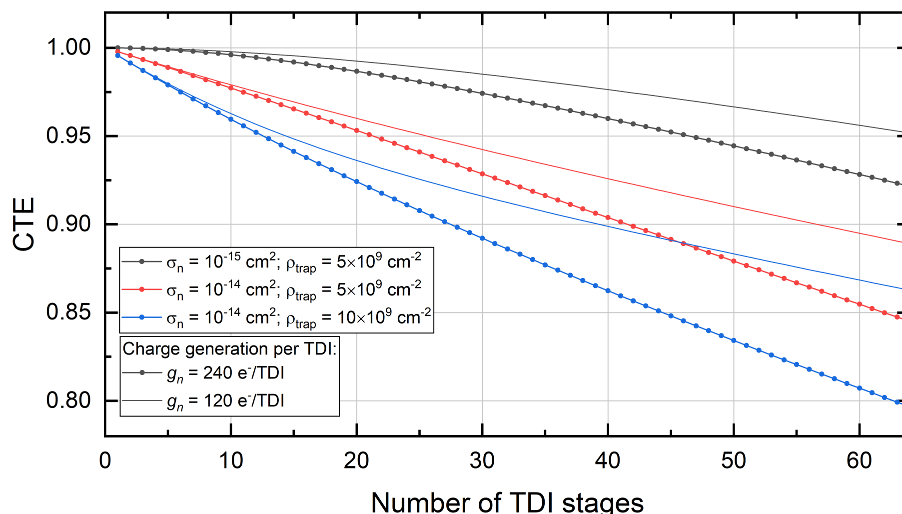

Figure 6.11: CTE for 64 shifts in dependence on the number of charge carriers. g_n is the generation rate of charge carriers per TDI stage, and $N_\mathrm{e} = 75\ \mathrm{ke}^-$ is the initial number of charge carriers.

Finally, the results indicate that as soon as there is contact with the interface, a higher generation rate g_n per TDI stage degrades the CTE stronger than the lower generation rates. This is because, in the former case, more charge carriers are added per TDI stage, causing more charge carriers to interact with the interface. Therefore, the recombination probability increases as well.

Consequently, in the case of TDI CCDs, a proper choice of the TDI stage

numbers would solve this problem since the total number of generated charge carriers can be adjusted. However, this requires special wiring and control of the polysilicon gates and needs to be considered while designing the sensor. Otherwise, an inappropriate number would result either in strong CTE degradation, as indicated above, or in a weak signal.

6.3 Experimental Results

6.3.1 Experimental Setup

To verify the obtained simulation results, measurements of the CTE have been performed. Here, the way of proceeding is equal to Chapter 4. At first, the sensor is placed in a dark chamber where an illumination source provides monochromatic light of the wavelength $\lambda = 850$ nm. By gradually varying the irradiance E_e ($\mathrm{W/cm^{-2}}$), the total number of photons N_p that hit the pixel area A_px during the exposure time t_exp can be adjusted according to the already known equation

$$N_\mathrm{p} = \frac{A_\mathrm{px} E_\mathrm{e} t_\mathrm{exp} \lambda N_\mathrm{TDI}}{\mathrm{hc}}. \tag{6.9}$$

Since the illumination of the sensor causes the generation of signal charge carriers whose number scales linearly to the photon number, we use the responsivity curve

$$\mu_y = \mu_{y.\mathrm{dark}} + R \cdot N_\mathrm{p}, \tag{6.10}$$

where the readout converts the generated charge into digital gray values μ_y, to determine the CTE. The subsequent measurements will be carried out with $N_\mathrm{TDI} = 128$ to provide a high number of total generated charge carriers.
Furthermore, the performed optical measurements, respectively the obtained results will be verified and compared with measurements using the fill-and-spill method. For this, the timing and procedure described in Section 6.2.2 will be applied.

6.3.2 Method and Measurement

To investigate the charge transfer efficiency for charge-coupled devices operating in time-delay integration mode, measurements of the responsivity were performed. The resulting responsivity curves are depicted in Figure 6.12. As can be observed,

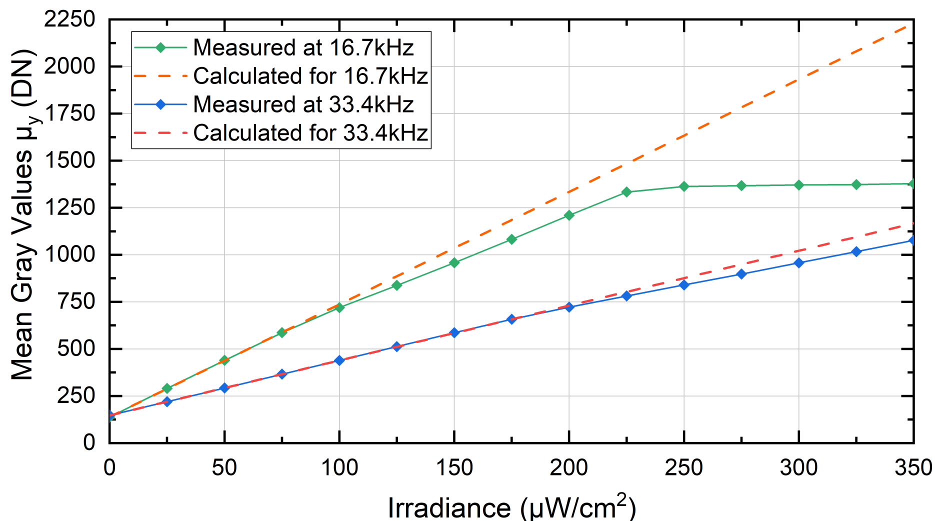

Figure 6.12: Mean gray values versus irradiance. The solid lines indicate the measured curves for 128 TDI stages at 16.7 kHz and 33.4 kHz line rates. The dashed line shows the calculated responsivity curve without any charge losses.

both measurements show a sudden decrease of the responsivity at μ_y = 750 DN. Regarding the definition, this means that the strength of the signal is attenuated, i.e., a loss of signal charges occurs as results from an inefficient transfer of charge carriers caused by contact with the interface.

Moreover, the curve at half line rate 16.6 kHz, i.e., double exposure time, reaches at E_e = 225 μW/cm^2 the saturation level which lies at 1375 DN. Consequently, the pixel is filled at this level and can not store other charge carriers.
To determine the charge transfer efficiency, theoretical responsivity curves for both cases are calculated. Here, the relation of measured and calculated mean gray values yields the CTE according to

$$\mathrm{CTE} = \frac{\mu_{y.\mathrm{meas}}}{\mu_{y.\mathrm{calc}}} \tag{6.11}$$

The corresponding CTE curves are depicted in Figure 6.13. Similar to the simulations, there is no degradation of the CTE at first, i.e., there is no contac with the interface.
However, the CTE starts to decrease gradually at E_e = 100 μW/cm^2, which correspond to the kink appearing in Figure 6.12. Moreover, as the saturation is reached, an incline in degradation can be observed since the number of stored

charge carriers remains constant, but the total number of generated charge carriers increases further.

Hence, we can identify the same sections in the measurements as we did in the simulations. Yet, the main difference is that the measurements yield the CTE after 128 TDI stages depending on the irradiance, whereas the simulations result in a CTE after one TDI stage for varying numbers of charge carriers. However, the responsivity measurements qualify as a simple method to determine the CTE for TDI-CCDs depending on the irradiance. An examination of charge loss us-

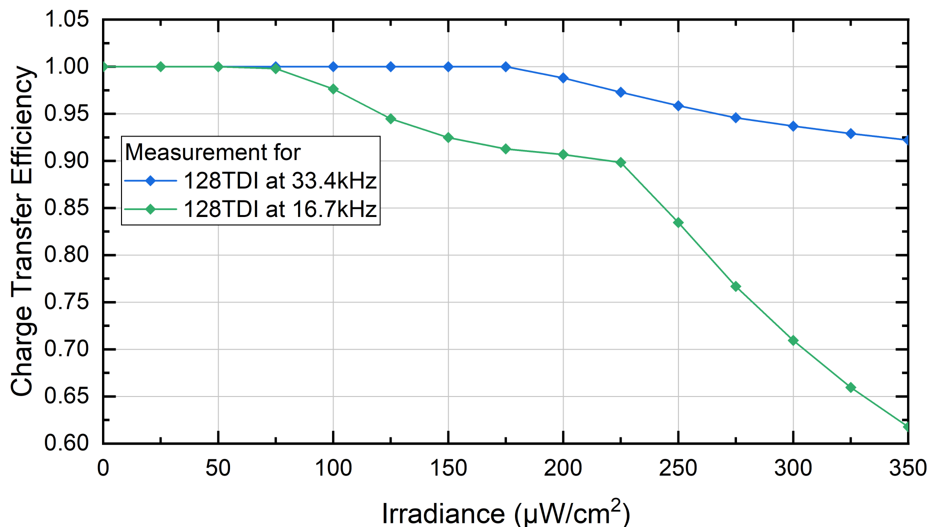

Figure 6.13: Transfer efficiency after 128 TDI stages and 16.7 kHz and 33.4 kHz line rate. The number of generated charge carriers per TDI stage is linear to the irradiance.

ing the fill-and-spill method can be performed equivalently. For this, the mean gray values versus the injection voltage and the capacitance versus the number of injected charge carriers have been depicted in Figure 6.14. As can be seen, the mean gray values increase approximately linearly at the beginning but then exhibit a kink at 700 DN, just as the measured curves with illumination shown above in Figure 6.12. The collapse of the capacitance in the highlighted region refers to this kink and indicates a reduced growth of μ_y depending on V_{IN}, respectively the number of charge carriers. This is mainly caused by considerable charge loss due to contact with the interface as has been shown previously.

Considering the capacitance more in detail, it can be observed that the capaci-

tance starts to scale in a good approach linearly after the collapse. This indicates that the buried-channel CCD, which capacitance acts in a non-linear manner in relation to V_{IN}, starts to operate as a surface-channel CCD. The linear part of the graph proves this by verifying the linear behavior of Eq.(6.3).

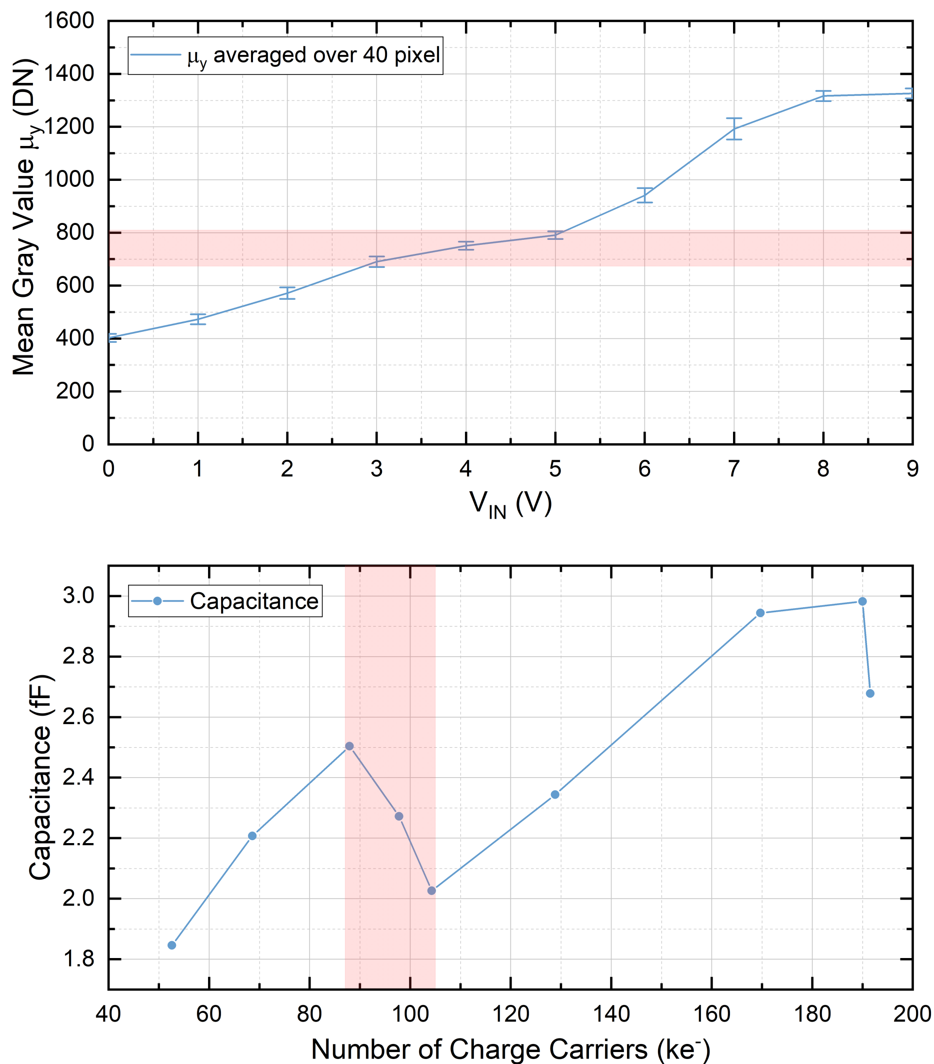

Figure 6.14: Measurement of the injected charge for a buried channel CCD. Curve represents the average over 40 pixel columns with 128 TDI stages each (top). Capacitance in dependence on the number of charge carriers (bottom). The red region highlights the occurrence of interface contact until saturation.

Further, the fill-and-spill method is qualified to determine precisely the amount of charge carriers in a buried-channel CCD where interface contact occurs.

However, as was already explained before, the occurrence of surface contact can be affected by applying a higher voltage to the gates since it broadens the depletion width. Variations of the gate voltage would therefore reduce or increase the maximum amount of charge carriers a pixel can hold without interacting with the interface. The optimizations of additional design parameters also contribute to improving the CTE.

6.4 Summary

As was presented in this chapter, the charge carriers in a buried-channel CCD approach the Si/SiO_2 interface as their total amount increases. A method to determine the charge transfer efficiency in TCAD simulations has been presented. Simulations with varying trap densities and generation rates concerning TDI mode have been carried out. An exponential behavior, which equals the SRH-Theory, could be identified, yielding an approach to describe the CTE in buried-channel TDI CCDs. Depending on the generation/recombination ratio, two different manners have been found, affecting the CTE considerably. The obtained results have been verified by measurements using the optical and electrical generation of charge carriers. A simple experimental method to determine the CTE has been presented. Finally, the occurrence of interface contact has been related to a collapse of the oxide capacitance yielding a method to identify the interaction of the signal charge packet with the Si/SiO_2 interface. A method to prevent interaction with the Si/SiO_2 interface is a proper choice of TDI stages, with which the total generated charge carriers can be adjusted so that a significant interaction is avoidable.

Chapter 7

Conclusions and Outlook

The purpose of this thesis was to study the effect of continuous charge accumulation due to the time-delay integration mode regarding the image quality and the sensor parameters. In order to achieve this, analytical models, simulations, and measurements have been derived and carried out concerning three main degradation effects.

The deployment of an anti-blooming clocking scheme where photogenerated charge carriers of not desired TDI stage have been removed by shifting in the opposite direction turned out to be crucial for the characterization of a TDI-CCD. A method for identifying charge blooming in TDI CCDs has been shown and verified by responsivity measurements. While the measurement with implemented anti-blooming yielded equal responsivities for various numbers of active TDI stages, the measurements without anti-blooming differed for TDI stage adjustment showing deviations of up to 143% from the actual value. Here, the blooming effect increased with an increased number of inactive TDI stages where the generated charge carriers had not been removed.
Measurements with reduced numbers of active TDI stages and no implemented anti-blooming mechanism stated further apparent deviations of the determined sensor parameters compared to an implemented anti-blooming mechanism. So, the SNR with no AB was 28% higher at maximum value than the SRN with AB. Hence, the former SNR curve was closer to an ideal SNR curve. Nevertheless, since the accumulated charge carriers within the pixel do not relate to the actual signal, the results without AB have no validity. This becomes obvious when

regarding the quantum efficiencies for various TDI stage numbers. The measurements without AB resulted in quantum efficiencies ranging from 60% for 128 TDI stages (the whole pixel array) which is the correct value, up to 140% for 32 TDI stages. The reason can be explained by the definition of the QE, which is the ratio of photogenerated electrons to incident photons. Here, due to blooming, a contribution of overflowing charge carriers adds up to the number of photogenerated electrons while the number of incident photons remains the same. This circumstance results in varying quantum efficiencies in dependence on blooming and can be applied to other sensor characteristics, such as the dynamic range, which is affected too. Although the photon transfer method is mainly used to characterize sensors and cameras, the PTC and the conversions gain did not reflect any indication of charge blooming, making the conversion gain in itself not a reliable quantity to verify the proper function of a TDI sensor. To demonstrate how the image quality is degraded, the influence of blooming on the modulation has been determined. At an irradiance of 350 $\mu W/cm^2$, which corresponds to 2.25×10^3 photons per TDI stage, the measurement for 64 TDI stages resulted in a modulation of 0.7 with and 0.4 without an anti-blooming mechanism, yielding a difference of 75% and confirming the need of an implemented anti-booming mechanism.

Aside from charge blooming, the charge transfer efficiency plays an important role for the image quality since it affects the MTF considerably. Therefore, the second part of this thesis has been concerned with the degradation of the image due to charge loss during transfer. In general, the degradation of the CTE is created due to two mechanisms: The incomplete transfer of charge carriers associated with the fall time of the applied clock and charge trapping by interface and defect states.

The former mechanism is generally dependent on the design parameters of the device and the size of the charge packet which has to be transferred. An analytical model which considers these aspects has been derived while containing all affecting transfer mechanisms, namely the self-induced drift, the fringing-field drift, and the thermal diffusion. According to this model, the majority of charge carriers are transferred by self-induced drift, contributing $\leqslant$90% to the charge transfer efficiency, whereas the remaining charge carriers are then driven by the fringing-

field. Apart from the design parameters, the transfer efficiency depends strongly on the number of initial charge carriers. To examine the behavior, the fringing-field was kept at a constant value while the number of charge carriers varied. Comparing the cases for an initial number of charge carriers $n_0 = 5 \times 10^{11}$ cm^{-2} and $n_0 = 20 \times 10^{11}$ cm^{-2}, it was apparent that the latter achieves at the beginning a higher transfer efficiency in the same amount of time, due to a stronger self-induced drift-field. However, as the charge carrier density decreases, the fringing-field surpasses the self-induced drift. As a consequence, the former constellation, which contains fewer charge carriers, becomes faster transferred, i.e., yields a higher CTE in a shorter amount of time. Here, the simulations have shown that the time required for reaching a transfer inefficiency $\epsilon = 10^{-5}$ was by factor 4 higher for $n_0 = 20 \times 10^{11}$ cm^{-2} than for $n_0 = 5 \times 10^{11}$ cm^{-2} at the same conditions. The same contemplation has been carried out for a constant initial number of charge carriers and varying fringing-fields, where the results showed that a higher absolute E_{ff} yields a higher CTE. For the chosen parameter set, the line frequency required to obtain a transfer inefficiency $\epsilon = 10^{-5}$ lies in the MHz regime, respectively the order of magnitude for the integration time is in nanoseconds. However, this order of magnitude can vary strongly in dependence on the design parameters. Therefore a discussion of contained parameters in this model has been provided, highlighting the crucial ones for an efficient charge transfer, which are the gate length L, the doping concentration N_{d} of the buried-channel, the oxide thickness d_{ox}, and the depletion width t_{d}. By optimizing these parameters, a higher CTE and MTF can be achieved.

The second CTE degradation mechanism occurs due to interface states with energy levels located in the forbidden band gap, causing charge carriers at the interface to recombine with these traps. To prevent contact of these photogenerated charge carriers with the interface, in general, buried-channel CCDs are deployed, where the charge is stored within the silicon in the depletion region. Nevertheless, an increasing number of charge carriers causes the depletion region to decrease and the electrons to approach the interface, as has been shown with TCAD. To simulate the CTE between two adjacent pixels for a CCD operating in TDI mode, charge carriers have been injected using the fill-and-spill method and transferred across the pixel column. The ratio of the number of charge carriers

before and after one single pixel shift, corresponding to the CTE, has shown a CTE curve allocable in four sections. At first, there was no surface contact, i.e., the CTE did not decrease. As the number of charge carriers increased, the CTE decreased until all defect states at the interface were saturated. This decrement corresponded to a declining exponential curve and coincided with the predicted behavior. Finally, the charge started blooming as the FWC was exceeded. This contemplation was carried out for three different defect concentrations, where the lowest defect concentration yielded a CTE at saturation of around 99.8% and the highest concentration a CTE of 99.3%.
The determination of the CTE after one shift for a particular number of charge carriers allowed the derivation of a model, where the CTE after N shits can be calculated depending on the number of photogenerated electrons and the number of traps. Here, depending on the number of generated electrons per TDI stage, the number of collected electrons increases continuously until blooming occurs since the generation rate surpasses the recombination rate. Otherwise, for a recombination rate higher than the generation rate, the number of electrons reaches a constant level because an equilibrium state adjusts. This behavior has been expressed analytically by relating the number of traps to the number of incident photons. However, the CTE still decreases in both cases due to an increasing number of total generated electrons.
These simulations have been verified with measurements employing a TDI CCD with 128 TDI stages at different irradiance levels and line rates. The resulting responsivity curve for the measurement at a line frequency of 16.7 kHz shows kink in the curve at an irradiance of 100 $\mu W/cm^2$, whereas at a double frequency of 33.4 kHz, the kink occurs at 100 $\mu W/cm^2$. Both cases show the same generation rate per TDI stage at these constellations. Further, the kink in the responsivity curve indicates a loss of signal charge carriers. Hence, the signal charge interacts with the Si/SiO_2 interface at these respective irradiance levels and line rates. The electrical injection of different-sized charge packets with the fill-and-spill method supported these results. Moreover, the consideration of the oxide capacitance allows identifying charge packet size where a buried-channel CCD operates similarly to a surface channel CCD.
In conclusion, measures have to be adopted to prevent the interaction of charge packets with the Si/SiO_2 interface. Here, the design, as well as the operating

mode, affect the CTE significantly. However, due to the proper choice of TDI stages, the total generated charge carriers can be adjusted so that considerable contact is avoidable. Hence, it has to be ensured that the accumulated charge carriers do not approach the surface by choosing design parameters that induce a higher depletion width on the one hand and choosing an appropriate number of TDI stages on the other hand.

This work can be continued with the study of occurring blooming in unused stages while the anti-blooming mechanisms are active. Considering a CCD column with 128 TDI stages from which 32 are intended for readout and 96 for anti-blooming. At very high irradiation levels, there is the possibility that blooming takes place in the direction of the active stage even if the AB mechanism is implemented since the generation of charges is faster than they can be removed. Considering the respective unique applications of TDI CCDs, more detailed analysis for certain conditions resembling applications in space can be accomplished. Nevertheless, TDI CCDs can vary enormously, depending on which attributes are required. Hence, this thesis provides methods and tools to choose optimal design parameters regarding the needs and applications that can be developed and improved further.

Publications

- D. S. Piechaczek, O. Schrey, M. Ligges, B. Hosticka, and R. Kokozinski, “Anti-blooming clocking for time-delay integration CCDs,” Sensors, vol. 22, no. 19, p. 7520, Oct. 2022. DOI: 10.3390/s22197520
- D. S. Piechaczek, B. J. Hosticka, M. Ligges, O. Schrey, and R. Kokozinski, “Analytical model of free charge transfer in charge-coupled devices,” Solid-State Electronics, p. 108513, Nov. 2022. DOI: 10.1016/j.sse.2022.108513
- D. S. Piechaczek, M. Ligges, B. J. Hosticka, and R. Kokozinski, “Impact of Interface States on TDI CCDs,” Solid-State Electronics. (In Preparation)

References

[1] A. B. Garrett, “The discovery of the transistor: W. Shockley, J. Bardeen, and W. Brattain,” *Journal of Chemical Education*, vol. 40, no. 6, p. 302, Jun. 1963.

[2] W. Aspray, “The intel 4004 microprocessor: what constituted invention?” *IEEE Annals of the History of Computing*, vol. 19, no. 3, pp. 4–15, 1997.

[3] W. S. Boyle and G. E. Smith, “Charge coupled semiconductor devices,” *Bell System Technical Journal*, vol. 49, no. 4, pp. 587–593, Apr. 1970.

[4] G. E. Smith, “The invention and early history of the CCD,” *Nuclear Instruments and Methods in Physics Research Section A: Accelerators, Spectrometers, Detectors and Associated Equipment*, vol. 607, no. 1, pp. 1–6, Aug. 2009.

[5] E. Gerstner, “Nobel prize 2009: Kao, boyle & smith,” *Nature Physics*, vol. 5, no. 11, pp. 780–780, Oct. 2009.

[6] S. Mendis, S. Kemeny, and E. Fossum, “CMOS active pixel image sensor,” *IEEE Transactions on Electron Devices*, vol. 41, no. 3, pp. 452–453, Mar. 1994.

[7] R. H. Walden, R. H. Krambeck, R. J. Strain, J. McKenna, N. L. Schryer, and G. E. Smith, “The buried channel charge coupled device,” *Bell System Technical Journal*, vol. 51, no. 7, pp. 1635–1640, Sep. 1972.

[8] C. Kittel and P. McEuen, *Introduction to solid state physics.* John Wiley & Sons, 2018.

[9] S. M. Sze and M.-K. Lee, *Semiconductor Devices: Physics and Technology: Physics and Technology.* Wiley Global Education, 2012.

[10] D. Barbe, "Imaging devices using the charge-coupled concept," *Proceedings of the IEEE*, vol. 63, no. 1, pp. 38–67, 1975.

[11] S. M. Sze, Y. Li, and K. K. Ng, *Physics of semiconductor devices.* John wiley & sons, 2021.

[12] L. Esser, "Peristaltic charge-coupled device: a new type of charge-transfer device," *Electronics Letters*, vol. 8, no. 25, p. 620, 1972.

[13] R. M. Barsan, "Surface and bulk charge transport in a buried-layer MOS structure," *International Journal of Electronics*, vol. 44, no. 1, pp. 97–104, Jan. 1978.

[14] B. E. Saleh and M. C. Teich, *Fundamentals of photonics.* john Wiley & sons, 2019.

[15] M. A. Green and M. J. Keevers, "Optical properties of intrinsic silicon at 300 k," *Progress in Photovoltaics: Research and Applications*, vol. 3, no. 3, pp. 189–192, 1995.

[16] M. A. Green, "Self-consistent optical parameters of intrinsic silicon at 300k including temperature coefficients," *Solar Energy Materials and Solar Cells*, vol. 92, no. 11, pp. 1305–1310, Nov. 2008.

[17] J. R. Janesick, K. P. Klaasen, and T. Elliott, "Charge-coupled-device charge-collection efficiency and the photon-transfer technique," *Optical Engineering*, vol. 26, no. 10, Oct. 1987.

[18] D. Durini, *High performance silicon imaging.* Woodhead Publishing, 2014.

[19] A. J. Theuwissen, *Fundamentals of Charge-Coupled Devices.* Springer, 1995.

[20] T. Kuroda, *Essential principles of image sensors.* CRC press, 2017.

[21] R. Hui, *Introduction to fiber-optic communications.* Academic Press, 2019.

[22] U. Teubner and H. J. Brückner, *Optical Imaging and Photography.* De Gruyter, Feb. 2019.

[23] H.-S. Wong, Y. L. Yao, and E. S. Schlig, "TDI charge-coupled devices: Design and applications," *IBM Journal of Research and Development*, vol. 36, no. 1, pp. 83–106, Jan. 1992.

[24] J. E. Rushton, K. D. Stefanov, A. D. Holland, J. Endicott, F. Mayer, and F. Barbier, "A CMOS TDI image sensor for earth observation," in *SPIE Proceedings*, E. W. Taylor and D. A. Cardimona, Eds. SPIE, Sep. 2015.

[25] C.-H. Koo, H.-K. Kim, K.-H. Paik, D.-C. Park, K.-H. Lee, Y.-K. Park, C.-R. Moon, S.-H. Lee, S.-H. Hwang, D.-H. Lee, and J.-T. Kong, "Improvement of crosstalk on 5m cmos image sensor with 1.7 x 7μm^2 pixels," in *SPIE Proceedings*, K.-T. Tsen, J.-J. Song, M. J. Cohen, and J. W. Glesener, Eds. SPIE, Feb. 2007.

[26] C. Serief and Y. Ghelamallah, "Dynamic MTF estimate of the optical imager onboard alsat-1b satellite," in *International Conference on Space Optics — ICSO 2018*, N. Karafolas, Z. Sodnik, and B. Cugny, Eds. SPIE, Jul. 2019.

[27] G. Lepage, J. Bogaerts, and G. Meynants, "Time-delay-integration architectures in CMOS image sensors," *IEEE Transactions on Electron Devices*, vol. 56, no. 11, pp. 2524–2533, Nov. 2009.

[28] J. C. Feltz and M. A. Karim, "Modulation transfer function of charge-coupled devices," *Applied Optics*, vol. 29, no. 5, p. 717, Feb. 1990.

[29] A. Eckardt, S. Gläsener, R. Reulke, K. Sengebusch, and B. Zender, "Status of the next generation CMOS-TDI detector for high-resolution imaging," in *Earth Observing Systems XXIV*, J. J. Butler, X. J. Xiong, and X. Gu, Eds. SPIE, Sep. 2019.

[30] A. Materne, A. Bardoux, H. Geoffray, T. Tournier, P. Kubik, D. Morris, I. Wallace, and C. Renard, "Backthinned TDI CCD image sensor design and performance for the pleiades high resolution earth observation satellites," in *International Conference on Space Optics — ICSO 2006*, E. Armandillo, J. Costeraste, and N. Karafolas, Eds. SPIE, Nov. 2017.

[31] A. Ercan, L. Haspeslagh, K. De Munck, K. Minoglou, A. Lauwers, and P. De Moor, "Prototype TDI sensors in embedded CCD in CMOS technology," in *Proceedings of the International Image Sensor Workshop*, 2013.

[32] S. R. Kamasz, S. P. Singh, S. G. Ingram, M. J. Kiik, Q. Tang, and B. Benwell, "Enhanced full well for vertical antiblooming, high sensitivity time-delay and integration (tdi) ccds with ghz data rates," in *IEEE Workshop on Charge-Coupled Devices and Advanced Image Sensors*, vol. 6, 2001.

[33] P. Boulenc, J. Robbelein, L. Wu, L. Haspeslagh, P. D. Moor, J. Borremans, and M. Rosmeulen, "High speed TDI embedded CCD in CMOS sensor," in *International Conference on Space Optics — ICSO 2016*, N. Karafolas, B. Cugny, and Z. Sodnik, Eds. SPIE, Sep. 2017.

[34] M. Farrier and R. Dyck, "A large area TDI image sensor for low light level imaging," *IEEE Journal of Solid-State Circuits*, vol. 15, no. 4, pp. 753–758, Aug. 1980.

[35] D. S. Piechaczek, O. Schrey, M. Ligges, B. Hosticka, and R. Kokozinski, "Anti-blooming clocking for time-delay integration CCDs," *Sensors*, vol. 22, no. 19, p. 7520, Oct. 2022.

[36] J. R. Janesick, *Scientific charge-coupled devices.* International Society for Optics and Photonics, 2001.

[37] A. Driewer, "Modellierung von 3d-time-of-flight-sensoren und-systemen," Ph.D. dissertation, Dissertation, Duisburg, Essen, Universität Duisburg-Essen, 2016, 2016.

[38] F. Dierks, "Sensitivity and image quality of digital cameras," *Image_Quality_of_Digital_Cameras.pdf*, 2004.

[39] E. M. V. Association *et al.*, "Emva standard 1288, standard for characterization of image sensors and cameras," *Release*, vol. 3, p. 29, 2010.

[40] J. R. Janesick, *Photon Transfer.* SPIE, Aug. 2007.

[41] G. D. Boreman, *Modulation Transfer Function in Optical and Electro-Optical Systems.* SPIE, Jul. 2001.

[42] W. Singer, M. Totzeck, and H. Gross, *Handbook of Optical Systems, Volume 2, Physical Image Formation*, 10 2005.

[43] M. Singh and S. Brotherton, "Influence of clocking waveform on charge transfer in three phase charge coupled devices," *Solid-State Electronics*, vol. 19, no. 4, pp. 279–287, Apr. 1976.

[44] W. Engeler, J. Tiemann, and R. Baertsch, "Surface charge transport in silicon," *Applied physics letters*, vol. 17, no. 11, pp. 469–472, 1970.

[45] Y. Daimon, A. Mohsen, and T. McGill, "Final stage of the charge-transfer process in charge-coupled devices," *IEEE Transactions on Electron Devices*, vol. 21, no. 4, pp. 266–272, Apr. 1974.

[46] J. Carnes, W. Kosonocky, and E. Ramberg, "Free charge transfer in charge-coupled devices," *IEEE Transactions on Electron Devices*, vol. 19, no. 6, pp. 798–808, Jun. 1972.

[47] ——, "Drift-aiding fringing fields in charge-coupled devices," *IEEE Journal of Solid-State Circuits*, vol. 6, no. 5, pp. 322–326, Oct. 1971.

[48] D. S. Piechaczek, B. J. Hosticka, M. Ligges, O. Schrey, and R. Kokozinski, "Analytical model of free charge transfer in charge-coupled devices," *Solid-State Electronics*, p. 108513, Nov. 2022.

[49] A. Fick, "Ueber diffusion," *Annalen der Physik und Chemie*, vol. 170, no. 1, pp. 59–86, 1855.

[50] M. Grundmann, *The Physics of Semiconductors.* Springer International Publishing, 2016.

[51] T. A. A. Broadbent, "Investigations on the theory of the brownian movement. by a. einstein. pp. 122. 1956-the principles of mechanics. by h. hertz. pp. xlii, 274. 1956-hydrodynamics. by hl dryden, fp murnaghan and h. bateman. pp. 634. 1956.(dover publications, new york)," vol. 41, no. 337, pp. 231–231, Oct. 1957.

[52] V. F. Zaitsev and A. D. Polyanin, *Handbook of Nonlinear Partial Differential Equations.* CRC Press, 2012.

[53] D. Barbe, "Imaging devices using the charge-coupled concept," *Proceedings of the IEEE*, vol. 63, no. 1, pp. 38–67, 1975.

[54] H.-S. Wong, Y. L. Yao, and E. S. Schlig, "TDI charge-coupled devices: Design and applications," *IBM Journal of Research and Development*, vol. 36, no. 1, pp. 83–106, Jan. 1992.

[55] H. Bugnet, C. Guicherd, T. Ligozat, F. Mayer, S. Pesenti, B. Gili, R. Bell, and B. D. Monte, "First measurements of true charge transfer TDI (time delay integration) using a standard CMOS technology," in *International Conference on Space Optics — ICSO 2012*, E. Armandillo, N. Karafolas, and B. Cugny, Eds. SPIE, Nov. 2017.

[56] Y.-F. Chen, C.-M. Kwei, PinSu, and C.-J. Tung, "Dependence of electron mobility on doped impurities," *Japanese Journal of Applied Physics*, vol. 34, no. Part 1, No. 9A, pp. 4827–4833, Sep. 1995.

[57] W. Füssel, M. Schmidt, H. Angermann, G. Mende, and H. Flietner, "Defects at the Si/SiO_2 interface: Their nature and behaviour in technological processes and stress," *Nuclear Instruments and Methods in Physics Research Section A: Accelerators, Spectrometers, Detectors and Associated Equipment*, vol. 377, no. 2-3, pp. 177–183, Aug. 1996.

[58] W. Shockley and W. T. Read, "Statistics of the recombinations of holes and electrons," *Physical Review*, vol. 87, no. 5, pp. 835–842, Sep. 1952.

[59] R. S. Bonilla and P. R. Wilshaw, "On the c-Si/SiO_2 interface recombination parameters from photo-conductance decay measurements," *Journal of Applied Physics*, vol. 121, no. 13, p. 135301, Apr. 2017.

[60] A. G. Aberle, S. Glunz, and W. Warta, "Impact of illumination level and oxide parameters on shockley–read–hall recombination at the si-sio_2 interface," *Journal of Applied Physics*, vol. 71, no. 9, pp. 4422–4431, May 1992.

[61] M. Y. Ghannam and H. A. Kamal, "Modeling surface recombination at the p-type Si/SiO_2 interface via dangling bond amphoteric centers," *Advances in Condensed Matter Physics*, vol. 2014, pp. 1–9, 2014.

[62] U. K. Mishra and J. Singh, *Semiconductor device physics and design.* Springer, 2008, vol. 83.

[63] R. McGrath, J. Doty, G. Lupino, G. Ricker, and J. Vallerga, "Counting of deep-level traps using a charge-coupled device," *IEEE Transactions on Electron Devices*, vol. 34, no. 12, pp. 2555–2557, Dec. 1987.

[64] E. Banghart, J. Lavine, E. Trabka, E. Nelson, and B. Burkey, "A model for charge transfer in buried-channel charge-coupled devices at low temperature," *IEEE Transactions on Electron Devices*, vol. 38, no. 5, pp. 1162–1174, May 1991.

[65] S. P. Emmons and D. D. Buss, "Noise measurements on the floating diffusion input for charge-coupled devices," *Journal of Applied Physics*, vol. 45, no. 12, pp. 5303–5306, Dec. 1974.

[66] M. Tompsett, "Surface potential equilibration method of setting charge in charge-coupled devices," *IEEE Transactions on Electron Devices*, vol. 22, no. 6, pp. 305–309, Jun. 1975.

[67] G. Prigozhin, B. Burke, M. Bautz, S. Kissel, and B. LaMarr, "CCD charge injection structure at very small signal levels," *IEEE Transactions on Electron Devices*, vol. 55, no. 8, pp. 2111–2120, Aug. 2008.

[68] R. Brodersen and S. Emmons, "Noise in buried channel charge-coupled devices," *IEEE Transactions on Electron Devices*, vol. 23, no. 2, pp. 215–223, Feb. 1976.

[69] N. S. Saks, "Interface state trapping and dark current generation in buried-channel charge-coupled devices," *Journal of Applied Physics*, vol. 53, no. 3, pp. 1745–1753, Mar. 1982.

[70] O. Marcelot, R. Molina, M. Bouhier, and P. Magnan, "Design impact on charge transfer inefficiency of surface CCD on CMOS devices: TCAD and characterization study," *IEEE Transactions on Electron Devices*, vol. 63, no. 3, pp. 1099–1104, Mar. 2016.

DuEPublico

Duisburg-Essen Publications online

UNIVERSITÄT DUISBURG ESSEN

Offen im Denken

ub | universitäts bibliothek

Diese Dissertation wird via DuEPublico, dem Dokumenten- und Publikationsserver der Universität Duisburg-Essen, zur Verfügung gestellt und liegt auch als Print-Version vor.

DOI: 10.17185/duepublico/81291
URN: urn:nbn:de:hbz:465-20231214-143243-3

Alle Rechte vorbehalten.